Current fluctuations in ionic nanopores

Mira Zorkot
St Cross College
University of Oxford

A thesis submitted for the degree of
Doctor of Philosophy
Supervised by Ramin Golestanian

Hilary Term 2017

Current fluctuations in ionic nanopores

Mira Zorkot, St Cross College, University of Oxford

A thesis submitted for the degree of *Doctor of Philosophy*, Hilary Term 2017

Abstract

From electrical current to ecological and biological systems, fluctuations are characterised based on the frequency dependence of the power spectral density. Surprisingly - given the diversity of the systems considered - the power spectra of many systems reveal an inverse power-law dependence on the frequency f in certain regimes. This ubiquitous phenomenon famously known as "$1/f$ noise" has triggered an abundance of investigations aimed at understanding its mechanism. Recently, "$1/f$ noise" has also been observed in the ionic electric current through biological ion channels, nanometre-scale membrane pores and solid-state nanopores. Identifying and understanding the source of $1/f$ noise in nanopores emerges as a crucial prerequisite to design nanopore systems for their use in technological devices, such as nanopore-based DNA sequencers. At the same time, the current power spectrum in nanopores contains a wealth of information which, if extracted, would help towards a detailed characterisation of the nanopore's microscopic properties.

To analyse the mechanism behind the occurrence of $1/f$ in nanopores, we study nanopores using Langevin-dynamics simulations and analytical methods. Ions move through the pore driven by an applied electric field, and the induced current is recorded. The power spectral density calculated from this data indicates the existence of a power law frequency dependence in an extended frequency regime.

To verify a series of conclusions drawn from experimental investigations, we systematically vary all parameters characterising the system, including the geometry, the electric field, the ion density and the flexibility of the pore wall. Furthermore, we derive an analytical expression for the current power spectral density and compare it to the results from the Langevin-dynamics simulations. Finally, we evaluate the role of hydrodynamic interactions and find that it does not induce any major changes in the current power spectral density. Our studies allow us to uncover the mechanism that leads to the power law behaviour: interactions among the ionic components.

This work could not have been achieved without your support, and your guidance. To you I dedicate my thesis:

My parents:
Ata Zorkot and Zeina Jouni.

Mom, or better to call you the ideal mom. You thrived to teach us everything, to put us on the right track. You always wanted us to be distinguished and to excel in every detail in our life. "Intellectual growth should commence at birth and cease at death" (Albert Einstein), your unique worldwide dictionary of quotes that you used in every single conversation played a crucial role in our guidance.

Dad, the title of power and strong personality. Arguments, songs, dance, sports you always had something to add to our life. Nothing is impossible, everything can be achieved by hard work were summarized by your favourite continuously repeated Aristotle quote: "The roots of education are bitter but the fruit is sweet".

Mom and Dad, I wanted always to make you proud, and to present you one fruit of your continuous dedication and effort. Maya, Raed, Haya, and myself cannot be more grateful. You have deprived yourselves from various things to provide us with the best environment, education, and life. No matter what are the difficulties that we faced or we might face, we will be always together.

Publications Related to this Thesis

This thesis has used material from the following publications:

Chapters 2 and 3 use material from M. Zorkot and R. Golestanian. Current fluctuations across a nanopore. *Journal of Physics: Condensed Matter* 30(13):134001, 2018.

Chapters 3, 4 and 5 use material from M. Zorkot, R. Golestanian, and D. J. Bonthuis. The power spectrum of ionic nanopore currents: the role of ion correlations. *Nano Letters* 16 (4):2205–2212, 2016.

Chapter 6 uses material from M. Zorkot, R. Golestanian, and D. J. Bonthuis. Current fluctuations in nanopores: The effects of electrostatic and hydrodynamic interactions. *The European Physical Journal Special Topics* 225(8-9):1583–1594, 2016.

Acknowledgements

Firstly, a special thank you goes to my supervisor Prof. Ramin Golestanian for giving me the opportunity to work with him and join his group. Working for my DPhil was not easy for me with all the life challenges but you were there to support and guide me. Prof. Ramin, the guidance that you gave me and the challenges that you encouraged me to take, contributed tremendously in my life, and lead to a new "Mira". Your work dedication and your desk always impressed me. I was happy to find someone who wakes up very early. As you call it, I got the bug of research and this will always be the key towards any future success.

The work presented in this thesis was remarkably supported by Dr. Douwe Bonthuis, to whom I address a thank you. For one year and a half, I had the pleasure to work with you. Douwe, at this moment I do realize how much I gained from your computational skills, and our conversations.

Warmest thanks goes to my two sisters Maya and Haya, and my brother Raed who always showed a great support despite their responsibilities and the distances between us. To my aunt Amina Jouni and my uncle Mosbah Jouni, for the beautiful discussion that we had, I would also like to thank you.

To my partner Mohamad Fahes, I do not have enough words to thank you. You always believed in me and you were always present to tell me that everything will be fine. You were always happier than me when it comes to any achievement that I made. I will never forget the number of trips that you made to support me, especially the last one when you came urgently from Kuwait. Without you my trip would have been much more difficult.

Hawraa Salami, Samar Eid, Ranim Thebian, Youmna El. Bitar, Ali Beydoun, and Sam Sleiman to you I express a heartfelt thank you. Hawraa, you are a special friend. Distance was never a problem for you. You always found a way to make me smile. You succeeded even to find the address of my office to order food for me to show support in my most hard days. Ali despite distances and time you and your chocolate were always supportive.

To my Oxford friends, Arnold Mathijissen, Amin Doostmohammadi, Viviana Ponta, Mattia Sormani, and many others in and outside the Rudolf Peierls Centre thank you. The amazing time that we spent together is unforgettable. From politics to economics, and philosophy we had the chance to enjoy wonderful discussions. I would have never dared to jump in the Thames without you Arnold.

Kalpana Sivabalah, a unique housemate for two years. You have become a best friend, together we shared lot of stories and laughter. You are a very good french speaker now, and you will cook very good dishes one day. For Mr. Rafik Charafeddine I address a thank you. Last but not least, I would like to thank all the researchers that gave me the permissions to use their figures in the introduction.

Contents

List of Figures

List of Tables

CHAPTER 1

Introduction

> *It is probably fair comment to say that to many physicists the subject of fluctuations (or "noise" to put it bluntly) appears rather esoteric and perhaps even pointless; spontaneous fluctuations seem nothing but an unwanted evil which only an unwise experimenter would encounter"*
>
> MacDonald's 1962 text, Noise and Fluctuations.

From everything bad there is something beautiful, this is what the title of this thesis is all about. Noise, a word generally used to describe something annoying and avoidable, emerges in this thesis to be something useful and essential for our survival.

1.1 Overview of the Thesis

In this thesis we begin by introducing noise types and their defining features. Next, the emergence of $1/f$ noise in the current flow of ions in nanopores, where it appears to be playing a crucial role, is developed. Trying to elaborate on the source of the $1/f$ noise from a theoretical perspective, an analytical and computational analysis aiming at better understanding the current flow of ions follows.

This thesis is composed of five related studies focussed on *the current fluctuations inside*

nanopores. Among these, two chapters focus on finding a theoretical description for the current fluctuations of ions, and the other three chapters focus on simulation results under various conditions and how they compare to the analytical expressions.

In addition to the main five chapters, the last chapter presents a quick review of the main conclusions and we provide an outlook of the current and the future work.

Where is that noise? How is it generated? These two questions form the crux of this thesis.

1.2 Noise Types and Characteristics

Noise comes in different forms and derives from different sources. It can be viewed as an unwanted sound generated by humans and industries, or as will be shown, it can be a source of information predominently present in electrical devices and biological systems.

1.2.1 Noise Types

In order to understand the different types of noise that exist, we must consider their power spectrum. A power spectral density shows the variation of any physical measureable such as the current or energy as a function of the frequency. It can be obtained from the Fourier transform of the autocorrelation function of the signal that gives us an insight into how the previous data points are correlated to the future data points at different time steps[4;5].

1.2.2 White Noise

In any stochastic process, the random variable $\eta(t)$ is a collection of random numbers as a function of time t. Particularly, white noise is a distinguished type of random variable. The white noise $\eta_w(t)$ can take any arbitrary value but it should obey a number of properties. First, the numbers generated in a white noise signal are statistically uncorrelated. Second, the average value of the numbers is equal to zero, $\langle \eta_w(t) \rangle = 0$, where $\langle ... \rangle$ denotes the ensemble average. Third, their variance is finite, equivalent to $\langle \eta_w(t)\eta_w(s) \rangle = \sigma^2 \delta(t-s)$. Based on the

Wiener-Khinchin theorem[6], the power spectral density can be calculated from the Fourier transform of the autocorrelation function. More specifically, the power spectral density $S(f)$ of the white noise is flat over the entire frequency range.

1.2.3 Brownian Noise

From the integration over a white noise signal, a brownian noise can be extracted. As its name indicates, the brownian noise is generated by the continuous time stochastic process Brownian motion $W(t)$, where $W(t) = \int_0^t \eta(\tau)d\tau$. Although it is characterised by independent increments, $W(t)$ is correlated to $W(t+\tau)$ contrary to the white noise. Over a frequency range, the power spectrum of $W(t)$ is inversely proportional to the square of the frequency: $S(f) = \frac{S_0}{f^2}$ [7–9].

1.2.4 Flicker Noise

One intermediate and extremely ubiquitous noise type, is the $1/f$ noise. Its power spectrum is inversely proportional to the frequency $S(f) \propto \frac{1}{f}$, however $1/f$ with a unit power cannot be simply derived.

Where do we find $1/f$ *noise? Why is* $1/f$ *noise important?*

$1/f$ noise has been observed in many physical systems[10–17]. Subsequently, a pertinent question arises: *Is there a universal cause for this type of noise despite the diversity of the systems exhibiting it?* First discovered by J.B. Johnson, $1/f$ noise is a mystery that researchers have been exploring for a whole century[11]. In 1927 Johnson's experiments were performed on conductors, distinguishing between thermal noise and tube noise. Although it was generally believed that voltage could not be present in a circuit without any electricity source, Johnson's experiments were the first to correct this common belief. He was able to conclude that irrespective of the surrounding area and of the presence of any DC current, thermal agitation of ions would generate a current, and consecutively an electromotive force.

Measurements across a resistor in thermal equilibrium revealed the presence of mean square voltage fluctuations proportional to both the resistance R and the conductor temperature (Fig. 1.2 rectangular region). To support Johnson's conclusion, Nyquist performed a theoretical derivation for the thermal fluctuations generated in a conductor with resistance R and temperature T, through dealing with two resistors I and II with resistance R as shown in Fig.1.1 [18–20].

Figure 1.1: Two resistors R_{I} and R_{II} with resistance R connected using a long non-dissipative transmission line[20].

A thermal agitation across the first resistor produces a current I through the circuit that will itself produce a power P associated with the second resistor. As expected, from the laws of thermodynamics, the two conductors will equilibrate at the same temperature, with the same current and power. Nyquist extended his work to prove that the equilibrium will be maintained at any frequency and that the average spectral density of the voltage is proportional to the absolute temperature of the system T and independent of the conducting material or the conductor shape. Further experiments on various materials such as silver and sodium at different temperatures have proven to follow the same relation [21–24].

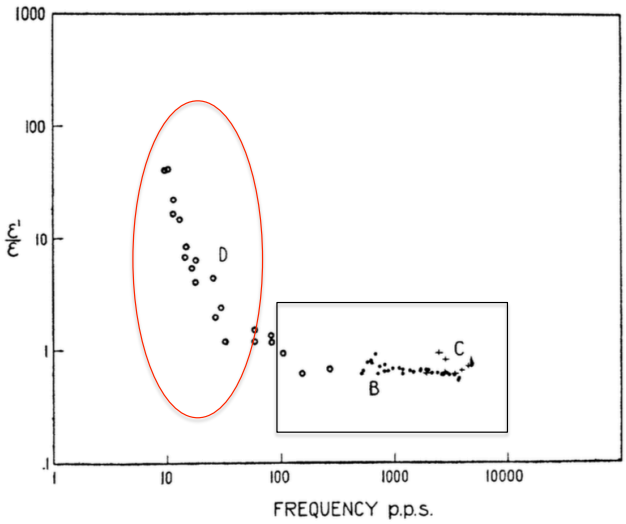

Figure 1.2: The spectral density observed by J. B. Johnson, adapted from the reference with permission[11]. It represents the noise power density divided by the theoretical shot noise power density versus the frequency.

Voltage fluctuations of charged carriers showed a frequency independent behaviour similar to the "white noise" pattern in the random walk scenario[25]. However this behaviour changes at low enough frequencies, where a frequency dependent behaviour is observed in Fig. 1.2 (oval region). This unusual behaviour, visualised by a power spectrum inversely proportional to the frequency was called "flicker noise", or "$1/f$ noise"[11]. Later, this behaviour appeared not to be restricted to Johnson's experiments on conductors; but rather was found to be common in semiconductors, glass, music, rise and fall of tides, flow of traffic, the stock market and earthquakes[10–17;26–31]. Driven by its prevalence, several experiments and interpretations were carried out to explore its origin.

1.3 Search for the $1/f$ Noise

1.3.1 Major Attempts

Based on data that he collected during 1967-1969, from measurements on semi-conductors F.N. Hooge, claimed in his important 1969 paper that $1/f$ noise is inversely proportional to the number of charge carriers in the conduction band[32;33]. Hooge's famous formula for the

power spectral density of the voltage was concluded to take the following form without any theoretical derivation:

$$S_v = \alpha \frac{V^2}{N f^\beta}, \tag{1.1}$$

where α is a proportionality constant found by Hooge to be equal to 2×10^{-3}, N is the number of charge carriers, and f is the frequency where $\omega = 2\pi f$. Here, the power law exponent was empirically found to be in the range of $0.8 < \beta < 1.4$.

Driven by this result, various propositions were published accepting or refuting Hooge's formula and exploring further dependence on other parameters[34–38].

One order of magnitude disagreement in the value of α was found by Voss and Clarke in their experiment on manganim[34]. To understand this contradiction, Hooge performed experiments on manganim in bulk where α was found to be smaller than 10^{-4}. However, the coefficient α derived from experiments on manganim with point contacts agrees with his previous result. Further experiments performed on gold and copper in bulk also showed a good agreement with the initially measured α value. To show coherence with those results, Hooge revised his previous conclusion regarding the so called "magic number" α to be not only material dependent but also temperature dependent. The debate over the applicability of Hooge's equation is still open.

The question of the source of $1/f$ noise appeared on a wider scale[34]. The flicker noise measured was not limited to conductors, but also appeared to be present in semi-conductors, where Hooge's formula was proven also to be untenable. It is worth pointing out that at this stage, researchers discarded the influence of the current on the $1/f$ noise; rather, it was considered to be an equilibrium phenomenon[39]. In all noise measurements, it was believed that the current is not continuous and a cutoff should exist, but none of the experiments succeeded in deciphering the cutoff[40;41]. There have also been many theoretical attempts to

explain the "flicker noise". The first attempt was postulated by McWhorter who attributed the noise to the movement of ions on and off the surface states[42–44]. This continuous movement characterises a random process driven by resistance fluctuations. To describe it, a Debye-Lorentzian spectrum equation is used:

$$S(\omega) \propto \frac{\tau}{\omega^2\tau^2 + 1}, \tag{1.2}$$

where τ is a time constant, and $\omega = 2\pi f$ is the frequency. Depending on the distribution function $F(\tau)$ used, a frequency dependent spectrum can be derived from an integration over Eq. (1.2). Particularly, if $F(\tau)$ is inversely proportional to τ, an inverse frequency power spectrum is derived: $S(\omega) \propto 1/\omega$. In his theory, McWorther proposed that the described resistance fluctuations obey the previous equation with the following time constant:

$$\tau = \tau_0 \exp(E/k_B T), \tag{1.3}$$

where E is the activation energy. If the energy distribution between E_1 and E_2 is considered to be uniform, the time constant τ will therefore be characterised by an inverse time distribution $1/\tau$ between τ_1 and τ_2 and a power spectrum inversely proportional to the frequency would then be obtained over the corresponding frequency range: $S(\omega) \propto (k_B T/\omega)/(E_2 - E_1)$.

This smooth derivation proposed by McWorther implies a direct temperature dependence and requires a particular description for the distribution of the energy barrier E. However, these two criteria were proven not to be universal and the problem remained unresolved. For instance, in semiconductors the noise dependence on temperature was shown to be weak with an inconsistent energy barrier[34].

An alternative idea based on the coupling of diffusion to resistance parameters was proposed by Richardson[45;46]. Using the diffusion equation, a power spectral density for the resistance can be derived. However, deriving a $1/f$ behaviour from it required several superficial

constraints, a feature that limited the applicability of the proposed theory[47].

One more theory evoking Hooge's formula was put forward by Handel between 1975 and 1977. Handel's idea was mainly derived from the energy of the emitted photons when electrons are scattered in conductors and semiconductors. The energy of the photon is not steady, but exhibits some fluctuations that lead to flicker noise. However, similar to the previous attempts, Handel's theory was mainly disproved through experiments performed by Tremblay and Martin, who succeeded to show that the derived spectral density is instead directly proportional to the frequency[48].

1.3.2 Temperature Dependence

A noteworthy point of view was proposed by Voss and Clarke who developed a major theory demonstrating the dependence of resistance fluctuations on temperature fluctuations.[10]

They found that the energy E for a canonical ensemble obeys the following relation:

$$E^2 = k_B T^2 C_v, \tag{1.4}$$

where C_v and T refer respectively to the heat capacity and the temperature of the sample. Once again, the derived relation proved to be application limited, suitable for metals but not for semiconductors.

They derived the temperature power spectrum $S_T(f)$ by solving the stochastic heat conduction equation in three dimensions:

$$\frac{\partial T}{\partial t} = D\nabla^2 T + \frac{\boldsymbol{\nabla} \cdot \mathbf{F}}{c}, \tag{1.5}$$

where c is the heat capacity per unit length and the random function $\mathbf{F}(\mathbf{x}, t)$ accounts for the random exchange through thermal conductance of energy between the mass and the reservoir.

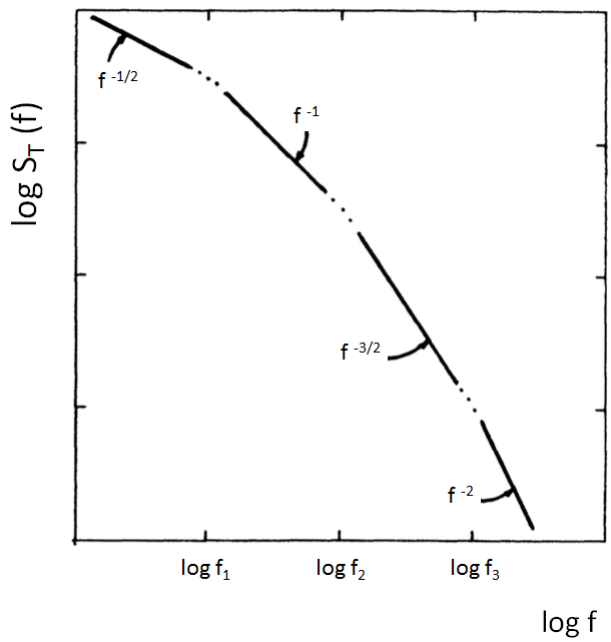

Figure 1.3: Temperature fluctuation spectrum $S_T(f)$ for partially correlated temperature fluctuations of a box $2l_1 \times 2l_2 \times 2l_3$ as a function of frequency. Adapted from Voss et clarke with permission[49].

By considering a conductor with sizes l_1, l_2, and l_3, Voss and Clarke divided the power spectrum $S_T(f)$ into four regions with three characteristic frequencies inversely proportional to the dimensions: $f_i = \dfrac{D}{2l_i^2}$ (Fig. 1.3). By replacing $\boldsymbol{\nabla} \cdot \mathbf{F}$ in Eq. (1.5) with an uncorrelated function $P(\mathbf{x}, t)$ in space and time, the shape of $S_T(f)$ showed a clear change[10;46;47;49]. Although this theory appeared promising, its applicability was limited to superconducting transitions.

1.3.3 Alternative Explanations and Systems

Weissman et al. in 1978 asserted that noise can be induced in systems with constant temperature due to a time-dependent current applied on a resistor but not from thermal fluctuations[50]. However, their work has shown that enthalpy fluctuations generates noise which does not resemble $1/f$, but instead it is similar to Johnson noise.

A particularly interesting explanation was later offered by Bak et al. in 1987, who attributed the $1/f$ noise to the mechanism known as self-organised criticality (SOC).[51;52]

No matter what the system is, a perturbation across it can cause a tiny noise to spread; it may even lead to an avalanche (see Fig. 1.4). The phenomenon can easily be visualised using the famous example of a sand pile. Starting with a steep slope the pile will collapse until the slope reaches a critical value at which the system reaches stability. Clearly, the behaviour and the stability point of the system depend on the magnitude of the employed force.

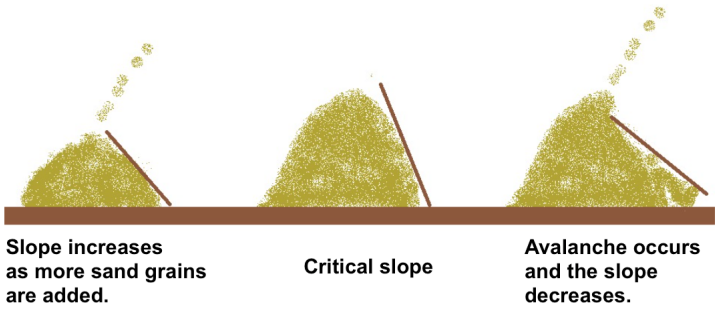

Figure 1.4: The sandpile model. Dropping an additional grain on a sand pile resting on a table may set off avalanches. The result depends on the steepness of slope that evolves to a critical state[53].

From measuring the number of modified clusters in response to an applied force, a power law could be observed with an exponent of 0.95[51]. Bak, Tang, and Weisenfeld generalised the model to describe any open system that generates $1/f$ noise. To explain their simulation-based work, Ramasawamy and Dhar provided a detailed analytical derivation to extract the $1/f$ noise in SOC[54;55]. Similarly, Hwa and Kardar, built a model that depends on the direction of the flow, which generated a different exponent[56–58].

1.4 $1/f^{\alpha}$ in DNA

The presence of $1/f^{\alpha}$ behaviour was found to be more prevalent after being discovered in DNA as well. By quantifying correlations and equal symbol power spectra, the evolution of information on DNA was measured by Voss in 1992. Measurements performed over different DNA categories including phages and mammals lead to a current power spectrum $S(f) \propto 1/f^{\alpha}$ with α varying from 0.71 to 1.16[59;60].

1.5 $1/f^{\alpha}$ Noise in Ion Channels

Given the prevalence of $1/f$ noise, in this thesis, we will approach the $1/f^{\alpha}$ noise problem from a different perspective. The $1/f$ noise I am interested in, is generated in nanopores, nanometer-sized holes connecting two ionic reservoirs across an impermeable membrane. In effect, they are channels that control information transmission by neurons in the form of electrical signals carried by ions. These are biological pores formed by proteins in lipid membranes. They operate in response to a driving force induced by the voltage gradient variation across the pore membrane. In response, a gating process occurs, which allows ions to flow depending on the strength and type of the stimulus they receive, thereby called ion-channels.

1.6 Introduction to Ion Channels

> *You don't need to use your workday circuits on a Sunday, but to keep those channels open, your brain sends a ping through them every minute or so. The fluctuations are the brain's investment in maintaining its circuits online.*
>
> Winifred Gallagher

The many types of ion channels that exist have different functionalities. Each part of the body is governed by its corresponding type of channels; for example "isoforms" are predominantly present in the brain. Different channels respond to different stimuli. Ligand-gated ion channels are activated by neurotransmitters, others are voltage sensitive, while hybrid channels react to both types of stimuli.

Ion channels are heavily present in the axons' initial segment of a neuron, where the concentration of potassium ions is much higher inside the axon membrane. The concentration of sodium ions however, is much higher outside the membrane. Due to the charge difference between the interior and exterior of the channel, a resting potential E exists ranging between -60 and -70 mV and a concentration gradient is present[61]. In particular, nanopores are being

used to study the properties of translocating biological molecules; to count them, measure their size and translocation velocity, or even determine their sequence as in the case of DNA and RNA[62–65].

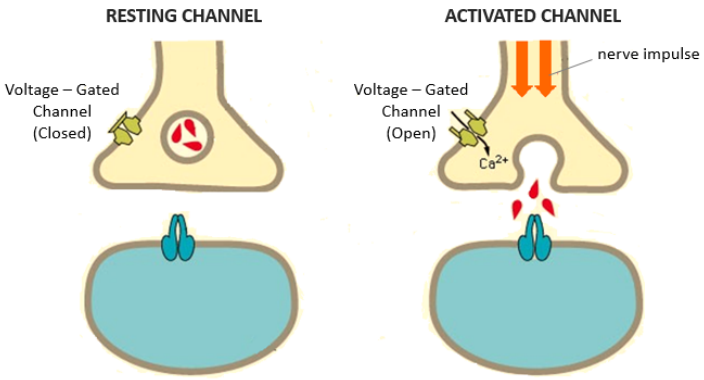

(a) Structure of ion-channels

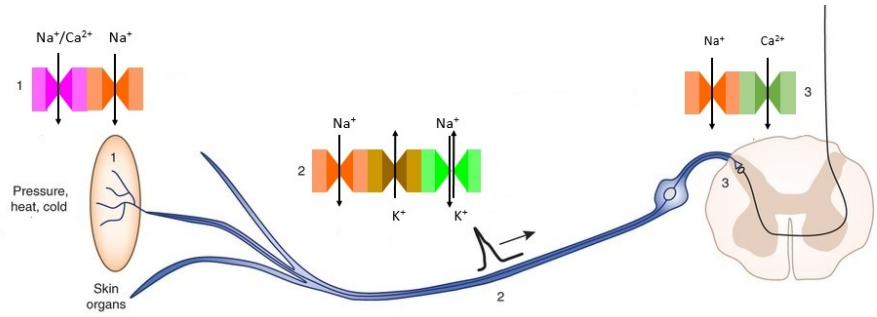

(b) Axon of a neuron

Figure 1.5: a) The structure of an ion channel showing the gating process. b) Ion channels across a neuron.

1.7 Ions Channels: What are they?

Bounded by membranes of prokaryotic and eukaryotic cells, ion channels are proteins or protein complexes that form a pore controlling the passage of ions. They tell us to move our hand back when we feel something hot or guide our hand movement when drawing on a paper. These transport systems play a crucial role in processing any signal through the nervous system, for example in initiating muscle contraction, or even in pancreatic secretion. Four ion types govern most of the processes K^+, Na^+, Cl^-,and Ca^{2+}. The classification of ion channels can be based on three properties that will be hereafter elaborated: selectivity,

gating, and conductivity[66–83].

1.7.1 Selectivity

Ion channels are selectively permeable to specific types of ions at a specific rate. Typically some channels are only permeable to calcium ions Ca^{2+}, others only to potassium ions K^{+}, while others only allow sodium ions Na^{+} to flow through[84;85]. However, how does a potassium channel distinguishes potassium ions from sodium ions? Although both types of ions are monovalent, spherical alkali cations, the channel succeeds in allowing one type of ions to flow and blocking the other type through its ion specifity feature. The radius of a potassium channel is comparable to potassium ions radii, a size selectivity characteristic that will not allow any ion of bigger radius to flow. Nevertheless, this feature is not applicable to sodium ions which have smaller radii. In this condition interaction within the selectivity filter of the pore plays a major role. When a potassium ion travels though the channel, it loses its solvation cage of H_2O due to the selectivity filter size, however due to its exact size, it builds interactions with amino acids along the wall. Small sodium ions, because of their size will not be able to build strong bonds and therefore the amount of energy released will not be equivalent to the energy needed to break the bonds between the water and sodium ions. Therefore the flow of sodium ions through potassium channels would not be successful as extra energy would be required.

1.7.2 Gating

Ion channels are said to be gated when they respond to a stimulus and open to allow the flow of ions or close to block the flow of ions. There exists various types of stimuli that make the channel excitable. Among them we list the Ligand gated ion channels that respond to the binding of a small molecule to the channel protein, mechanosensitive channels responsive to a pressure change, members of the transient receptor potential (TRP) channel family

that respond to a change in temperature, and voltage gated ion channels which respond to the change in the transmembrane potential that is discerned by charged segments of the channel protein. The rate at which ions flow through a selective open channel is very high and can exceed 10^6 ions/s[86–91]. As will be shown later, by controlling the flow of ions, the gating process plays a crucial role in controlling the membrane potential and in processing the electrical signal along the membrane.

1.7.3 Conductivity

For each channel type to conduct the solute, the following process is carried out. The fluid surrounding the channel is characterised by a higher number of cations on one side of the channel opposing a region richer in anions, a situation that indicates the presence of a potential difference (Fig. 1.6).

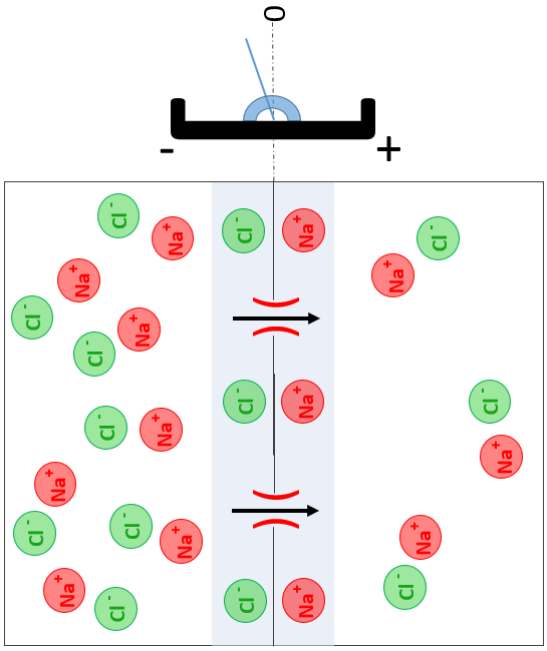

Figure 1.6: An illustration of sodium selective ion-channel separating a concentration gradient of salt NaCl. Sodium ions Na^+ will move against the gradient from left to right.

1.7.3.1 Move towards Equilibrium

We consider a channel that is only Sodium (Na^+) permeable, and a membrane separating two solutions characterised by different concentration of salt NaCl with no membrane potential. Driven by the concentration gradient, the sodium ions will start diffusing down across the channel. The diffusion of sodium ions induces a potential difference across the membrane with an excess positive charge building on the opposite side of the membrane[92–94]. The selectivity of the channel will forbid the movement of anions across the membrane to reach equilibrium, thereby a charge difference will persist. However, sodium driven to the opposite side of the channel will eventually build up an electrical force that will counter the flow of sodium itself. As a result of this electrical gradient, the positive side will start repelling sodium ions Na^+. Ions will flow down these gradients until the diffusional force balances the opposing electrical force and the system acquires an equilibrium Nernst potential $E = E_{\mathrm{Na}}$.

Using the well known Nernst equation, a relation can be built between the concentration of sodium inside the channel $[\mathrm{Na_i}]$ and its concentration outside the channel $[\mathrm{Na_o}]$ as following:

$$E_{\mathrm{Na}} = \frac{RT}{F} \ln \frac{[\mathrm{Na_o}]}{[\mathrm{Na_i}]}, \tag{1.6}$$

where R is the universal gas constant, T is the temperature in Kelvin, and F is the Faraday constant. In summary, E_{Na} in Eq. (1.6) has two indications: on one hand, if the membrane potential E is equal to E_{Na}, the net flux would be zero and there would be no flow of Na^+ ions. On the other hand, in a Na^+ selective pore, Na^+ ions will flow and the membrane potential will vary to reach the equilibrium potential $\mathrm{E_{Na}}$.

Membranes permeable to K^+ and Cl^- ions follow a similar process. Na^+ ions will contribute to moving the neuron potential towards its positive equilibrium potential E_{Na} while K^+ ions will change the membrane potential towards its negative equilibrium potential E_{K}. The

final membrane potential of a neuron containing channels permeable to both potassium and sodium ions will be closer to the equilibrium potential of the ions with higher permeability.

1.7.3.2 Ion Channels: An Electrical Circuit

From a physics perspective, the ion channel system can be compared to an electrical circuit built from a capacitor, a resistor, and a battery. Comparable to a capacitor, the membrane containing the channel plays the role of an insulator separating two conducting solutions, whereas the channel mimics the resistor, and finally the gradient is comparable to the electromotive force from the battery. Using this circuit, the channel conductivity can be summarized by reference to Ohm's Law. A relation between E_{Na}, the voltage E, the electrical conducatance G_{Na}, and the current I_{Na} can be built as follows:

$$I_{\mathrm{Na}} = G_{\mathrm{Na}}(E - E_{\mathrm{Na}}). \tag{1.7}$$

Therefore, by evaluating the channel current and voltage relation, extensive information was drawn about the channel behaviour. This relation was firstly proposed by Hodgkin and Huxley, whose work is discussed in more details in the following section.

1.8 A Glimpse at the Hodgkin and Huxley Model

It was discovered by Hogkin and Huxley(HH) in 1952 that the response of the nerve does not depend on the flow of ions driven by the stimuli; instead it depends on the potential difference across the channel. Their proposed electrical circuit model gave a new physical description to biological ion channels that are now treated as voltage sensor gates[95].

1.8.1 Voltage Sensor Gates

Upon receiving a stimulus, the voltage across the membrane is varied, and the equilibrium is altered. If the voltage change is above a threshold value generally around 30mV, the cell is said to be depolarised. Due to this voltage change, sodium channels will open and sodium ions attracted by the concentration gradient will flow to the inside of the channel. In response to the increase in cations, the sodium channels will close and the potassium channels will open allowing the potassium ions to diffuse outside the channel. At this stage, a repolarisation is taking place as the inside of the channel is restored back to be more negative than the outside. The channel is said to have an action potential.

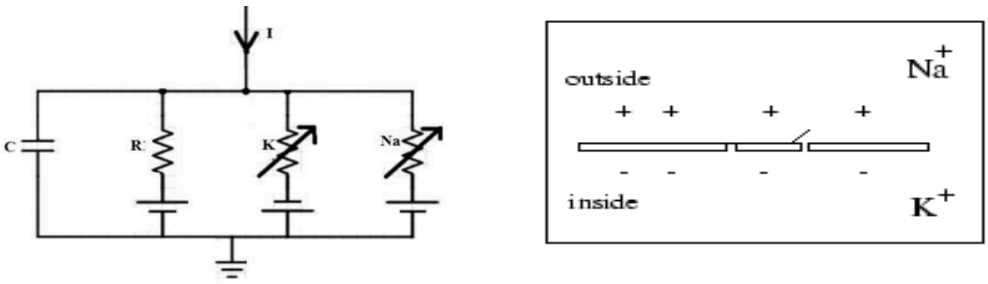

Figure 1.7: (Left panel) Electrical circuit representing the Hodgkin and Huxley model. The membrane is represented by the capacitor and the resistances of the sodium and the potassium gated channels are measured respectively by R_{Na} and R_K. The constant leakage resistance is measured by the resistor R. (Right panel)The membrane acts as a capacitor and separates the interior of the cell from the exterior.

Figure 1.5b shows that the axons have many channels and the action potential will be carried as a wave consecutively in a Markovian chain across all of them. Each ion in the pore is characterised by a critical driving force and the flow of ions is proportional to that force. Thereby, the main question answered by HH's work, was the source of the gating process. Isolating potassium and sodium ions from the channels allowed them to conclude that the flow of the sodium is independent of the ionic movement. Rather, they found that the flow of the ions depends on other membrane components characterised by a dipole moment that triggers the channel to open. To support this conclusion, they built a model composed of

a series of resistors and capacitors as shown in Fig. 1.7. Hodgkin and Huxley formulated the current components using current conservation across three types of channel, potassium, sodium, and an unspecified leakage channel with resistance R with the following total current:

$$I = I_{\mathrm{Na}} + I_{\mathrm{K}} + I_{\mathrm{L}}. \tag{1.8}$$

Expressing the total current in terms of the ionic voltage and the corresponding activation function, HH's differential equation of the voltage variation as a function of time was derived. The equation result was found to agree with experimentally measuremed action potential. This provided strong evidence for their proposed theory that the open-close mechanism is generated by the movement of membrane components due to a polarity change that can be viewed as a torque. Further, they asserted that the number of charges inside the membrane is independent of their number outside.

1.9 Beyond the Hodgkin and Huxley Model

1.9.1 The Flow of Ions

While the model developed by HH in 1952 helps to understand the behaviour of the ion channel, mainly the gating process, it did not describe the flow of ions inside the channel, its characteristics, or how the potential difference across the pore is generated. Measuring and studying the ionic current passing through a nanometer-scale membrane pore has emerged over the past couple of decades as a versatile technique to study nanometer-scale transport processes. In the following sections an overview of the most focussed researches on understanding the current flow through ion channels will be introduced.

1.9.2 Brownian Motion and Thermal Noise

The ions around the channel electrodiffuse across the pore, in an intrinsic Brownian motion that alters the channel's electrical properties. Due to this random motion, successive collisions between ions themselves and their surroundings take place, generating electrical fluctuations characterised by what was previously introduced as the thermal noise.

Apart from limiting the measurement accuracy, the noise level can sometimes be used to study the microscopic properties of a nanofluidic system, such as the adsorption of molecules on the walls of a nanometer-scale cavity.[96]. At low frequencies, the power spectrum $S(\omega)$ of the ionic current through an electrolyte-filled nanopore typically follows a power law $S(\omega) \propto 1/\omega^{\alpha}$ with $\alpha \approx 1$, or $1/f$ noise[97;98]. At high frequencies, $S(\omega)$ or $S(f)$ is dominated by thermal or capacitive noise[98;99].

1.10 Johnson Noise in Ion Channels

The $1/f^{\alpha}$ noise problem remained heavily debated and its exploration went beyond metals, and semi-conductors, to biological systems. In 1965, Verveen and Derksen first succeeded in revealing the presence of $1/f^{\alpha}$ noise in the ionic current power spectral density in biological pores[100]. Their experiment was mainly based on the analysis of ions behaviour in myelinated nerves subject to random stimulations that lead to different action potentials. The power spectrum of the membrane voltage revealed a $1/f$ behaviour over several kHz frequency range.

As with electronic devices, several attempts to find an explanation for this behaviour took place. Current measurements were performed on the brain, and axon of different types of biological organisms, which induced various suggestions about the source of $1/f$ noise.

The power spectral density $S(f)$ was found by Conti et al. to be independent of the temperature within a range of $9.5 - 20°\mathrm{C}$ and to be inversely proportional to the square of the

current, an idea upon which scientists agree[101]. Furthermore, Fishman et al. suggested that $1/f$ noise is independent of the surface area of the axon, a conclusion that was later modified to find instead an inverse relation between the spectral density and the system size[102].

Despite all the measurements performed, the origin of the $1/f$ noise remained unknown. Several questions were also addressed. Why should a system in equilibrium exhibit a $1/f$ noise? What is its source, charges, membrane, or voltage?

To approach the problem more closely, Fishman and Poussart fabricated artificial pores in axons[103;104]. Driven by the empirical relation derived by Hooge[32], experiments were again conducted to explore its validity on biological pores[104–106].

Despite their attempts, they did not find a single α that could obey the equation at different ion concentrations, instead they related the $1/f$ noise to current leakage[107]. Several other questions were asked trying to explore the dependence of $1/f$ noise on the charge number or on the ion mobility[50].

On one hand, for the impulse to propagate along the axons, a Markovian process takes place; a scenario that according to Weissman might be playing a role in generating the $1/f$ noise[50]. On the other hand, other attempts tried to link the noise with enthalpy fluctuations. This proposition was ruled out by Dutta and Horn in 1981, when they showed it to be very negligible with respect to the generated noise[50]. Finally, Bak et al. preserved an alternative theory that linked the power law in any system to spatial organisation. Numerically, they proved that a power law is evoked when an avalanche takes place[52].

1.11 Recent developments

Further experiments were conducted and many propositions were made, but the final picture remained inconclusive[108–112]. In the international conference on unsolved problems of noise in 1998, Bezrukov et al. reported that the noise in ion channels is caused by "the equilibrium conductance fluctuations related to the conformational flexibility of the channel pore structural

constituents". By those words, Bezrukov eliminated the role of the ions and focused on the state and behaviour of the membrane. In an attempt to support his proposition, experiments were conducted on Maltoporin channels. By measuring the power spectral density generated by those channels in their open state, a $1/f$ dependence at frequencies lower than 100 Hz was noticed. To explain those results, Bezrukov et al. defended their previous claim by attributing the results to the channel behaviour characterised by the conductance variation [113]. Specifically, they linked it to conformational change in the pore without a total closure; a conclusion that is in clear support of their previous claims.

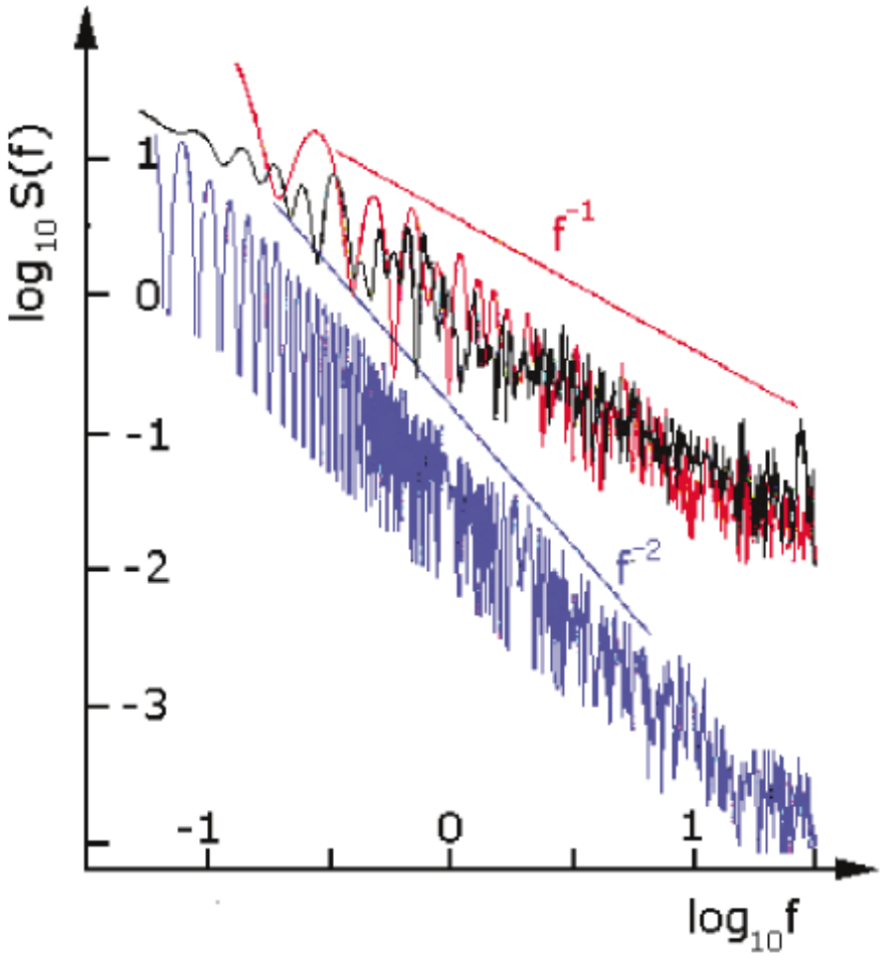

Figure 1.8: Current power spectra of biological channels (red) and synthetic channels (black and blue). The black and the red curves are extracted from channels that exhibit a gating process but the blue curve corresponds to the current spectrum of an open channel. Adapted from Siwy et al. with permission [114].

Driven by the explanation of Bezrukov et al. Siwy and Fulinski performed experiments on

fabricated biological, and synthetic nanopores[114]. The corresponding current power spectral densities were measured at various potentials to characterise the three different channel states: closed, open, or random transitions between open and closed states. Their measurements revealed two different power law behaviours. Open channels lead to a $1/f^{\alpha}$ with a remarkable $\alpha = 1.9$ whereas closed channels did not decisively lead to $\alpha = 1$, and dwell times in BIO and PET behaviour lead to $\alpha = 1.1 \pm 0.1$ (Fig. 1.8). From further investigations to support their results, Siwy et al. reached a conclusion that strengthened Bezrukov's preliminary results by associating the flicker noise to the movement in the channel subunits. The conclusion of Siwy et al. was further developed by Hänggi and Goychuk who focussed on understanding the non-Markovian process and how it relates to $1/f$ noise[115–118].

Goychuk and Hänggi developed a new theory for the gating process. The opening and the closing states of the channel were described as two stochastic processes that happen at independent time intervals. In their theory, Hänggi and Goychuk use the McNamara-Wiesenfeld two-state Markov theory. The survival probabilities $\phi_{1,2}$ for the open and closed states respectively can be described by the following equations:

$$\phi_{1,2} = \int_{\tau}^{\infty} \psi_{1,2}(t)dt,$$

$$\psi_{1,2}(\tau) = \nu_{1,2} \exp(\nu_{1,2}\tau),$$

where $\psi_{1,2}$ represents the residential time distributions, and $\nu_{1,2}$ the transition rates.

Deriving the propagator of the unperturbed two states $\prod(t|t_0)$, and combining it with the fluctuation theorem, they built the power spectral density equation, and the signal to noise ratio at low and high frequencies. To apply their theorem to ion channels, they derived the characteristic residential times τ_1 and τ_2 and particularly the power spectral density $S(N)$. At low frequencies, the power spectrum of conductance fluctuations obeys $S_f = 1/f$, which

agrees to some extent with the result previously concluded by Siwy et al.. To generalise their work Goychuk and Hänggi studied the stochastic resonance in a three state system instead of only two state system. To exactly mimic the ion channel in its thermal equilibrium states, they distinguished between open, closed, and inactivated states. They described the gating process by non-exponential, power law residence time probability distribution, and they characterised the diffusion process in each state.

Goychuk and Hänggi not only presented a comparison that showed a good agreement with their previously developed theory for the two state non-Markovian system, but they have also provided a tool for experimentalists to choose the molecules that show the appropriate stochastic resonance.

A different explanation for the $1/f$ noise contradictory to the explanation by Siwy et al. was developed by Banarjee et al.. Inspired by Bak et al., they developed a different model based on self-organised criticality in ion channels[119]. They showed that the sand organisation during an avalanche resembles the behaviour of ions when crossing the membrane. Their experiments were performed on voltage dependent anion channels, in which they showed that fluctuations depend on the amount of ions crossing the pore at different time intervals. They derived an expression for the current power spectrum from the probability of current fluctuations occurring due to ion correlations. From that model, they concluded that $1/f$ flicker noise can be created by ions blocking the pore randomly during their passage. However, the proposition of Banerjee et al. proposition was not definitive. Instead, as it is shown in the following section, numerous experiments were further conducted aiming at gaining a better understanding of the $1/f$ noise and the current flow of ions especially after succeeding in fabricating solid state pores.

1.12 Solid State Pores

The study of the flicker noise became more frequent after a major improvement in the fabrication of artificial pores that were reported in the famous Dekker review article[120] (see Fig. 1.9a). In their fabrication, they used silicon to create solid-state nanopores, later used to study ionic conductance and DNA translocation[121–126]. The solid-state pores showed a clear advantage over biological pores, but they still exhibited the same $1/f$ noise[98;120;127]. Driven by the noise ubiquity, the same group explored the source of the noise and suggested that it is created by nanobubbles occupying the nanopore[128]. After studying the conductance profile for pores with various diameters when moved across a laser beam, they noticed that conductance reaches a maximum and the noise a minimum when the pore is located at the centre of the beam, where the temperature is maximized. Smeets et al. confirmed that hydrophobicity of the channel and its surface contribute to form nanobubbles that play a role in the occurrence of the $1/f$ noise[129].

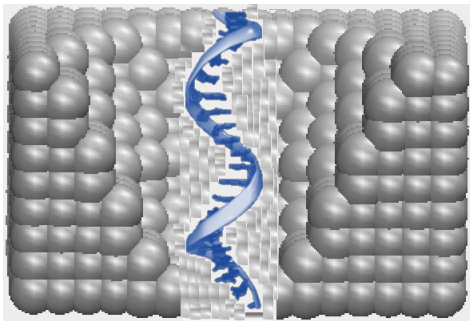

(a) DNA translocation

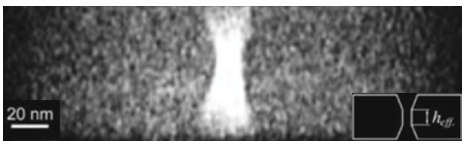

(b) Solid state pores

Figure 1.9: a) An illustration of a single-stranded DNA translocating through a SIN nanopore. Credit: Robert Johnson[130]. b) SIN solid-state nanopore fabricated by ion beam drilling. Adapted from Shi et al. with permission[131]

.

Despite this proposition, Smeets et al., published a different characterisation of the noise the following year. From studying ionic fluctuation in solid state pores, they went back to support Hooge's conclusion. Increasing the salt concentration prompts an increase in conductance that triggers a noise power decrease. After extracting the number of charge carriers inside

the pore, they used it to fit the power law using Hooge's formula:

$$\frac{S_I}{I^2} = \frac{A}{f},$$

where $A = \frac{\alpha}{N_c}$, A is the value of the noise power and N_c is the number of charge carriers. They found that Hooge's parameter α is equal $(1.1 \pm 0.1) \times 10^{-4}$, a comparable value to what has been previously found in electronic devices[98].

From another perspective, fractional Brownian motion, which can be used to describe $1/f$ noise, also governs subdiffusive motion of molecules under confinement[132]. Based on careful analysis of noise measurements in solid-state pores filled with ionic liquids, Tasserit *et al.* reached the conclusion that $1/f$ noise is caused by a cooperative effect in the ionic motion[133]. In computer simulations, $1/f$ noise has only been observed in nanochannels where the single-file motion is enforced artificially[134].

After decades of development and trials, the first commercially available nanopore sequencing device was introduced last year[135]. This revolutionary apparatus allows DNA sequencing at high speed and low cost, however its main challenge is error correction. Because noise reduction is complicated, or even fundamentally impossible due to the low number of ions involved, noise characterisation becomes extremely important. This technology triggered more interest in pores and more research into the flicker noise area.

The continuous growth in the nanopore field promulgated more publications in the area. Other explanations of $1/f$ noise were provided again by the Dekker group through work on graphene nanopores. Trying to examine the applicability of Hooge's magic number on graphene pores, their measurements showed that the noise is independent of charge fluctuations[97]. Alternatively, the noise is thought to depend on layer thickness, a conclusion that was supported by further experiments on boron nitride membrane[136].

1.13 A Quick Look at the Content

As it was thoroughly shown $1/f$ noise has always been approached from an experimental perspective. However, a systematic theoretical investigation of the noise spectrum in nanopores filled with an aqueous electrolyte has been lacking so far. Below we outline the content of each chapter of this thesis and give an overview of the main questions addressed and new questions proposed.

In Chap. 2, we present a comprehensive theoretical analysis of the nonequilibrium noise spectrum of an ionic current through a rigid nanopore. We derive an analytical expression for the noise spectrum in the mean-field regime, providing a tool to analyze and interpret experimental results in both the high and low frequency limits. We proceed in our derivation by calculating the current density in an infinite box in real space, that we then map into a cylinder in Fourier space to extract the final expression for the current power spectral density. We show that the linearized mean-field theory predicts a plateau in the power spectrum at low frequencies, which has not been found in experiments, and a power law at high frequencies. These two features will be analysed in Chaps. 3, 5, and 6. A challenging and interesting problem would be to derive an analytical expression incorporating non-linear terms.

To extract the power spectrum of the current flow of ions, coarse grained Langevin-dynamics simulations of electric-field-driven monovalent ion transport through nanometer-scale pores have been performed using the many-particle simulation software Espresso. Details of the simulations are put forward in Chap. 3. A comparison between simulation results and analytical expression from Chap. 2 is also given. An agreement was found at high frequencies, while a discrepancy existed at low frequencies, recalling $1/f$ noise. The discrepancy is explained in terms of the role of ion-ion interactions, while this demonstration can provide a new guideline to overcome the question of $1/f$ noise.

The mathematical model laid out in Chap. 2 proved to be a tool to analyse the power

spectral density derived in Chap. 3. However, a simplified form for the current power spectral density can be derived when we ignore several terms. In Chap. 4, our work predicts that if we do not consider the screening effect of the concentration, and if we assume that positive and negative ions experience the same thermal noise, the current density acquires a reduced form that we integrate over a cross section instead of a confined volume. We explain the relation between both expressions and we address the question of the applicability of the simplified form. The similarity in behaviour sheds light on the role of various parameters characterising our system, and can be the key towards future investigations and experiments.

In Chap. 5, we elaborate more on the role of ion-ion interactions by considering lower ion concentrations. Besides biological nanopores, innovative technology allowed the fabrication of new solid state pores. Solid-state pores allowed more flexibility in modifying and understanding more properties. Among these we list charges on the pore wall, electric field, pore geometry, and valency. Here, we attempt to investigate the influence of those parameters on the current flow of ions. Contrary to reports in the literature, we find no significant dependence of the power spectrum on the surface charge density. The role of the gating process is as well approached using an oscillating channel. Varying other properties emphasized more the role of ion-ion correlation.

To develop our studies, in Chap. 6 our attention is shifted to hydrodynamics in ionic pores. To understand active matter, hydrodynamics interactions have always been a major point of interest, but not much is known about their role in ion channels. Here, we explore the effect of hydrodynamic interactions on the power spectrum of the current flow of ions. Using nonequilibrium Langevin-dynamics simulations of an electrolyte with explicit solvent particles, we investigate the effect of fluid flows on the power spectrum of ionic nanopore currents. At low frequencies, we find a power-law dependence of the power spectral density, with an exponent depending on the ionic density. Surprisingly, however, the exponent is not affected by the presence of the neutral solvent particles. Although a direct comparison

with experimental results is currently not feasible, this result can lead to many experiments investigating the role of hydrodynamics in the future.

CHAPTER 2

Theoretical Study of Current Fluctuations

The secret of change is to focus all of your energy not on fighting the old, but in building the new.

Socrates (470BC-399BC)

2.1 Introduction

The noise generated in nanopores, is extracted from the current power spectral density $S(\omega)$ as a function of the frequency ω.

In an attempt to understand the source of the noise from a different perspective, in this chapter, we develop a theoretical formulation to study the noise spectrum in the mean-field regime.

For this purpose, we start by considering the flow of ions along a cylindrical pore in real space. Because of the complexity of extracting an exact expression describing the current fluctuations of ions in a bounded domain, an *ad hoc* approximation scheme in which we map our system to an infinite $3D$ box that we subsequently map to a cylinder in Fourier space. When integrating over the Fourier modes, we impose infrared and ultraviolet cutoffs on the wave-vectors using the corresponding geometric characteristics along each direction.

Following those steps we derive an expression for the current density fluctuations that we use to get the final expression describing the current fluctuations $S(\omega)$.

2.2 Theoretical Formulation

We consider a system consisting of a cylindrical nanopore of length L and radius R surrounded by two reservoirs of monovalent ions. We model the electrolyte filling the nanopore as ions of valency ± 1 in implicit water, where ions are considered to be surrounded with a continuous medium[137;138].

Because the ionic current through the system is ultimately determined by the flux through the pore, we base our model on the ion flux density $\boldsymbol{J}^{\pm}(\boldsymbol{x}, t)$ inside the nanopore, with $\boldsymbol{x}$ denoting the position in three dimensions and t denoting the time.

We denote the flux densities of the positive $(+1)$ and negative (-1) ions inside the nanopore as $\boldsymbol{J}^{\pm}(\mathbf{x}, t)$ respectively, and the corresponding thermal noise parameter as $\boldsymbol{\eta}^{\pm}(\mathbf{x}, t)$.

The dynamics of each ionic species satisfies the continuity equation:

$$\frac{\partial C^{\pm}}{\partial t} + \boldsymbol{\nabla} \cdot \boldsymbol{J}^{\pm} = 0, \tag{2.1}$$

where $C^{\pm}(\mathbf{x}, t)$ denotes the corresponding concentrations.

The ionic fluxes $\boldsymbol{J}^{\pm}(\mathbf{x}, t)$ are composed of diffusive and deterministic components, as follows:

$$\boldsymbol{J}^{\pm} = -D\boldsymbol{\nabla}C^{\pm} + \mu e C^{\pm}(\mathbf{E} - \boldsymbol{\nabla}\phi) - \boldsymbol{\eta}^{\pm}, \tag{2.2}$$

where e denotes the elementary charge, $\mathbf{E}$ is the applied electric field, μ is the mobility of the ions, and the electrostatic potential ϕ satisfies Poisson's equation:

$$-\nabla^2\phi = \frac{4\pi e}{\epsilon}(C^{+} - C^{-}), \tag{2.3}$$

with ϵ being the dielectric constant of the medium.

To simplify our equations, we define the Bjerrum length $\ell_B = \dfrac{e^2}{\epsilon k_B T} = 7$ Å, where k_B and T refer respectively to the Boltzmann constant and the temperature of our system. Besides, we define the dimensionless potential $\psi = \dfrac{e\phi}{k_B T}$, the inverse of the Debye length κ via $\kappa^2 = 8\pi\ell_B C_{\text{pore}}$, and the reduced electric field $\boldsymbol{\mathcal{E}} = \dfrac{e\mathbf{E}}{k_B T}$. The diffusion coefficients for the ions are considered to be equal $D^+ = D^- = D$, and independent of the ionic concentrations. This assumption is obeyed in KCl and KNO_3 solutions[139].

2.3 Boundary Conditions

To solve the above proposed system of equations in the given geometry, we need to specify the relevant boundary conditions. The equations are to be solved in a bounded domain Ω with defined boundary $\partial\Omega$. In Fig. 2.1(a), we illustrate a $3D$ ion channel geometry in which the coordinates $(x_{\parallel},\ x_{\perp 1},\ x_{\perp 2})$ are defined. The system is projected onto a $2D$ space in Fig. 2.1(b).

The channel walls and the separating surfaces are considered to be impenetrable; *i.e.* they block ions from flowing through them. For this criterion to be achieved, using the unit vector normal to the walls $\mathbf{n}$, we set the no-flux boundary condition for the fluxes:

$$\begin{cases} \boldsymbol{J}^+(\widetilde{\mathbf{x}}) \cdot \mathbf{n} &= 0, \\ \boldsymbol{J}^-(\widetilde{\mathbf{x}}) \cdot \mathbf{n} &= 0, \end{cases} \tag{2.4}$$

where $\widetilde{\mathbf{x}} \in \partial\Omega$. The equations in (2.4) are applicable for all particles in the 3-dimensional space. Due to the Neuman no-flux boundary condition, regardless of the number of ions flowing in and out of the channel, a number conservation condition and an electroneutrality condition should be maintained. For this condition to be obeyed, the total sum of each of the anions and cations in the three chambers forming the system (along the channel, the upper

reservoir and the lower reservoir) has to be maintained constant, as following:

$$\begin{cases} \sum_{i=1}^{N} z_i = 0, \\ \\ N_{\text{Channel}}(t) + N_{\text{Upper Reservoir}}(t) + N_{\text{Lower Reservoir}}(t) = N(t=0), \end{cases} \tag{2.5}$$

where $N(t)$ accounts for the number of ions at any time t.

Finally, for the Poisson equation, the boundary condition depends on our assumption regarding the charges on the pore wall. If charges are added to the wall with a charge density σ_s, a Neumann boundary condition is imposed using the normal derivative of the potential as follows:

$$-\frac{\partial \phi}{\partial n} = \mathbf{E} \cdot \mathbf{n} = \frac{\sigma_s}{\epsilon_0}, \tag{2.6}$$

with ϵ_0 being the permittivity of free space. If we deal with uncharged walls, the normal derivative of the potential will vanish:

$$-\frac{\partial \phi}{\partial n} = \mathbf{E} \cdot \mathbf{n} = 0. \tag{2.7}$$

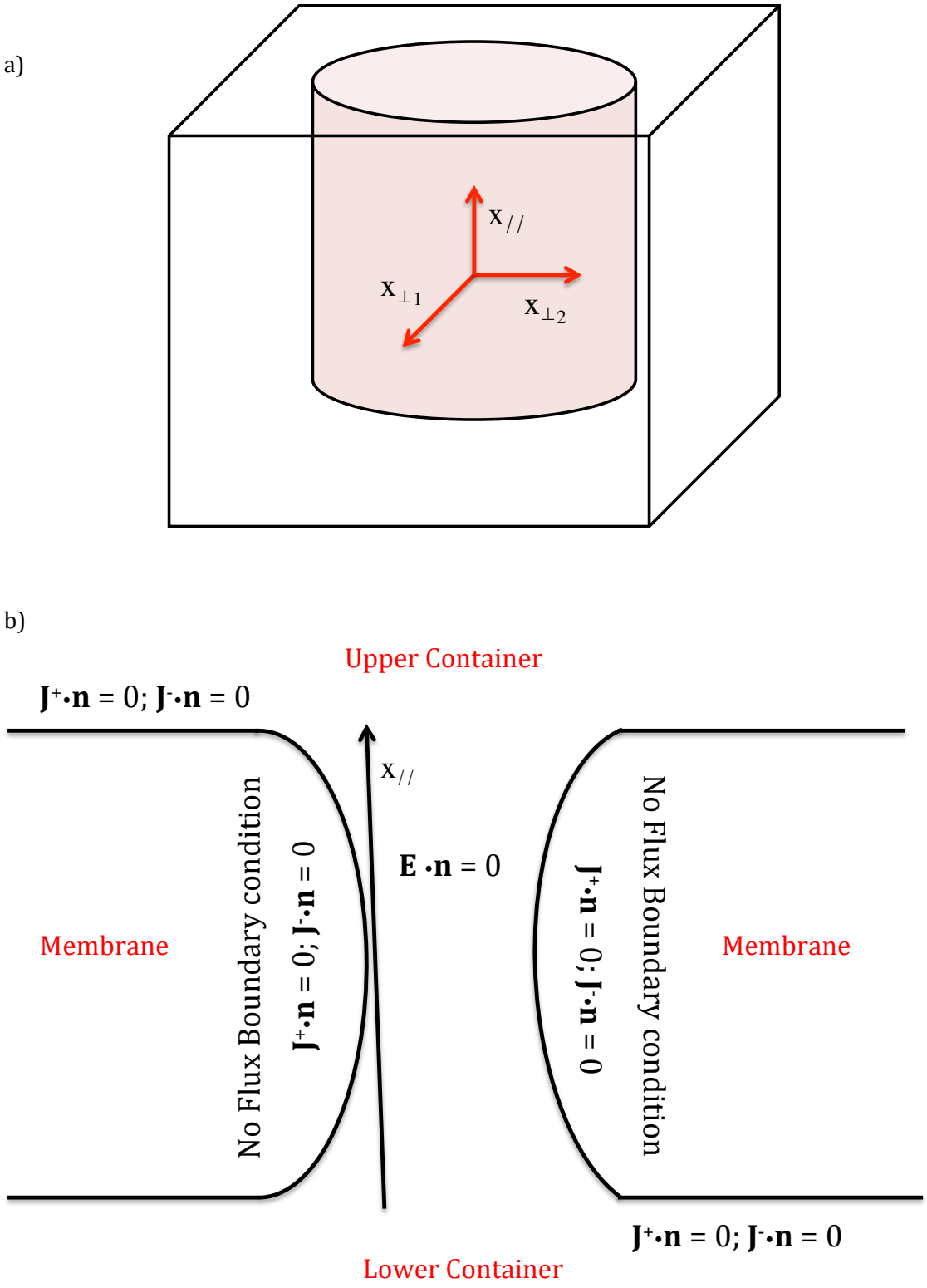

Figure 2.1: (a) The ion channel geometry in 3-dimensional space. (b) A projection of the channel geometry in 2-dimensional space. The membrane walls are flux free and the normal component of the potential is set to 0 as there is no charge on the pore wall.

2.3.1 A Major Simplification of the System

Solving the system of equations we have developed, namely (2.1), (2.2), and (2.3) subject to the above boundary conditions in the specified geometry is a formidable task. Instead of attempting that, we simplify the problem by considering an infinite $3D$ channel and implement the geometric features at a later stage. Using this approximation, the boundary conditions could be ignored, and the ions would be modeled in the infinite three-dimensional space, using the following coordinates: $x_{\parallel}$, $x_{\perp 1}$, and $x_{\perp 2}$.

Involving the newly established translational symmetry, we use a transformation from the real space to the Fourier space, which allows us to describe the system by a wave vector $\mathbf{q}$ characterised by the following conjugate components ($q_{\parallel}$, $q_{\perp 1}$, and $q_{\perp 2}$) along the three dimensions (See Fig. 2.2). By using this mapping, the upper and the lower limits of the conjugate components provide us with an opportunity to incorporate the geometric features of the system in an approximate manner as it is done in solid state physics. In reciprocal space, the lattice spacing of dimension L^{-1} is set by the real space lattice of dimension L. In our system, the extent of $x_{\parallel}$ is controlled by the channel length L, and the longitudinal dimensions $x_{\perp 1}$, and $x_{\perp 2}$ are limited by the channel radius R. Using those considerations, the resulting lower limits for $q_{\parallel}$, $q_{\perp 1}$, and $q_{\perp 2}$ are respectively π/L, π/R, and π/R.

Similary, if we consider the lattice space size Λ as the lower limit of the real space components $x_{\parallel}$, $x_{\perp 1}$ and $x_{\perp 2}$, then the Fourier space components will be controlled at the upper limit by π/Λ[140;141].

Another approximation is related to how we simplify the shape of the Brillouin zone, which is warranted as the information about the exact geometry of the boundary cannot change the main features of the result[140–142].

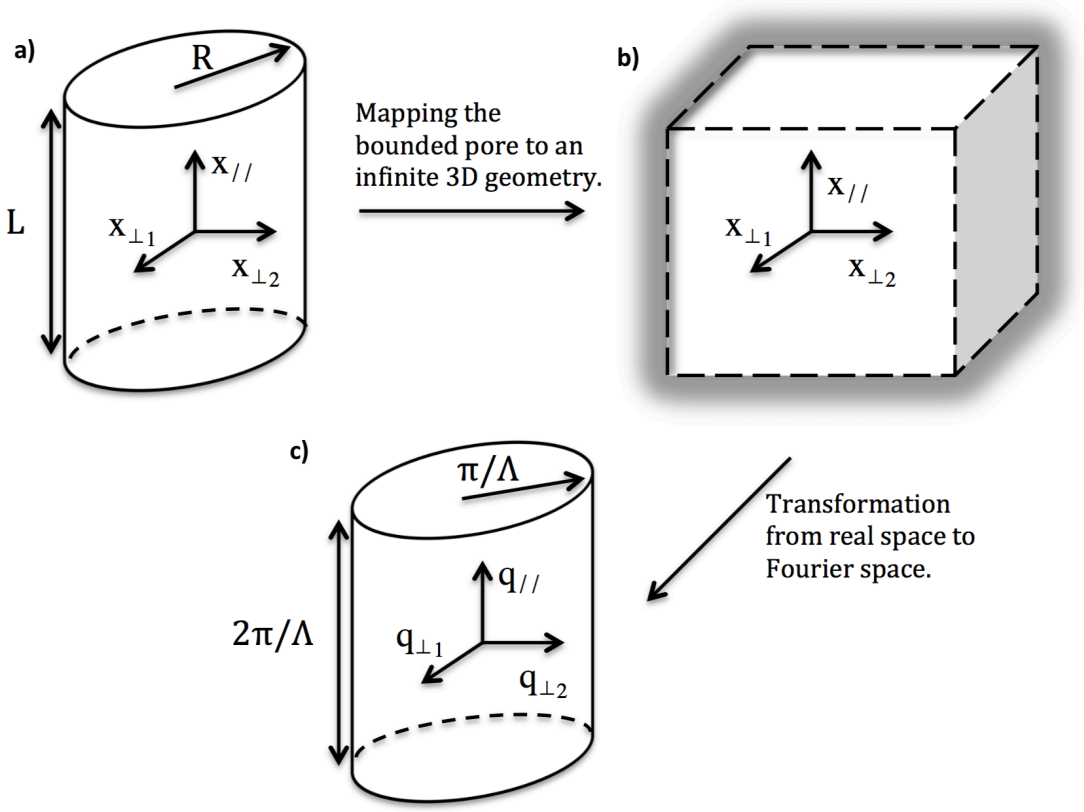

Figure 2.2: A schematic drawing illustrating the transformation from a bounded cylindrical geometry to an infinite 3D space then to a confined cylindrical domain in Fourier space. The small length scale cut-off of Λ is implicit in (a), and the small wavelength cut-offs of π/L and π/R in wavevector space are not shown in (c).

2.3.2 The Governing Equations in Fourier Space

Interested in the fluctuations in the ionic concentrations C^+ and C^- around the average concentration C_{pore}, we define respectively: $C^+ = C_{\text{pore}} + \delta C^+$ and $C^- = C_{\text{pore}} + \delta C^-$, where $\delta C^\pm$ refer to a small perturbation obeying $\delta C^\pm << C_{\text{pore}}$. We perform the Fourier transform of Eq. (2.2) that leads to the positive and negative ions flux densities as functions of the

wave vector $\mathbf{q}$ and the frequency ω,

$$\begin{cases} J^+(\mathbf{q},\omega) = D(i\mathbf{q}+\boldsymbol{\mathcal{E}})\delta C^+(\mathbf{q},\omega) - \boldsymbol{\eta}^+(\mathbf{q},\omega) \\ \qquad\qquad + i4\pi\ell_B D\int \frac{d\Omega}{2\pi}\frac{d^d\mathbf{k}}{(2\pi)^d}\Big[\frac{(\mathbf{q}-\mathbf{k})}{(\mathbf{q}-\mathbf{k})^2}\Big]\delta C^+(\mathbf{k},\Omega)\big[\delta C^+(\mathbf{q}-\mathbf{k},\omega-\Omega) - \delta C^-(\mathbf{q}-\mathbf{k},\omega-\Omega)\big], \\ \\ J^-(\mathbf{q},\omega) = D(i\mathbf{q}-\boldsymbol{\mathcal{E}})\delta C^-(\mathbf{q},\omega) - \boldsymbol{\eta}^-(\mathbf{q},\omega) \\ \qquad\qquad - i4\pi\ell_B D\int \frac{d\Omega}{2\pi}\frac{d^d\mathbf{k}}{(2\pi)^d}\Big[\frac{(\mathbf{q}-\mathbf{k})}{(\mathbf{q}-\mathbf{k})^2}\Big]\delta C^-(\mathbf{k},\Omega)\big[\delta C^+(\mathbf{q}-\mathbf{k},\omega-\Omega) - \delta C^-(\mathbf{q}-\mathbf{k},\omega-\Omega)\big]. \end{cases} \tag{2.8}$$

In Fourier space and in terms of $\delta C^+(\mathbf{q},\omega)$ and $\delta C^-(\mathbf{q},\omega)$, Eqs. (2.1) and (2.3) read:

$$\begin{cases} \psi(\mathbf{q},\omega) = \dfrac{4\pi\ell_B}{q^2}\big[\delta C^+(\mathbf{q},\omega) - \delta C^-(\mathbf{q},\omega)\big], \\ \\ i\omega\delta C^+(\mathbf{q},\omega) = -Dq^2\delta C^+(\mathbf{q},\omega) + i\mathbf{q}\cdot\boldsymbol{\mathcal{E}}D\delta C^+(\mathbf{q},\omega) - i\mathbf{q}\cdot\boldsymbol{\eta}^+(\mathbf{q},\omega) \\ \qquad\qquad - 4\pi\ell_B D\int \frac{d\Omega}{2\pi}\frac{d^d\mathbf{k}}{(2\pi)^d}\Big[\frac{\mathbf{q}\cdot(\mathbf{q}-\mathbf{k})}{(\mathbf{q}-\mathbf{k})^2}\Big]\delta C^+(\mathbf{k},\Omega)\big[\delta C^+(\mathbf{q}-\mathbf{k},\omega-\Omega) - \delta C^-(\mathbf{q}-\mathbf{k},\omega-\Omega)\big], \\ \\ i\omega\delta C^-(\mathbf{q},\omega) = -Dq^2\delta C^-(\mathbf{q},\omega) - i\mathbf{q}\cdot\boldsymbol{\mathcal{E}}D\delta C^-(\mathbf{q},\omega) - i\mathbf{q}\cdot\boldsymbol{\eta}^-(\mathbf{q},\omega) \\ \qquad\qquad + 4\pi\ell_B D\int \frac{d\Omega}{2\pi}\frac{d^d\mathbf{k}}{(2\pi)^d}\Big[\frac{\mathbf{q}\cdot(\mathbf{q}-\mathbf{k})}{(\mathbf{q}-\mathbf{k})^2}\Big]\delta C^-(\mathbf{k},\Omega)\big[\delta C^+(\mathbf{q}-\mathbf{k},\omega-\Omega) - \delta C^-(\mathbf{q}-\mathbf{k},\omega-\Omega)\big]. \end{cases} \tag{2.9}$$

To derive the current density expression, we formulate explicitly the expressions of the net number density $C(\mathbf{q},\omega)$ and the charge density $\rho(\mathbf{q},\omega)$:

$$\begin{cases} C(\mathbf{q},\omega) = C^+(\mathbf{q},\omega) + C^-(\mathbf{q},\omega) - 2DC_{\text{pore}}(\mathbf{q},\omega) = \delta C^+(\mathbf{q},\omega) + \delta C^-(\mathbf{q},\omega) \\ \rho(\mathbf{q},\omega) = C^+(\mathbf{q},\omega) - C^-(\mathbf{q},\omega) = \delta C^+(\mathbf{q},\omega) - \delta C^-(\mathbf{q},\omega). \end{cases} \tag{2.10}$$

By taking the difference and the sum of the positive and negative ions flux densities defined in Eq. (2.8) we conclude the expression for the current density $\boldsymbol{J}_\rho(q,\omega)$:

$$\begin{aligned}\boldsymbol{J}_\rho(\mathbf{q},\omega) = {} & 2DC_{\text{pore}}\boldsymbol{\mathcal{E}}(2\pi)\delta(\omega)(2\pi)^d\delta^d(\mathbf{q}) + i\mathbf{q}D\rho(\mathbf{q},\omega) + D\boldsymbol{\mathcal{E}}C(\mathbf{q},\omega) + i\kappa^2 D\frac{\mathbf{q}}{q^2}\rho(\mathbf{q},\omega) \\ & - \left[\boldsymbol{\eta}^+(\mathbf{q},\omega) - \boldsymbol{\eta}^-(\mathbf{q},\omega)\right] + i4\pi\ell_B D\int\frac{d\Omega}{2\pi}\frac{d^d\mathbf{k}}{(2\pi)^d}\frac{(\mathbf{q}-\mathbf{k})}{(\mathbf{q}-\mathbf{k})^2}\ C(\mathbf{k},\Omega)\rho(\mathbf{q}-\mathbf{k},\omega-\Omega),\end{aligned} \tag{2.11}$$

and the expression for the particle flux $\boldsymbol{J}_C(q,\omega)$:

$$\begin{aligned}\boldsymbol{J}_C(\mathbf{q},\omega) = {} & i\mathbf{q}DC(\mathbf{q},\omega) + D\boldsymbol{\mathcal{E}}\rho(\mathbf{q},\omega) - \left[\boldsymbol{\eta}^+(\mathbf{q},\omega) + \boldsymbol{\eta}^-(\mathbf{q},\omega)\right] \\ & + i4\pi\ell_B D\int\frac{d\Omega}{2\pi}\frac{d^d\mathbf{k}}{(2\pi)^d}\frac{(\mathbf{q}-\mathbf{k})}{(\mathbf{q}-\mathbf{k})^2}\ \rho(\mathbf{k},\Omega)\rho(\mathbf{q}-\mathbf{k},\omega-\Omega).\end{aligned} \tag{2.12}$$

2.3.3 The Current Density Fluctuations in Fourier Space

As Eq. (2.11) indicates, the Coulomb interactions between the mobile ions result in second order nonlinearities that govern the dynamics of the ionic density fluctuations. For the purpose of our investigation, we focus on the linear theory only, and therefore we ignore the nonlinear terms in what follows.

Discarding non-linear terms and using the following current density correlation function:

$$\left\langle J_\rho(\mathbf{q},\omega)J_\rho(\mathbf{q}',\omega')\right\rangle = (2\pi)^{d+1}\delta(\mathbf{q}+\mathbf{q}')\delta(\omega+\omega')\left\langle\left|J_\rho(\mathbf{q},\omega)\right|^2\right\rangle, \tag{2.13}$$

we proceed to derive the Fourier-transformed current density fluctuations expression: $\left\langle\left|J_\rho(\mathbf{q},\omega)\right|^2\right\rangle = \left\langle\left|\widetilde{J}_\parallel^+(\mathbf{q},\omega) - \widetilde{J}_\parallel^-(\mathbf{q},\omega)\right|^2\right\rangle$, where $\widetilde{...}$ denotes the Fourier transform. For this purpose, we solve first for the two concentrations and insert them in the above expressions to obtain the fluxes.

Rearranging the equations defined in (2.9), and rewriting them in terms of ρ and C, we get:

$$\begin{cases} (i\omega + Dq^2)C(\mathbf{q},\omega) - iD\mathbf{q}\cdot\boldsymbol{\mathcal{E}}\rho(\mathbf{q},\omega) = -i\mathbf{q}\cdot\Big[\boldsymbol{\eta}^{+}(\mathbf{q},\omega) + \boldsymbol{\eta}^{-}(\mathbf{q},\omega)\Big], \\ (i\omega + Dq^2 + \kappa^2 D)\rho(\mathbf{q},\omega) - iD\mathbf{q}\cdot\boldsymbol{\mathcal{E}}C(\mathbf{q},\omega) = -i\mathbf{q}\cdot\Big[\boldsymbol{\eta}^{+}(\mathbf{q},\omega) - \boldsymbol{\eta}^{-}(\mathbf{q},\omega)\Big]. \end{cases} \tag{2.14}$$

Using matrix algebra, we build a matrix system to derive the corresponding expressions for the concentration $C(\mathbf{q},\omega)$ and the density $\rho(\mathbf{q},\omega)$ respectively:

$$\begin{bmatrix} C \\ \rho \end{bmatrix} = \frac{1}{\mathcal{B}} \begin{bmatrix} i\omega + Dq^2 + \kappa^2 D + iD\mathbf{q}\cdot\boldsymbol{\mathcal{E}} & i\omega + Dq^2 + \kappa^2 D - iD\mathbf{q}\cdot\boldsymbol{\mathcal{E}} \\ i\omega + Dq^2 + iD\mathbf{q}\cdot\boldsymbol{\mathcal{E}} & -i\omega - Dq^2 + iD\mathbf{q}\cdot\boldsymbol{\mathcal{E}} \end{bmatrix} \begin{bmatrix} -i\mathbf{q}\cdot\boldsymbol{\eta}^{+}(\mathbf{q},\omega) \\ -i\mathbf{q}\cdot\boldsymbol{\eta}^{-}(\mathbf{q},\omega), \end{bmatrix} \tag{2.15}$$

where $\mathcal{B} = [i\omega + Dq^2][i\omega + D(q^2+\kappa^2)] + D^2(\mathbf{q}\cdot\boldsymbol{\mathcal{E}})^2$.

Using Eq. (2.15) we arrive at the response equations for the concentration $C(\mathbf{q},\omega)$ and the density $\rho(\mathbf{q},\omega)$ using defined functions $G_c^{+}(\mathbf{q},\omega)$, $G_c^{-}(\mathbf{q},\omega)$, $G_\rho^{+}(\mathbf{q},\omega)$, and $G_\rho^{-}(\mathbf{q},\omega)$ in Eq. (2.17):

$$\begin{cases} C(\mathbf{q},\omega) = \big[G_c^{+}(\mathbf{q},\omega) + G_c^{-}(\mathbf{q},\omega)\big]\big[-i\mathbf{q}\boldsymbol{\eta}^{+}(\mathbf{q},\omega)\big] + \big[G_c^{+}(\mathbf{q},\omega) - G_c^{-}(\mathbf{q},\omega)\big]\big[-i\mathbf{q}\cdot\boldsymbol{\eta}^{-}(\mathbf{q},\omega)\big], \\ \rho(\mathbf{q},\omega) = \big[G_\rho^{+}(\mathbf{q},\omega) + G_\rho^{-}(\mathbf{q},\omega)\big]\big[-i\mathbf{q}\boldsymbol{\eta}^{+}(\mathbf{q},\omega)\big] + \big[G_\rho^{+}(\mathbf{q},\omega) - G_\rho^{-}(\mathbf{q},\omega)\big]\big[-i\mathbf{q}\cdot\boldsymbol{\eta}^{-}(\mathbf{q},\omega)\big], \end{cases} \tag{2.16}$$

where for simplicity we use the following expressions:

$$\begin{cases} G_c^{+}(\mathbf{q},\omega) = \dfrac{i\omega + Dq^2 + \kappa^2 D}{[i\omega + Dq^2][i\omega + Dq^2 + \kappa^2 D] + D^2(\boldsymbol{q}\cdot\boldsymbol{\mathcal{E}})^2}, \\ G_c^{-}(\mathbf{q},\omega) = \dfrac{iD\boldsymbol{q}\cdot\boldsymbol{\mathcal{E}}}{[i\omega + Dq^2][i\omega + Dq^2 + \kappa^2 D] + D^2(\boldsymbol{q}\cdot\boldsymbol{\mathcal{E}})^2}, \\ G_\rho^{+}(\mathbf{q},\omega) = \dfrac{iD\boldsymbol{q}\cdot\boldsymbol{\mathcal{E}}}{[i\omega + Dq^2][i\omega + Dq^2 + \kappa^2 D] + D^2(\boldsymbol{q}\cdot\boldsymbol{\mathcal{E}})^2}, \\ G_\rho^{-}(\mathbf{q},\omega) = \dfrac{i\omega + Dq^2}{[i\omega + Dq^2][i\omega + Dq^2 + \kappa^2 D] + D^2(\boldsymbol{q}\cdot\boldsymbol{\mathcal{E}})^2}. \end{cases} \tag{2.17}$$

Inserting Eqs. (2.16) and (2.17) in Eqs. (2.11) and (2.12), we find the expressions for the current flux density (Details in the appendix Section (8.1)).

The applied electric field inside the pore is nonzero only in the parallel direction, where $\boldsymbol{\mathcal{E}}(\mathbf{x},t) = (0,0,\mathcal{E}_{\parallel})$. Interested in the current flow across the ion channel in response to a constant applied electric field, the current density fluctuations expression denoted by $\left\langle \left| \widetilde{J}_{\parallel}^{+}(\mathbf{q},\omega) - \widetilde{J}_{\parallel}^{-}(\mathbf{q},\omega) \right|^2 \right\rangle$ reads:

$$\begin{aligned}
&\left\langle \left| \widetilde{J}_{\parallel}^{+}(\mathbf{q},\omega) - \widetilde{J}_{\parallel}^{-}(\mathbf{q},\omega) \right|^2 \right\rangle = \\
&4DC_{\text{pore}} \Bigg[1 + \frac{\omega^2 \left[D^2 \mathcal{E}_{\parallel}^2 q^2 [2q_{\parallel}^2 + q^2] - \kappa^2 D^2 q_{\parallel}^2 (\kappa^2 + 2q^2) - D^2 q_{\parallel}^2 q^4 \right]}{q^2 \left[(-\omega^2 + D^2 q^4 + D^2 q^2 \kappa^2 + D^2 q_{\parallel}^2 \mathcal{E}_{\parallel}^2)^2 + (2\omega D q^2 + \omega D \kappa^2)^2 \right]} \\
&+ \frac{[q_{\perp}^2 - q_{\parallel}^2][2D^4 \kappa^2 q^4 \mathcal{E}_{\parallel}^2 + D^4 \mathcal{E}_{\parallel}^4 q_{\parallel}^2 q^2 + D^4 \kappa^4 \mathcal{E}_{\parallel}^2 q^2]}{q^2 \left[(-\omega^2 + D^2 q^4 + D^2 q^2 \kappa^2 + D^2 q_{\parallel}^2 \mathcal{E}_{\parallel}^2)^2 + (2\omega D q^2 + \omega D \kappa^2)^2 \right]} \\
&+ \frac{-D^4 \kappa^2 q^4 q_{\parallel}^2 [\kappa^2 + 2q^2] + D^4 q^8 [\mathcal{E}_{\parallel}^2 - q_{\parallel}^2] + D^4 \kappa^4 q_{\parallel}^4 \mathcal{E}_{\parallel}^2 - D^4 q_{\parallel}^2 q^4 \mathcal{E}_{\parallel}^2 [q_{\parallel}^2 + 2q^2]}{q^2 \left[(-\omega^2 + D^2 q^4 + D^2 q^2 \kappa^2 + D^2 q_{\parallel}^2 \mathcal{E}_{\parallel}^2)^2 + (2\omega D q^2 + \omega D \kappa^2)^2 \right]} \Bigg].
\end{aligned} \tag{2.18}$$

2.3.4 Final Expression for the Current Fluctuations

Using Eq. (2.18), we proceed to derive the final expression for the current fluctuations $S(\omega)$. We begin by writing the expression of the current $I(t)$ as the integral of the current density $J_{\parallel}^{+}(\boldsymbol{x},t) - J_{\parallel}^{-}(\boldsymbol{x},t)$ at a given position in the direction of $x_{\parallel}$:

$$I(t) = \frac{1}{L} \iint_A \mathrm{d}x_{\perp 1} \mathrm{d}x_{\perp 2} \int \mathrm{d}x_{\parallel} \left[J_{\parallel}^{+}(\boldsymbol{x},t) - J_{\parallel}^{-}(\boldsymbol{x},t) \right]. \tag{2.19}$$

The two-sided power spectral density $S(\omega)$ of the current $I(t)$ defined on the domain $0 < t < T$ is given by the limit of $T \to \infty$ of

$$S(\omega) = \frac{1}{T} \langle |\tilde{I}(\omega)|^2 \rangle = \frac{1}{T} \langle \tilde{I}_{\parallel}(\omega)\, \tilde{I}(-\omega) \rangle, \tag{2.20}$$

which can be written as

$$S(\omega) = \frac{1}{T}\int_T \mathrm{d}t \int_T \mathrm{d}t'\, e^{-i\omega(t-t')}\,\langle I(t)\, I(t')\rangle. \tag{2.21}$$

Combining Eq. (2.19) and Eq. (2.21), we get an expression for the current power spectral density in terms of the ion fluxes:

$$\begin{aligned} S(\omega) =& \frac{1}{L^2}\frac{1}{T}\int_T \mathrm{d}t \int_T \mathrm{d}t'\, e^{-i\omega(t-t')} \iint_A \mathrm{d}x_{\perp 1}\mathrm{d}x_{\perp 2}\int \mathrm{d}x_{\parallel} \iint_A \mathrm{d}x'_{\perp 1}\mathrm{d}x'_{\perp 2}\int \mathrm{d}x'_{\parallel} \\ & \times \Big\langle \big[J^+_{\parallel}(\boldsymbol{x},t) - J^-_{\parallel}(\boldsymbol{x},t)\big]\big[J^+_{\parallel}(\boldsymbol{x}',t') - J^-_{\parallel}(\boldsymbol{x}',t')\big]\Big\rangle. \end{aligned} \tag{2.22}$$

Taking the Fourier transforms of Eq. (2.22), we arrive at:

$$\begin{aligned} S(\omega) =& \frac{1}{L^2}\frac{1}{T}\int_T \mathrm{d}t \int_T \mathrm{d}t'\, e^{-i\omega(t-t')} \iint_A \mathrm{d}x_{\perp 1}\mathrm{d}x_{\perp 2}\int_L \mathrm{d}x_{\parallel} \iint_A \mathrm{d}x'_{\perp 1}\mathrm{d}x'_{\perp 2}\int_L \mathrm{d}x'_{\parallel} \\ & \times \int \frac{\mathrm{d}q_{\perp 1}}{2\pi}\int \frac{\mathrm{d}q_{\perp 2}}{2\pi}\int \frac{\mathrm{d}q_{\parallel}}{2\pi}\, e^{-i(q_{\perp 1}x_{\perp 1}+q_{\perp 2}x_{\perp 2}+q_{\parallel}x_{\parallel})} \\ & \times \int \frac{\mathrm{d}q'_{\perp 1}}{2\pi}\int \frac{\mathrm{d}q'_{\perp 2}}{2\pi}\int \frac{\mathrm{d}q'_{\parallel}}{2\pi}\, e^{-i(q'_{\perp 1}x'_{\perp 1}+q'_{\perp 2}x'_{\perp 2}+q'_{\parallel}x'_{\parallel})} \\ & \times \int \frac{\mathrm{d}\omega'}{2\pi}\int \frac{\mathrm{d}\omega''}{2\pi}\, e^{-i\omega' t}e^{-i\omega'' t'}\Big\langle \big[J^+_{\parallel}(\mathbf{q},\omega') - J^-_{\parallel}(\mathbf{q},\omega')\big]\big[J^+_{\parallel}(\mathbf{q}',\omega'') - J^-_{\parallel}(\mathbf{q}',\omega'')\big]\Big\rangle. \end{aligned} \tag{2.23}$$

Evaluating the integrals over ω'', $\mathbf{q}'$, and using Eq. (2.13) we get:

$$\begin{aligned} S(\omega) =& \frac{1}{L^2}\frac{1}{T}\int_T \mathrm{d}t \int_T \mathrm{d}t'\, e^{-i\omega(t-t')} \iint_A \mathrm{d}x_{\perp 1}\mathrm{d}x_{\perp 2}\int_L \mathrm{d}x_{\parallel} \iint_A \mathrm{d}x'_{\perp 1}\mathrm{d}x'_{\perp 2}\int_L \mathrm{d}x'_{\parallel} \\ & \times \int \frac{\mathrm{d}q_{\perp 1}}{2\pi}\int \frac{\mathrm{d}q_{\perp 2}}{2\pi}\int \frac{\mathrm{d}q_{\parallel}}{2\pi}\, e^{-i(q_{\parallel}(x_{\parallel}-x'_{\parallel})+q_{\perp 1}(x_{\perp 1}-x'_{\perp 1})+q_{\perp 2}(x_{\perp 2}-x'_{\perp 2}))} \\ & \times \int \frac{\mathrm{d}\omega'}{2\pi}\, e^{i\omega'(t-t')}\langle |\big[\tilde{J}^+(\mathbf{q},\omega') - \tilde{J}^-(\mathbf{q},\omega')\big]|^2\rangle. \end{aligned} \tag{2.24}$$

If we perform the integrals over t, t' and ω', and we rearrange the expression we finally arrive to:

$$S(\omega) = \frac{1}{2\pi^2}\int_{\pi L^{-1}}^{\pi\Lambda^{-1}} \mathrm{d}q_{\parallel} \int_{\pi R^{-1}}^{\pi\Lambda^{-1}} q_{\perp}\mathrm{d}q_{\perp}\, \big|\widetilde{\mathcal{A}}(q_{\perp})\big|^2\big|\widetilde{\mathcal{L}}(q_{\parallel})\big|^2\langle |\big[\tilde{J}^+(\mathbf{q},\omega) - \tilde{J}^-(\mathbf{q},\omega)\big]|^2\rangle. \tag{2.25}$$

The limits of integration over the wave-vectors depend on the geometric factors: R, L, and the cut-off length Λ (see figure 2.2).

The average squared Fourier-transformed functions $\left|\widetilde{\mathcal{A}}(q_\perp)\right|^2$ and $\left|\widetilde{\mathcal{L}}(q_\parallel)\right|^2$ being given respectively by the following integrals:

$$\left|\widetilde{\mathcal{A}}(q_{\perp 1}, q_{\perp 2})\right|^2 = \iint_A \mathrm{d}x_{\perp 1}\mathrm{d}x_{\perp 2} \iint_A \mathrm{d}x'_{\perp 1}\mathrm{d}x'_{\perp 2}\, e^{-i(q_{\perp 1}(x_{\perp 1}-x'_{\perp 1})+q_{\perp 2}(x_{\perp 2}-x'_{\perp 2}))}, \tag{2.26}$$

representing the area function and

$$\left|\widetilde{\mathcal{L}}(q_\parallel)\right|^2 = \frac{1}{L^2}\int_L \mathrm{d}x_\parallel \int_L \mathrm{d}x'_\parallel\, e^{-i(q_\parallel(x_\parallel - x'_\parallel))}, \tag{2.27}$$

representing the length function.

2.3.5 Area and Length Functions

The integral in Eq. (2.26) is performed over the lateral area A of the pore built using Bead particles. As Fig. 2.3 shows, the cross sectional area can be approximated by two different geometries: square or circle.

Square approximation: First, if we integrate over a square of sides $2R$ we get:

$$\left|\widetilde{\mathcal{A}}(q_{\perp 1}, q_{\perp 2})\right|^2 = \left(\frac{4\sin\left[q_{\perp 1}R\right]\sin\left[q_{\perp 2}R\right]}{q_{\perp 1}q_{\perp 2}}\right)^2, \tag{2.28}$$

with $q_{\perp_1}$ and $q_{\perp_2}$ being the coordinates in reciprocal space.

Circular approximation: Integrating over a circle of radius R gives

$$\begin{cases} \widetilde{\mathcal{A}} = \displaystyle\int_0^{2\pi}\mathrm{d}\theta \int_0^R \mathrm{d}x_\perp\, x_\perp\, e^{-iq_\perp x_\perp \cos(\phi-\theta)} \\ \left|\widetilde{\mathcal{A}}(q_{\perp 1}, q_{\perp 2})\right|^2 = 2\pi R^2\ \frac{J_1[q_\perp R]}{q_\perp R}, \end{cases} \tag{2.29}$$

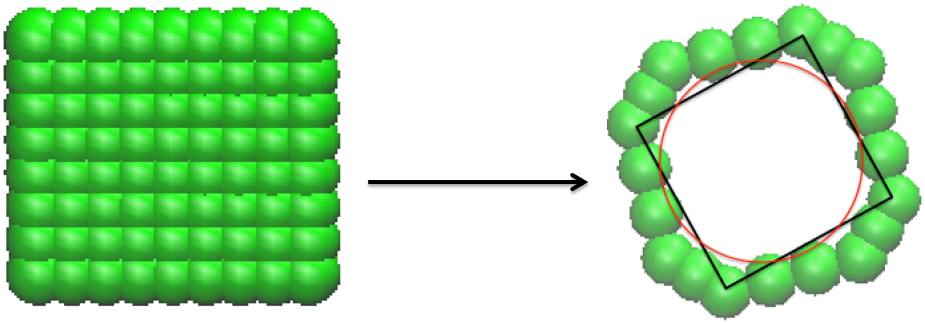

Figure 2.3: An example of how particles will be used to build the pore. We start from a square layer of particles (figure on the left) and we take out all particles falling within a certain radius R (figure on the right). The particles will then be distributed to form an approximately circular cross section. From the figure, we can see that the area can be treated as rectangular or circular.

with $x_\perp = \sqrt{x_{\perp 1}^2 + x_{\perp 2}^2}$ and $\theta = \arctan(x_{\perp 2}/x_{\perp 1})$ being the cylindrical coordinates, $q_\perp = \sqrt{q_{\perp 1}^2 + q_{\perp 2}^2}$ and $\phi = \arctan(q_{\perp 2}/q_{\perp 1})$ being the polar coordinates in reciprocal space, and J_1 being the first order Bessel function of the first kind.

Both the square and the circular integrations represent approximations of our geometry in real space, whose accuracy depends on R. Larger radius leads to better approximations and smoother geometry. The radius R that we use in our calculations is evaluated by counting the number of membrane particles precluded from a complete squared layer of particles as shown in Fig. 2.4. Subsequently, the area is calculated by multiplying the concluded number with the squared lattice constant. For the square integration, we employ $R = \sqrt{A/4}$, whereas for the circular integration we employ $R = \sqrt{A/\pi}$.

However, contrary to the circular area function, the square area can be mapped directly to reciprocal space. Therefore, we use Eq. (2.28) for all the curves in the thesis. Regarding the expression for $\left|\widetilde{\mathcal{L}}(q_\parallel)\right|^2$ in Eq. (2.27), we integrate over the length of the pore:

$$\left|\widetilde{\mathcal{L}}(q_\parallel)\right|^2 = \frac{1}{L^2}\int_0^L \int_0^L dx_\parallel dx'_\parallel \; e^{iq_\parallel x_\parallel}\, e^{iq_\parallel x'_\parallel} = \frac{2}{(Lq_\parallel)^2}\left[1 - \cos(Lq_\parallel)\right]. \tag{2.30}$$

Combining Eqs. (2.18), (2.25), (2.28), and (2.30), we reach the final expression for the current fluctuations $S(\omega)$.

As the expression of $S(\omega)$ (Eq. (2.25)) indicates, the behaviour of the current fluctuations will be governed by a plateau at low frequencies that will be followed by a power law decay at higher frequencies as shown in Fig. 2.4.

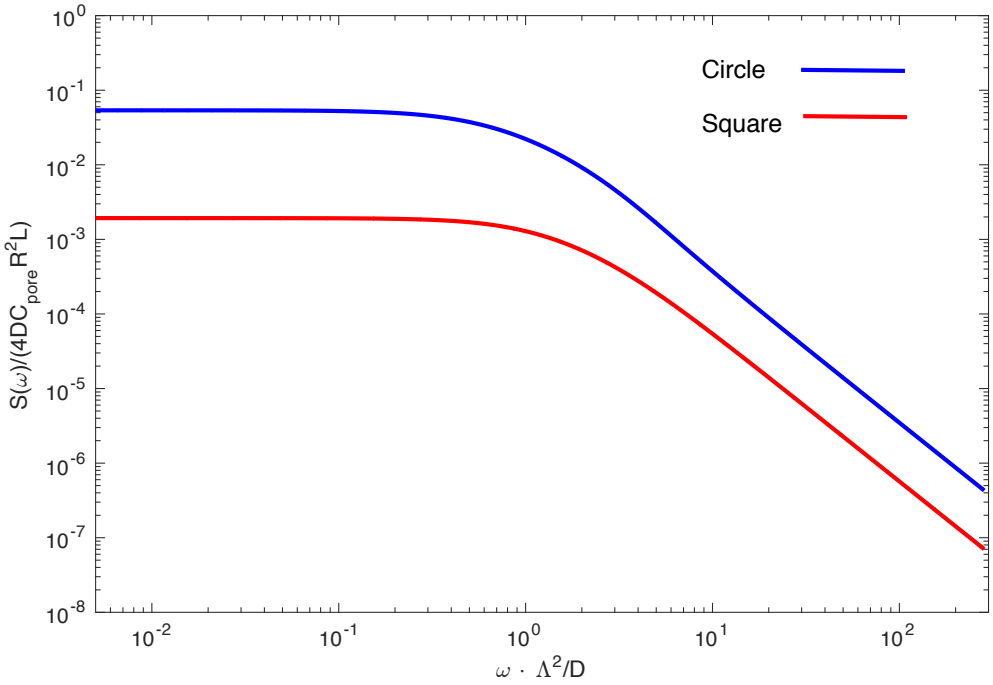

Figure 2.4: The current fluctuations $S(\omega)$ calculated according to the linearized mean-field theory using two different approximations for the area function (Eq. (2.28) and Eq. (2.29)) on a logarithmic scale. The circle and the square both have the same lateral area, equal to the surface area of the particles removed from the membrane to form the pore.

2.3.6 Mean Current

To get an expression for the mean current in our system, we start with the zero frequency component of Eq. (2.11) that takes the following form:

$$J_\rho = 2DC_{\text{pore}}\boldsymbol{\mathcal{E}}(2\pi)\delta(\omega)(2\pi)^d\delta^d(\mathbf{q}), \tag{2.31}$$

with $d = 3$. By taking the integral of the current density in Eq. (2.31) over the differential area, and averaging over the height, we obtain an expression for the average current:

$$I = \frac{1}{L}\int dx_\parallel \int_A dx_{\perp_1} dx_{\perp_2} \left[J_\parallel^+(\boldsymbol{x},t) - J_\parallel^-(\boldsymbol{x},t)\right]. \tag{2.32}$$

In Fourier space the average current in Eq. (2.32) reads:

$$\begin{aligned} I = \frac{1}{L}\int\int_A dx_{\perp 1}dx_{\perp 2}\int dx_{\parallel}\int\frac{dq_{\perp 1}}{2\pi}\int\frac{dq_{\perp 2}}{2\pi}\int\frac{dq_{\parallel}}{2\pi} \\ \times e^{-i(q_{\parallel}x_{\parallel}+q_{\perp 1}x_{\perp 1}+q_{\perp 2}x_{\perp 2})}\int\frac{d\omega}{2\pi}e^{i\omega t}\left[J_{\parallel}^{+}(\mathbf{q},\omega)-J_{\parallel}^{-}(\mathbf{q},\omega)\right]. \end{aligned} \tag{2.33}$$

If we replace $J_{\parallel}^{+}(\mathbf{q},\omega)-J_{\parallel}^{-}(\mathbf{q},\omega)$ by its corresponding expression Eq. (2.31), we get:

$$\begin{aligned} I = \int\int_A dx_{\perp 1}dx_{\perp 2}\int\frac{dq_{\perp 1}}{2\pi}\int\frac{dq_{\perp 2}}{2\pi}\int\frac{dq_{\parallel}}{2\pi} \\ \times e^{-i(q_{\perp 1}x_{\perp 1}+q_{\perp 2}x_{\perp 2})}\int\frac{d\omega}{2\pi}e^{i\omega t}2DC_{\text{pore}}(2\pi)^4\mathcal{E}_{\parallel}\delta(\omega)\delta(q_{\parallel})\delta(q_{\perp 1})\delta(q_{\perp 2}). \end{aligned} \tag{2.34}$$

Performing the integrations in Eq. (2.34), we obtain the final expression of the mean current:

$$I = 2\pi R^2 DC_{\text{pore}}\mathcal{E}_{\parallel}. \tag{2.35}$$

Equation (2.35) highlights the linear behaviour of the mean current I as a function of the applied electric field $\mathcal{E}_{\parallel}$, a feature that is illustrated explicitly in Fig. 3.2 in the following chapter.

2.3.7 Examining the Different Asymptotic Forms

The current fluctuations expression as shown in Fig. 2.4 describes a plateau at low frequencies followed by a power law and a discarded white noise at very high frequencies described by $4DC_{\text{pore}}$.

From the expression of the flux density fluctuations given in equation (2.18), we observe that current fluctuations will depend—through competing contributions—on the electric field, the geometric features of the pore, and the Debye length. To develop a physical intuition about the behaviour of $S(\omega)$ at different frequencies as a function of all these parameters, we examine the different asymptotic limits of equation (2.18).

As it was mentioned and developed, the power spectral density at very high frequencies is governed by white noise:

$$\lim_{\omega\to\infty}\left\langle\left|\widetilde{J}_{\parallel}^{+}(\mathbf{q},\omega)-\widetilde{J}_{\parallel}^{-}(\mathbf{q},\omega)\right|^{2}\right\rangle = 4DC_{\text{pore}}. \tag{2.36}$$

At low frequencies, the polynomial expressions of the ratio are of the same order, however at this asymptotic limit the current density fluctuations expression Eq. (2.18) takes the following complicated form:

$$\begin{aligned}&\left\langle\left|\widetilde{J}_{\parallel}^{+}(\mathbf{q},0)-\widetilde{J}_{\parallel}^{-}(\mathbf{q},0)\right|^{2}\right\rangle = \\ &4DC_{\text{pore}}q_{\perp}^{2}\left[\frac{\mathcal{E}_{\parallel}^{4}q_{\parallel}^{2}(q_{\perp}^{2}+q_{\parallel}^{2})+\mathcal{E}_{\parallel}^{2}(q_{\parallel}^{2}+q_{\perp}^{2}+\kappa^{2})\left[\kappa^{2}q_{\perp}^{2}+(q_{\parallel}^{2}+q_{\perp}^{2})(2q_{\parallel}^{2}+q_{\perp}^{2})\right]}{q^{2}\left[(q^{4}+q^{2}\kappa^{2}+2q_{\parallel}^{2}\mathcal{E}_{\parallel}^{2})^{2}\right]}\right. \\ &\left.+\frac{(q_{\parallel}^{2}+q_{\perp}^{2})^{2}(q_{\parallel}^{2}+q_{\perp}^{2}+\kappa^{2})^{2}}{q^{2}\left[(q^{4}+q^{2}\kappa^{2}+2q_{\parallel}^{2}\mathcal{E}_{\parallel}^{2})^{2}\right]}\right],\end{aligned} \tag{2.37}$$

where q^2 was replaced by $q_{\perp}^{2}+q_{\parallel}^{2}$. The behaviour of Eq. (2.37) depends on the applied electric field $\mathcal{E}_{\parallel}$, the inverse Debye length κ, and the pore dimensions. To explore these dependencies, we study the limiting behaviours of each of these variables.

As $\kappa \to 0$, equation (2.37) reduces to an equation that depends on the applied electric field and the pore dimensions:

$$\lim_{\kappa\to 0}\left\langle\left|\widetilde{J}_{\parallel}^{+}(\mathbf{q},0)-\widetilde{J}_{\parallel}^{-}(\mathbf{q},0)\right|^{2}\right\rangle = 4DC_{\text{pore}}\frac{q_{\perp}^{2}(q_{\parallel}^{2}+q_{\perp}^{2}+\mathcal{E}_{\parallel}^{2})}{\left[(q_{\parallel}^{2}+q_{\perp}^{2})^{2}+q_{\parallel}^{2}\mathcal{E}_{\parallel}^{2}\right]}. \tag{2.38}$$

Equation (2.38), indicates that at high values of the electric field, the magnitude of $S(\omega)$ at low frequencies will be controlled by $(q_{\perp}/q_{\parallel})^2$, which depends on the aspect ratio of the pore. However, at lower values of the electric field, a smaller amplitude of the noise is perceived, which becomes less significant when the length L of the channel approaches its radius R as shown in Fig. 2.5.

At higher values of κ, a different behaviour is perceived at which the current density fluctua-

tions expression reads:

$$\lim_{\kappa\to\infty}\left\langle\left|\widetilde{J}_{\parallel}^{+}(\mathbf{q},0)-\widetilde{J}_{\parallel}^{-}(\mathbf{q},0)\right|^{2}\right\rangle=4DC_{\text{pore}}\Big(\frac{q_{\perp}^{2}}{q_{\parallel}^{2}+q_{\perp}^{2}}\Big)\Big[1+\frac{\mathcal{E}_{\parallel}^{2}q_{\perp}^{2}}{(q_{\parallel}^{2}+q_{\perp}^{2})^{2}}\Big]. \tag{2.39}$$

At low values of the electric field, $S(\omega)$ features a plateau that decreases in amplitude when using shorter pores, whereas at high electric field, a continuously increasing behaviour is observed as indicated in Fig. 2.5(b).

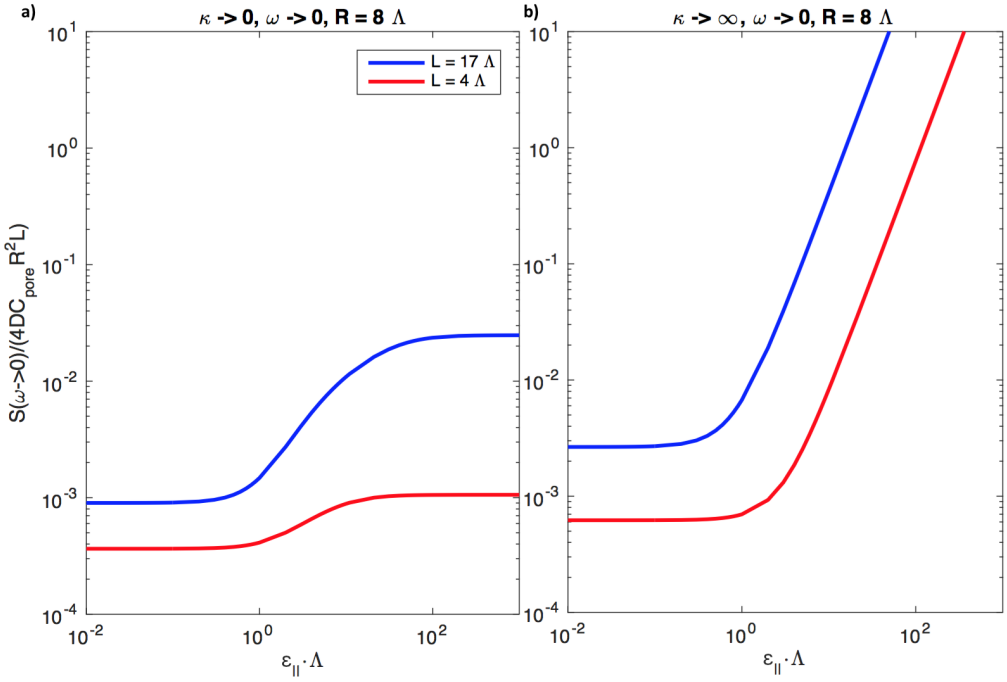

Figure 2.5: (a) The current fluctuations as ω tends to 0 as a function of the applied electric field, with κ approaching 0. (b) The current fluctuations as ω tends to 0 as a function of the applied electric field, with κ approaching infinity.

From another perspective, at sufficiently high and low electric field, all terms involving κ in Eq. (2.37) cancel and we get the same behaviour we found previously from Eq. (2.38) namely :

$$\lim_{\mathcal{E}_{\parallel}\to 0}\left\langle\left|\widetilde{J}_{\parallel}^{+}(\mathbf{q},0)-\widetilde{J}_{\parallel}^{-}(\mathbf{q},0)\right|^{2}\right\rangle=4DC_{\text{pore}}\frac{q_{\perp}^{2}}{(q_{\parallel}^{2}+q_{\perp}^{2})}, \tag{2.40a}$$

$$\lim_{\mathcal{E}_{\parallel}\to\infty}\left\langle\left|\widetilde{J}_{\parallel}^{+}(\mathbf{q},0)-\widetilde{J}_{\parallel}^{-}(\mathbf{q},0)\right|^{2}\right\rangle=4DC_{\text{pore}}\frac{q_{\perp}^{2}}{q_{\parallel}^{2}}. \tag{2.40b}$$

In summary, at low frequencies the current fluctuations expression will be characterised by a higher amplitude at higher electric field, a behaviour that becomes more significant when considering higher values of κ.

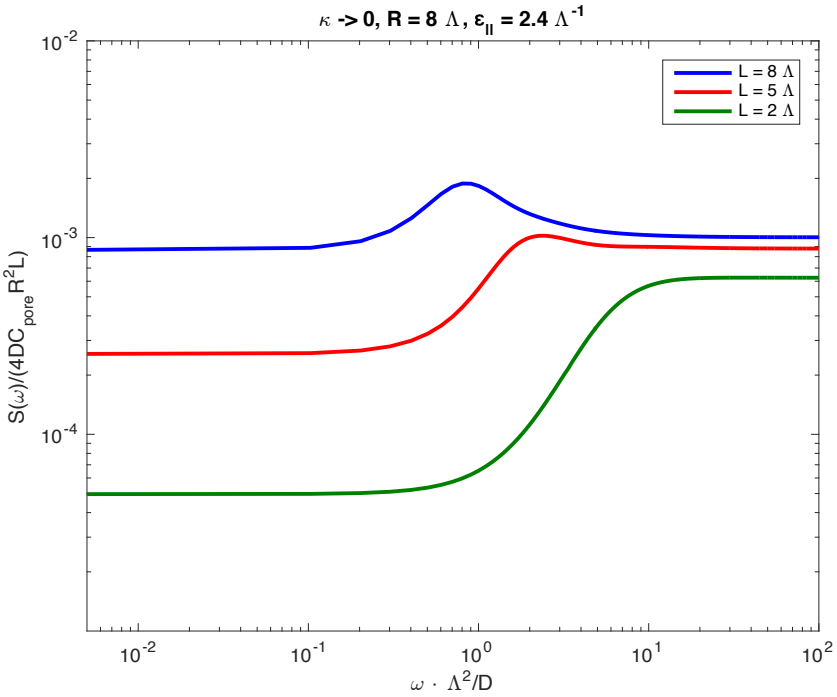

Figure 2.6: The current fluctuations as κ tends to 0 as a function of the frequency ω, using pores with radius $R = 8\ \Lambda$ and lengths $L = 1.5,\ 4,\ 8\ \Lambda$.

To get a deeper understanding of the behaviour of the current fluctuations expression at a certain frequency or over a range of frequencies, we consider the behaviour of $S(\omega)$ at low and high values of the inverse Debye length κ as a function of the frequency ω:

$$\lim_{\kappa\to 0}\left\langle\left|\widetilde{J}_{\parallel}^{+}(\mathbf{q},\omega)-\widetilde{J}_{\parallel}^{-}(\mathbf{q},\omega)\right|^{2}\right\rangle = 4DC_{\text{pore}}\frac{\left[\omega^2+D^2\mathcal{E}_{\parallel}^2q_{\parallel}^2+D^2(q_{\parallel}^2+q_{\perp}^2)^2\right]\left[\omega^2+D^2q_{\perp}^2(q_{\parallel}^2+q_{\perp}^2+\mathcal{E}_{\parallel}^2)\right]}{\omega^4+2D^2\omega^2\left[(q_{\parallel}^2+q_{\perp}^2)^2-\mathcal{E}_{\parallel}^2q_{\parallel}^2\right]+D^4\left[(q_{\parallel}^2+q_{\perp}^2)^2+q_{\parallel}^2\mathcal{E}_{\parallel}^2\right]^2}. \tag{2.41}$$

Under the pore condition that we consider, $S(\omega)$ will show a plateau at low frequencies and a decreasing power law at high frequencies followed by the white noise. Nonetheless, at this limit, an interesting behaviour is observed if we consider a pore with a radius considerably larger than its length. Under this condition, the shape of the function reverts, showing a

weaker plateau at small frequencies followed by an increasing power law as shown Fig. 2.6 above.

In limit where κ approaches infinity, equation (2.18) yields:

$$\lim_{\kappa\to\infty}\left\langle\left|\widetilde{J}_{\parallel}^{+}(\mathbf{q},\omega)-\widetilde{J}_{\parallel}^{-}(\mathbf{q},\omega)\right|^{2}\right\rangle=4DC_{\text{pore}}\frac{q_{\perp}^{2}}{q_{\parallel}^{2}+q_{\perp}^{2}}\frac{\omega^{2}+D^{2}\mathcal{E}_{\parallel}^{2}q_{\perp}^{2}+D^{2}(q_{\parallel}^{2}+q_{\perp}^{2})^{2}}{\omega^{2}+D^{2}(q_{\parallel}^{2}+q_{\perp}^{2})^{2}}. \quad (2.42)$$

At this limit, $S(\omega)$ does not exhibit any peculiar behaviour, except when dealing with a very short pore as shown below in Fig. 2.7. At this condition, $S(\omega)$ is almost flat as the difference between the low frequency plateau and the high frequency white noise becomes negligible.

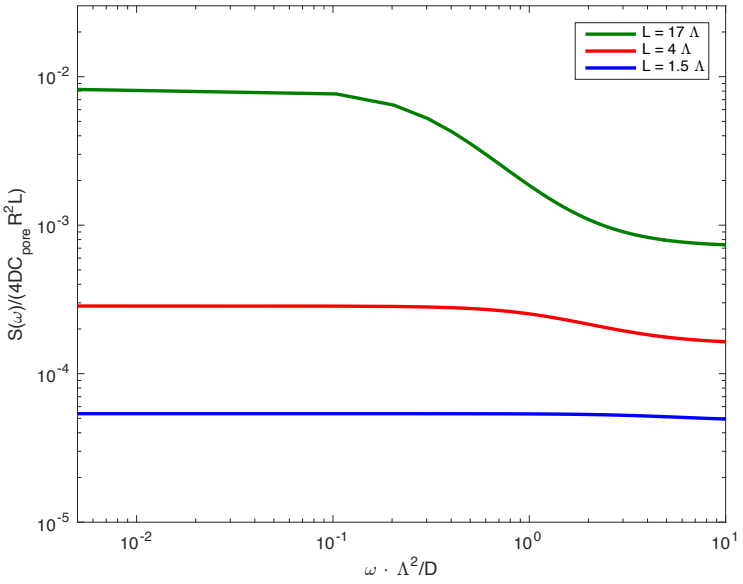

Figure 2.7: The current fluctuations behaviour as κ tends to infinity as a function of the frequency ω in a pore with radius $R = 8\ \Lambda$ and length $L = 1.5\ \Lambda$, $L = 4\ \Lambda$, and $L = 17\ \Lambda$. The applied electric field $\mathcal{E}_{\parallel}$ is set to 2.4 Λ^{-1}.

To elaborate more on the behaviour of the current fluctuations, we plot the variation of the current fluctuations at a certain specified low frequency, e.g. $\omega = 0.01\ \Lambda^2/D$, as a function of the applied electric field as shown in Fig. 2.8. We find that the power spectrum will always exhibit a higher amplitude at high values of the electric field, a result that becomes more significant when dealing with longer pores.

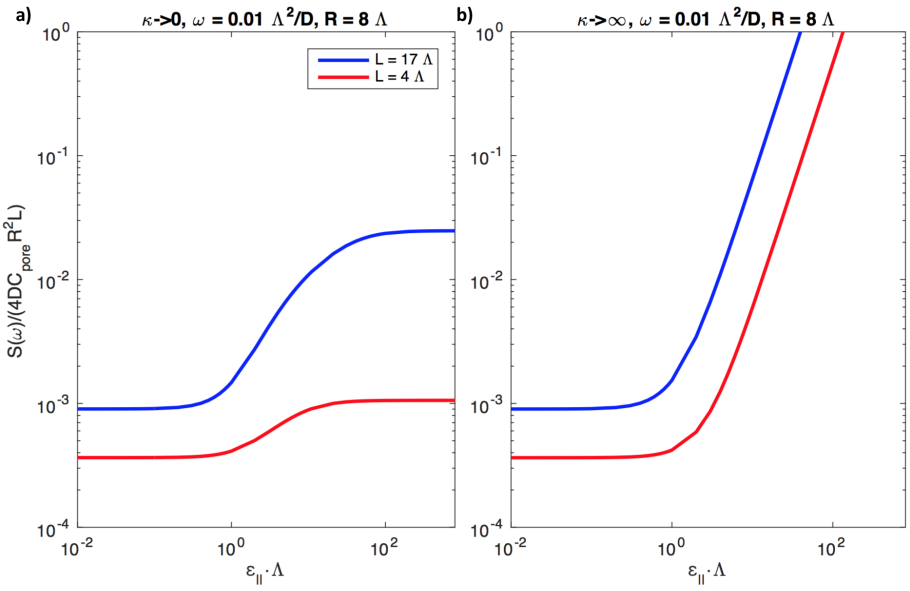

Figure 2.8: (a) The current fluctuations as κ tends to 0 as a function of the applied electric field, at a fixed frequency $\omega = 0.01\ \Lambda^2/D$. (b) The current fluctuations as κ tends to infinity as a function of the applied electric field, at a fixed frequency $\omega = 0.01\ \Lambda^2/D$.

The behaviour of Eq. (2.42) at different values of the electric field remains to be explored. As Fig. 2.9 indicates, the current power spectral density becomes frequency independent as we decrease the magnitude of the applied electric field. This highlights the major role played by the electric field in generating the power law at high frequencies.

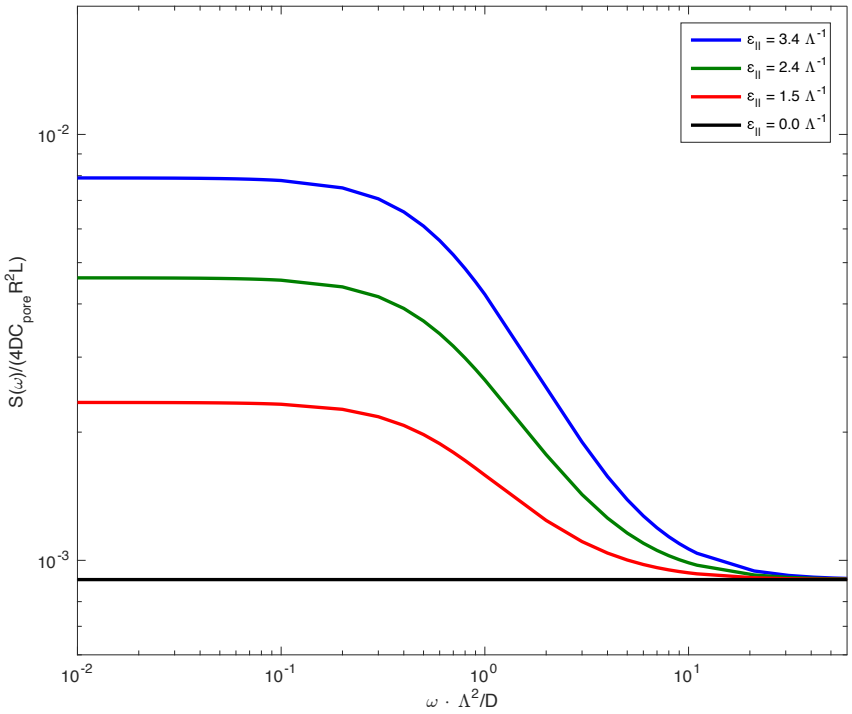

Figure 2.9: The current fluctuations behaviour as κ tends to ∞ as a function of the frequency ω in a pore with radius $R = 8\ \Lambda$ and length $L = 17\ \Lambda$. Four different values of the electric field are used $\mathcal{E}_{\|} = 0.0,\ 1.5,\ 2.4,\ 3.4\ \Lambda^{-1}$.

Finally, we study the low electric field limit. Under this condition, the expression of the current density fluctuations reduces to:

$$\lim_{\mathcal{E}_{\|}\to 0} \left\langle \left| \widetilde{J}_{\|}^{+}(\mathbf{q},\omega) - \widetilde{J}_{\|}^{-}(\mathbf{q},\omega) \right|^2 \right\rangle = 4DC_{\text{pore}} \frac{\omega^2 q_{\|}^2 + q_{\perp}^2\left[\omega^2 + D^2(\kappa^2 + q_{\|}^2 + q_{\perp}^2)^2\right]}{(q_{\perp}^2 + q_{\|}^2)\left[\omega^2 + D^2(\kappa^2 + q_{\|}^2 + q_{\perp}^2)^2\right]}. \quad (2.43)$$

The limit at low frequencies was developed previously in Eq. (2.40 a), highlighting the existence of a discrepancy only when dealing with very long pores. Otherwise, at this limit $S(\omega)$ will be governed by white noise. However, at this limit, the role of the Debye length becomes negligible highlighting once more the major role played by the electric field in generating the frequency dependent behaviour.

2.4 Number and Charge Fluctuations

To better understand the current flow of ions through an ionic channel, we can approach the number and charge fluctuations.

2.4.1 Number Density Fluctuations

By defining the total ion concentration as the sum of the positive and negative ions' fluctuations $C(\mathbf{q},\omega) = \delta C^+ + \delta C^-$, we proceed to derive an expression for the number density fluctuations. We define the linearized form of $C(\mathbf{q},\omega)$ using the previously defined functions $G_c^+(\mathbf{q},\omega)$ and $G_c^-(\mathbf{q},\omega)$ (Eq. (2.17)), hence the total number density in Fourier space can be written as:

$$C(\mathbf{q},\omega) = [G_c^+(\mathbf{q},\omega)+G_c^-(\mathbf{q},\omega)][-i\mathbf{q}\cdot\boldsymbol{\eta}^+(\mathbf{q},\omega)]+[G_c^+(\mathbf{q},\omega)-G_c^-(\mathbf{q},\omega)][-i\mathbf{q}\cdot\boldsymbol{\eta}^-(\mathbf{q},\omega)]. \quad (2.44)$$

Using explicit forms for the functions $G_c^+(\mathbf{q},\omega)$ and $G_c^-(\mathbf{q},\omega)$, we arrive at the final expression for the number density fluctuations:

$$\begin{aligned} &\langle|\left[\tilde{C}^+(\mathbf{q},\omega)+\tilde{C}^-(\mathbf{q},\omega)\right]|^2\rangle \\ &= \frac{4DC_{\text{pore}}q^2\left[D^2(q^2+\kappa^2)^2+\omega^2+D^2q_\parallel^2\mathcal{E}_\parallel^2\right]}{(-\omega^2+D^2q^4+D^2q^2\kappa^2+D^2q_\parallel^2\mathcal{E}_\parallel^2)^2+(2\omega Dq^2+\omega D\kappa^2)^2}. \end{aligned} \quad (2.45)$$

To calculate the power spectrum of the number and charge densities fluctuations, we start by defining the density of ions by the following integrals:

$$\begin{cases} N^+(t) = \int_A dx_{\perp 1}dx_{\perp 2}\int_L dx_\parallel C^+(x_\parallel,x_{\perp 1},x_{\perp 2},t), \\ N^-(t) = \int_A dx_{\perp 1}dx_{\perp 2}\int_L dx_\parallel C^-(x_\parallel,x_{\perp 1},x_{\perp 2},t). \end{cases} \quad (2.46)$$

Using Eq. (2.45) and Eqs. (2.46), the number fluctuations expression $S_N(\omega)$ takes the following form:

$$\begin{aligned}\left|\delta N(\omega)\right|^2 =& \frac{1}{T}\int_T \mathrm{d}t \int_T \mathrm{d}t'\, e^{-i\omega(t-t')} \\ & \Bigg\langle \Big\{ \big[N^+(t)+N^-(t)\big] - \Big\langle \big[N^+(t)+N^-(t)\big] \Big\rangle \Big\} \\ & \times \Big\{ \big[N^+(t')+N^-(t')\big] - \Big\langle \big[N^+(t')+N^-(t')\big] \Big\rangle \Big\} \Bigg\rangle \\ =& \frac{1}{T}\int_T \mathrm{d}t \int_T \mathrm{d}t'\, e^{-i\omega(t-t')} \iint_A \mathrm{d}x_{\perp 1}\mathrm{d}x_{\perp 2} \int \mathrm{d}x_{\parallel} \iint_A \mathrm{d}x'_{\perp 1}\mathrm{d}x'_{\perp 2} \int \mathrm{d}x'_{\parallel} \\ & \Big\langle \big[C^+(\boldsymbol{x},t)+C^-(\boldsymbol{x},t)\big]\big[C^+(\boldsymbol{x}',t')+C^-(\boldsymbol{x}',t')\big] \Big\rangle.\end{aligned} \tag{2.47}$$

Following the same adopted analogy to derive Eq. (2.22), we arrive at the final expression for the number fluctuations:

$$S_N(\omega) = \frac{L^2}{2\pi^2} \int_{\pi L^{-1}}^{\pi \Lambda^{-1}} \mathrm{d}q_{\parallel} \int_{\pi R^{-1}}^{\pi \Lambda^{-1}} q_{\perp}\mathrm{d}q_{\perp} \left|\widetilde{\mathcal{A}}(q_{\perp})\right|^2 \left|\widetilde{\mathcal{L}}(q_{\parallel})\right|^2 \langle \left|\big[\tilde{C}^+(\mathbf{q},\omega)+\tilde{C}^-(\mathbf{q},\omega)\big]\right|^2 \rangle, \tag{2.48}$$

where $\left|\widetilde{\mathcal{A}}(q_{\perp})\right|^2$ and $\left|\widetilde{\mathcal{L}}(q_{\parallel})\right|^2$, are respectively the area and the length functions.

2.4.2 Charge Density Fluctuations

A similar methodology is followed to derive an expression describing the charge density fluctuations $\rho(\mathbf{q},\omega) = \delta C^+ - \delta C^-$. The notation of the linearized form of $\rho(\mathbf{q},\omega)$ in terms of the previously defined functions $G_c^+(\mathbf{q},\omega)$ and $G_c^-(\mathbf{q},\omega)$ (Eq. (2.17)) reads:

$$\rho(\mathbf{q},\omega) = [G_\rho^+(\mathbf{q},\omega)+G_\rho^-(\mathbf{q},\omega)][-i\mathbf{q}\cdot\boldsymbol{\eta}^+(\mathbf{q},\omega)]+[G_\rho^+(\mathbf{q},\omega)-G_\rho^-(\mathbf{q},\omega)][-i\mathbf{q}\cdot\boldsymbol{\eta}^-(\mathbf{q},\omega)]. \tag{2.49}$$

If we replace $G_\rho^+(\mathbf{q},\omega)$ and $G_\rho^-(\mathbf{q},\omega)$ by their corresponding definitions, we arrive at the final expression for the charge density fluctuations:

$$\begin{aligned}&\langle|\left[\tilde{C}^+(\mathbf{q},\omega)-\tilde{C}^-(\mathbf{q},\omega)\right]|^2\rangle\\&=\frac{4DC_{\text{pore}}q^2\left[D^2q^4+D^2q_\parallel^2\mathcal{E}_\parallel^2+\omega^2\right]}{(-\omega^2+D^2q^4+D^2q^2\kappa^2+D^2q_\parallel^2\mathcal{E}_\parallel^2)^2+(2\omega Dq^2+\omega D\kappa^2)^2}.\end{aligned}\tag{2.50}$$

To obtain a representation for the charge density $S_Q(\omega)$ like that in Eq. (2.47), we use Eqs. (2.46):

$$\begin{aligned}\left|\delta Q(\omega)\right|^2=&\frac{1}{T}\int_T\mathrm{d}t\int_T\mathrm{d}t'\,e^{-i\omega(t-t')}\\&\left\langle\left\{\left[N^+(t)-N^-(t)\right]-\left\langle\left[N^+(t)-N^-(t)\right]\right\rangle\right\}\right.\\&\left.\times\left\{\left[N^+(t')-N^-(t')\right]-\left\langle\left[N^+(t')-N^-(t')\right]\right\rangle\right\}\right\rangle\\=&\frac{1}{T}\int_T\mathrm{d}t\int_T\mathrm{d}t'\,e^{-i\omega(t-t')}\iint_A\mathrm{d}x_{\perp1}\mathrm{d}x_{\perp2}\int\mathrm{d}x_\parallel\iint_A\mathrm{d}x'_{\perp1}\mathrm{d}x'_{\perp2}\int\mathrm{d}x'_\parallel\\&\left\langle\left[C^+(\boldsymbol{x},t)-C^-(\boldsymbol{x},t)\right]\left[C^+(\boldsymbol{x}',t')-C^-(\boldsymbol{x}',t')\right]\right\rangle.\end{aligned}\tag{2.51}$$

Using Eq. (2.50), the expression for the charge fluctuations $S_Q(\omega)$ in Eq. (2.51) becomes:

$$S_Q(\omega)=\frac{L^2}{2\pi^2}\int_{\pi L^{-1}}^{\pi\Lambda^{-1}}\mathrm{d}q_\parallel\int_{\pi R^{-1}}^{\pi\Lambda^{-1}}q_\perp\mathrm{d}q_\perp\left|\widetilde{\mathcal{A}}(q_\perp)\right|^2\left|\widetilde{\mathcal{L}}(q_\parallel)\right|^2\langle|\left[\tilde{C}^+(\mathbf{q},\omega)-\tilde{C}^-(\mathbf{q},\omega)\right]|^2\rangle,\tag{2.52}$$

where $\left|\widetilde{\mathcal{A}}(q_\perp)\right|^2$ and $\left|\widetilde{\mathcal{L}}(q_\parallel)\right|^2$ represent the area and the length functions respectively derived in Eqs. (2.27), (2.29), and (2.30). Details about the calculations developed in this chapter are included in the appendix (Sections (8.1) and (8.2)).

2.5 Conclusion

In this chapter, we have developed an exact expression for the current fluctuations $S(\omega)$ without considering the Coulomb interaction potential $V_{ion-ion}(r_{ij})=0$.

The developed linearized mean-field theory expression for $S(\omega)$ predicts a plateau at low frequencies, and therefore is independent of the frequency ω in the limit $\omega \to 0$, in clear contradiction to the low-frequency $S(\omega \to 0) \propto 1/\omega^{\alpha}$ behaviour observed experimentally. It is interesting to note that the same calculation in one dimension leads to $S(\omega \to 0) \propto 1/\omega^2$, which is incompatible not only with experimental results, but also with effectively one-dimensional simulations performed by Fulinski et al.[134].

At vanishing electric field $\mathcal{E}_{\|}$, the spectrum almost disappears and is governed by statistical fluctuations. In later chapters, the validity of our theory will be explored by comparing it to extensive simulations results in which all experimental assumptions will be examined. Besides, we have derived expressions for the number and charge power spectral density that constitute the core of our future work.

CHAPTER 3

Langevin Dynamics Simulation

All truths are easy to understand once they are discovered; the point is to discover them.

Galileo Galilei(1564-1642)

3.1 Introduction

To study the flow of ions in the ion channel, we model the process describing the velocity of a single ion by using the Langevin equation as follows:

$$m\frac{\mathbf{v}(t)}{dt} = -\gamma\mathbf{v}(t) + \boldsymbol{\xi}(t), \tag{3.1}$$

where $\mathbf{v}(t)$ is the particle velocity, m its mass, γ the friction coefficient, and $\boldsymbol{\xi}(t)$ the white noise satisfying $\langle\boldsymbol{\xi}(t)\rangle = 0$, and $\langle\boldsymbol{\xi}_i(t)\boldsymbol{\xi}_j(s)\rangle = \delta_{ij}\delta(t-s)$. We start by considering an idealized bulk case, where we do not account for all the interactions between ions and the wall, or among themselves. Under those conditions, to obtain an expression for the power spectral

density of the particle's velocity, a Fourier transform over Eq. (3.1) is performed:

$$\widetilde{\mathbf{v}} = \mathbf{v}(\omega) = F(\mathbf{v}(t)) = \int_{-\infty}^{\infty} \mathbf{v}(t) e^{-i\omega t} dt. \tag{3.2}$$

$F(\mathbf{v}(t))$ in Eq. (3.2) denotes the Fourier transform of the velocity over a frequency domain ω. Rewriting Eq. (3.1) in Fourier space we get:

$$\begin{cases} -i\omega\widetilde{\mathbf{v}} = -\dfrac{\gamma}{m}\widetilde{\mathbf{v}} + \dfrac{1}{m}\widetilde{\boldsymbol{\xi}}, \\ \widetilde{\mathbf{v}}\big(-i\omega + \dfrac{\gamma}{m}\big) = \dfrac{1}{m}\widetilde{\boldsymbol{\xi}}, \\ \widetilde{\mathbf{v}} = \dfrac{\widetilde{\boldsymbol{\xi}}}{\gamma - i\omega m}. \end{cases} \tag{3.3}$$

Employing the Wiener-Khinchin theorem[6], the particle velocity power spectral density $S_v(\omega)$ reads:

$$S_v(\omega) = \lim_{T\to\infty} \frac{1}{T} \langle |v|^2 \rangle \sim \frac{S_\xi(\omega)}{\omega^2 + \gamma^2}. \tag{3.4}$$

$S_\xi(\omega)$ refers to the white noise power spectrum, given by $\int_{-\infty}^{\infty} \langle \boldsymbol{\xi}(t)\boldsymbol{\xi}(0) \rangle e^{i\omega t} dt = 2\gamma k_B T$, where k_B is the Boltzmann constant and T the temperature of the system. Replacing $S_\xi(\omega)$ in Eq. (3.4) by its corresponding expression we obtain:

$$S_v(\omega) = \frac{2\gamma k_B T}{m\omega^2 + \gamma^2}. \tag{3.5}$$

From another perspective, the total current density is directly proportional to the drift velocity of the ions, hence the current I through a surface S can be represented as follows:

$$\begin{cases} I = \int_S \mathbf{J} \cdot d\mathbf{A}, \\ I = \int_S \rho \langle \mathbf{v} \rangle \cdot d\mathbf{A}. \end{cases} \tag{3.6}$$

The integration in Eq. (3.6) is performed over $d\mathbf{A}$, a surface element of S. The ith charge, is characterised by a velocity $\mathbf{v}_i$ and a charge $q_i = \pm 1$, the total charge density ρ is equal to $\frac{\sum_{i=1}^{N} q_i}{V}$, the number density of the charges is represented by $\frac{N}{V}$, and the average velocity is defined as following: $\langle \mathbf{v} \rangle = \frac{1}{N} \sum_{i=1}^{N} \mathbf{v}_i$. The current densities can be expressed as the following:

$$\begin{cases} I = \int \langle \mathbf{v} \rangle \rho d\mathbf{A}, \\ I = \int (\mathbf{J}_+ - \mathbf{J}_-) d\mathbf{A}, \end{cases} \tag{3.7}$$

with the corresponding power spectrum:

$$\begin{cases} S_J(\omega) = \frac{1}{V} S_v(\omega), \\ S_J(\omega) = \frac{1}{V} \frac{2\gamma k_B T}{\omega^2 + \gamma^2}. \end{cases} \tag{3.8}$$

Equation (3.8) indicates that the current power spectral density would exhibit a behaviour inversely proportional to the square of the frequency for $\omega \gg \frac{\gamma}{m}$, indicating the existence of Brownian noise.

Nonetheless, the flow of ions in nanopores is influenced by confinement due to ions collisions among themselves, against the membrane walls, their interactions with the surface charges, and the gating process. All these conditions modify the expected Brownian noise in the current power spectral density and lead to an unexplained non-quadratic dependence on ω. In this chapter, we perform Langevin dynamics simulations to model the current flow of ions across a cylindrical pore. The ions were allowed to flow across a pore with fixed radius under the influence of a constant applied electric field. All parameters characterising our system including radius, ionic concentration, and electric field, were altered to study their influence on the generated current power spectral density. Using a single fitting parameter, the expression for the current power spectral density $S(\omega)$, theoretically derived in Chap.

2, is fitted to the corresponding generated current spectra from the Langevin-Dynamics simulations. Excellent agreement is found at high frequencies, however a clear discrepancy between both graphs occurs at low frequencies. To explain these observations, we refer to the framework of our mean-field theory based on ignoring ion-ion interactions in the derivation. To study the effect of this consideration, ion-ion interactions were turned off, and a new current power spectral density was derived. The new result highlighted the indispensable role played by the interionic interactions in generating the power law at low frequencies.

3.2 Simulation Details

We perform Langevin-Dynamics simulations of ions passing through a membrane pore under the influence of an applied electric field, using the molecular simulation package Espresso[143]. The Langevin equation for particle i reads:

$$m_i \frac{\partial \boldsymbol{u}_i}{\partial t} = -\sum_{j \neq i} \boldsymbol{\nabla} V_{ij} + \boldsymbol{F}_i - \gamma \boldsymbol{u}_i + \boldsymbol{\xi}_i, \tag{3.9}$$

with $\boldsymbol{u}_i(t)$ being the particle's velocity in units Å$/\tau$, and $\gamma = 1\ k_B T \tau/\text{Å}^2$ being the friction coefficient, with τ being the time scale and $k_B T$ being the thermal energy. The random force $\boldsymbol{\xi}_i(t)$ satisfies $\langle \boldsymbol{\xi}_i(t) \rangle = 0$, and $\langle \boldsymbol{\xi}_i(t) \cdot \boldsymbol{\xi}_j(t') \rangle = 6 k_B T \gamma \delta_{ij} \delta(t - t')$. Ions are the only dynamical particles in our simulation, hence we consider them to have equal mass $m_i = 1\ k_B T \tau^2/\text{Å}^2$, commendably incorporating the mass into the time scale τ (see 3.2.2). The index j runs over all other particles of the system and the potential $V_{ij}(r_{ij})$ (in units of $k_B T$) combines the Coulomb interactions and the Lennard-Jones interactions, truncated and shifted to form a Weeks-Chandler-Andersen potential,

$$V_{ij} = \ell_B k_B T \frac{Q_i Q_j}{r_{ij}} + 4\epsilon_{ij} \left[\left(\frac{\sigma_{ij}}{r_{ij}} \right)^{12} - \left(\frac{\sigma_{ij}}{r_{ij}} \right)^{6} \right] + V_{\text{shift}}, \tag{3.10}$$

where Q_i is the charge of the i-th particle in units of the elementary charge e and r_{ij} is the distance between particles i and j. To account for the strength of the Coulomb interactions, the Bjerrum length $\ell_B = e^2/(4\pi\varepsilon\varepsilon_0 k_B T)$, with ε_0 being the permittivity of vacuum, is set to $\ell_B = 7$ Å, modeling electrostatic interactions in water with a dielectric constant $\varepsilon = 80$. The long-ranged electrostatic interactions are treated using the P^3M (particle-particle-particle mesh) Ewald summation with an automatically determined real-space cutoff, ensuring accurate treatment of the electrostatic interactions between ions separated by large distances[143]. The Ewald summation conditions are developed in more details in section 3.3.

To avoid any overlapping, we used the Lennard-Jones potential truncated and shifted to zero at $r_{ij} = 2^{1/6}\sigma_{ij}$, using $V_{\text{shift}} = \epsilon_{ij}/4$, making $V_{ij} = 0$ and $\nabla V_{ij} = 0$ at the truncation length for every pair interaction, regardless of the value of σ_{ij}. For the Lennard-Jones parameters, we use $\epsilon_{ij} = 0.5\ k_B T$ for all particles, $\sigma_{ij} = 3$ Å for ion-ion interactions, and $\sigma_{ij} = 6$ Å for ion-membrane interactions[143]. The applied electric field along the pore length exerts a force in the $x_\parallel$-direction on each ion crossing the pore only, a condition that takes the following form:

$$\boldsymbol{F}_i = \begin{cases} Q_i \boldsymbol{E} & \text{if } 0 < x_\parallel < L \\ 0 & \text{otherwise,} \end{cases} \tag{3.11}$$

with $\boldsymbol{E} = (0, 0, E_\parallel)$. The electric field $\boldsymbol{E} = (0, 0, E)$ is varied between 0.5, 0.8, and 1.1 $k_{\mathrm{B}}T/\left(e\text{Å}\right)$ equivalent to a potential difference between 0.6 V and 1.2 V.

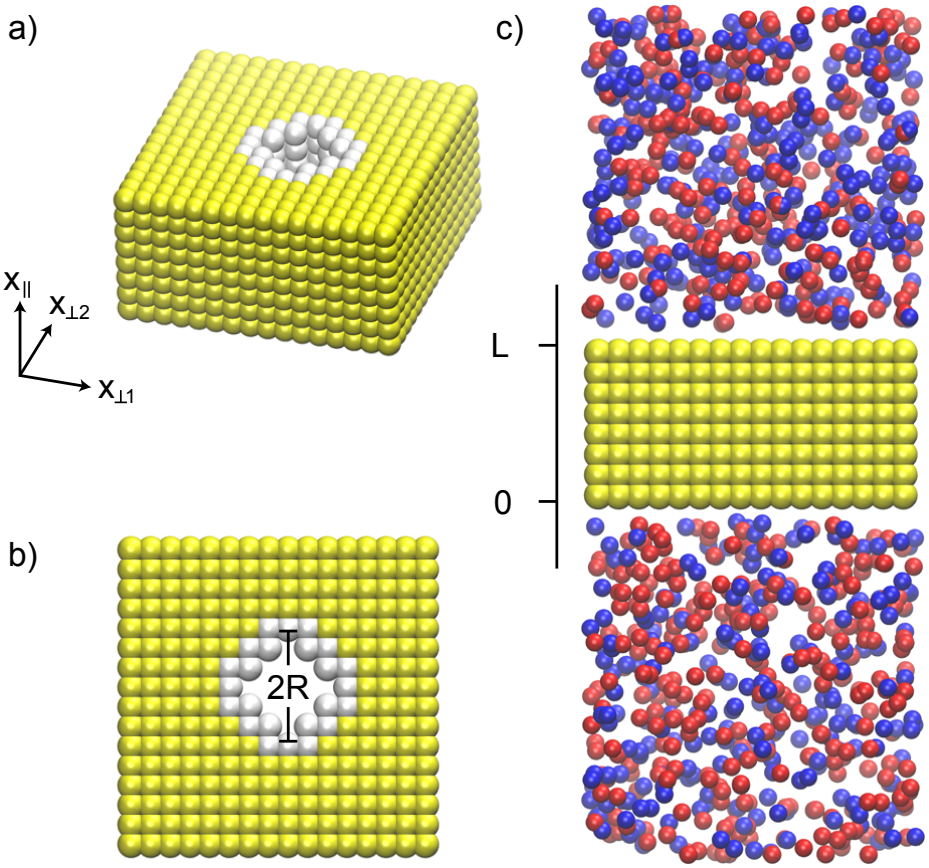

Figure 3.1: Simulation snapshots with (a) the membrane with the nanopore, (b) the top view of the membrane with the lateral pore size R indicated, and (c) the side view of the simulation box with the membrane thickness L indicated. The red and blue particles depict the charged ions, the yellow particles depict the membrane, and the surface particles that carry a partial charge in the case of a charged pore are shown in white. The membrane particles correspond to several atoms each, their size being chosen solely to make the membrane impermeable to ions. In (a) and (b) the ions are not shown. In (c) all the ions in the primary box are shown.

3.2.1 Building the Membrane and Distributing the Ions

We build an artificial membrane consisting of frozen particles on a cubic lattice with a lattice constant of 6 Å, of width $W = 100$ Å, length $L = 48$ Å, and height $H = 48$ Å. To reduce the number of particles in the simulation, the membrane is coarse-grained where each particle accounts for a group of atoms (see Fig. 3.1). Permeating the membrane, we construct an approximately cylindrical pore, with a radius varying between 19 Å, 25 Å, and 35 Å to allow the flow of ions and to approach the radii considered in experiments[114;119]. As it was explained in the introduction, the pore exhibits a gating process that can be approached using a flexible

membrane. In our analysis, the membrane can either be allowed to fluctuate through harmonic bonds built between the six nearest neighbours of all membrane particles or it can be fixed. Here, we model a frozen membrane with particles occupying specific positions. The lattice constant and the Lennard-Jones interaction parameters between the ions and the membrane were chosen accordingly as to avoid ion permeation across the membrane outside the pore area.

Ions concentration: $C_0(\text{Å}^{-3})$	0.001, 0.003, 0.0005
Electric field:$E_{\parallel}(e\text{Å}/k_BT)$	0.5, 0.8, 1.1
Radius:$R(\text{Å})$	$19, 25, 35$
Pore Length:$L(\text{Å})$	48

Table 3.1: Summary table for the parameters used in the simulations.

Monovalent positive and negative ions are placed uniformly at random into reservoirs of height $H = 50$ Å on either side of the membrane using three different concentrations, $C_0 = \{3 \times 10^{-3}, 1 \times 10^{-3}, 5 \times 10^{-4}\}$ Å^{-3}, corresponding to $C_0 = \{0.8, 1.7, 5.0\}$ mol/L.

3.2.2 Time scale

We define the time scale τ in our system as a function of the energy unit k_BT, the length unit Å and the particle's mass m as $\sqrt{m\text{Å}^2/k_BT}$. The time scale τ is derived by calculating the conductivity in a bulk system with an applied homogeneous electric field, and comparing it to the conductivity of a solution of potassium chloride.

To calibrate the time scale τ, we calculate the conductivity of a bulk system of ions of size 100^3 Å^3. On one side, the conductivity is derived from a linear fit of the current as a function of the electric field $\mathbf{E}$, as shown in Fig. 3.2. On the other side, experimentally, the conductivity is given by

$$\frac{1}{C_0}\frac{\mathrm{d}I}{\mathrm{d}E} = A\left(D^+ + D^-\right)\frac{e^2}{k_BT}, \tag{3.12}$$

with A the lateral area and $D^+ = D^- = 0.2$ Å^2/ps being the diffusion coefficient of K^+ and Cl^-. We plot the electrical conductivity $\frac{dI}{dE}$ as a function of the ionic concentration up to $C_0 = 3 \times 10^{-4}$ Å^{-3} (Fig. 3.2). From a linear fit of the resulting graph, and Eq. (3.12) we determine the time scale τ, which gives $\tau = 5$ ps.

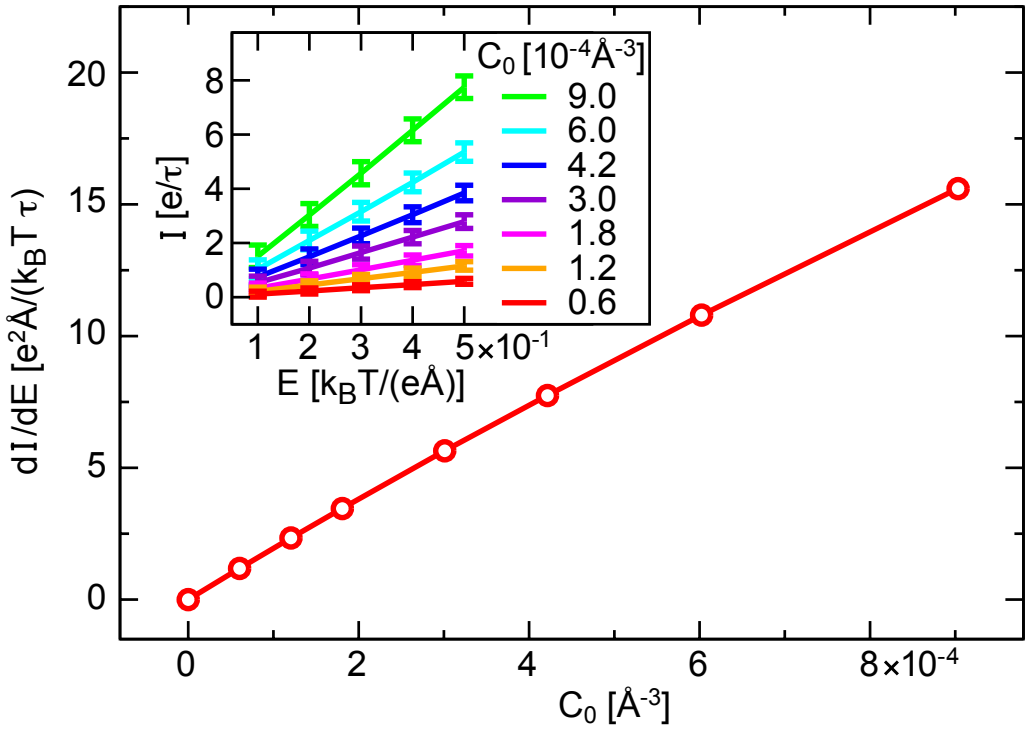

Figure 3.2: The electrical conductivity of a bulk system of ions ($100 \times 100 \times 100$ Å) as a function of the ionic concentration C_0. Inset: The current as a function of the electric field.

3.3 Simulation Initial and Boundary Conditions Details

As an initial condition, the electro-neutrality of the system has to be maintained. Thereby, the distribution of ions can be described as the sole initial condition. At time $t = 0$, the concentration of the two types of ions has to be proportional to their valence, hence cations and anions have equal concentrations. Apart from the neutrality condition, the total concentration of ions in the upper reservoir is equal to the total concentration of ions in the lower reservoir. Consequently, ions were distributed alternatively to obey the listed conditions that we describe

by the following set of equations:

$$\begin{cases} \sum_i z_i c_i = 0, \\ C_{\text{Lower Reservoir}} = C_{\text{Upper Reservoir}}. \end{cases} \tag{3.13}$$

As it was advanced, periodic boundary conditions were applied in three dimensional space to avoid edge effects. A central simulation box was built with two chambers of ions above and below the box. An infinite system is formed by replicating the constructed system in all the three dimensions. In any simulation or experiment, ions from different neighborhood may interact with each other. To account for this assumption, particularly long-ranged electrostatic interactions, we adopt the highly effective Espresso implemented P^3M (particle-particle-particle mesh) algorithm.

To develop more this proposition, we start by representing the Coulomb interactions between N atoms by the following equation:

$$E(\mathbf{r}_1, \mathbf{r}_2, ..., \mathbf{r}_N) = \frac{1}{2} \sum_{i=1}^{N} \sum_{j} \frac{q_i q_j}{r_{ij}}, \tag{3.14}$$

where $r_{ij} = |\mathbf{r}_i - \mathbf{r}_j|$ defines the distance between ion i with charge q_i and ion j with charge q_j. Nonetheless, introducing Coulomb interactions in simulation depends on the employed boundary conditions. Driven by the perodicity of our system, long-range Ewald summation was employed. An ion at location $\mathbf{r}_i$ will have an image located at $\mathbf{r}_i + n_1\mathbf{c}_1 + n_2\mathbf{c}_2 + n_3\mathbf{c}_3$, where n_1, n_2, and $n_3 \in \mathbb{Z}$ whereas $\mathbf{c}_1$, $\mathbf{c}_2$, and $\mathbf{c}_3$ present the repeating vectors describing the box dimensions. Using these definitions, Eq. (3.14) can be modified to account for the interaction between ions and their images as following:

$$E(\mathbf{r}_1, \mathbf{r}_2, ..., \mathbf{r}_N) = \frac{1}{2} \sum_{\mathbf{n}=(n_1,n_2,n_3)} \sum_{i=1}^{N} \sum_{j=1}^{N^*} \frac{q_i q_j}{|\mathbf{r}_{ij} + n_1\mathbf{c}_1 + n_2\mathbf{c}_2 + n_3\mathbf{c}_3|}. \tag{3.15}$$

The star is introduced to indicate that we exclude $i = j$ case when $\mathbf{n} = (0, 0, 0)$.

The summation in Eq. (3.15) converges very slowly $\sim (1/r)$, and its convergence is dependent on the ordering of the summations. To approach this argument, the concept of Ewald summation relies on splitting the potential in two terms the short-range potential E^s and the long-range potential E^L. By solving Poisson's equation, the short-range term of the Coulomb interactions takes the same form as Eq. (3.15) with a dependence on the error function erfc:

$$E^s(\mathbf{r}_1, \mathbf{r}_2, ..., \mathbf{r}_N) = \frac{1}{2} \sum_{\mathbf{n}=(n_1,n_2,n_3)} \sum_{i=1}^{N} \sum_{j=1}^{N^*} \frac{q_i q_j}{|\mathbf{r}_{ij} + n_1\mathbf{c}_1 + n_2\mathbf{c}_2 + n_3\mathbf{c}_3|} \mathrm{erfc}\left(\frac{|\mathbf{r}_{ij} + n_1\mathbf{c}_1 + n_2\mathbf{c}_2 + n_3\mathbf{c}_3|}{\sqrt{2}\sigma} \right). \tag{3.16}$$

The error function in Eq. (3.16) truncates the potential at large distances.

However, computing the slowly convergent long-range potential by a direct sum in real space is very time consuming. For this reason, and to approach a solution for E^L, Ewald's idea is based on making the summation short-range and rapidly decaying by evaluating it in reciprocal space[144;145].

Despite the fact that Ewald sum presents a quicker and efficient approach to compute the Coulomb interactions, the Fourier transform part of the Coulomb interactions can still be computationally demanding in very expensive simulations with large number of particles. For this reason, to evaluate Ewald sum Espresso package uses a particle Mesh Ewald Truncation method for electrostatic interactions based on the particle-particle-particle-mesh (P^3M) method introduced by Hockney and Eastwood[146;147].

The main idea of the P^3M method relies on mapping the system into a mesh where a Fast-Fourier transform is applied, a method that decreases relatively the intricacy of the system(Fig. 3.3). A cutoff r_c is used to calculate the real space interactions (Particle-Particle), whereas the reciprocal space interactions are calculated by mapping the system to a mesh (Particle-Mesh). Every charge will be assigned to this mesh, a Fast-Fourier transform FFT is

then applied on the mesh charge density, and using Poisson's equation the electric field is calculated. Finally, the mesh electric field is mapped back to real space at particles' positions and the force experienced by each particle is then derived[148;149].

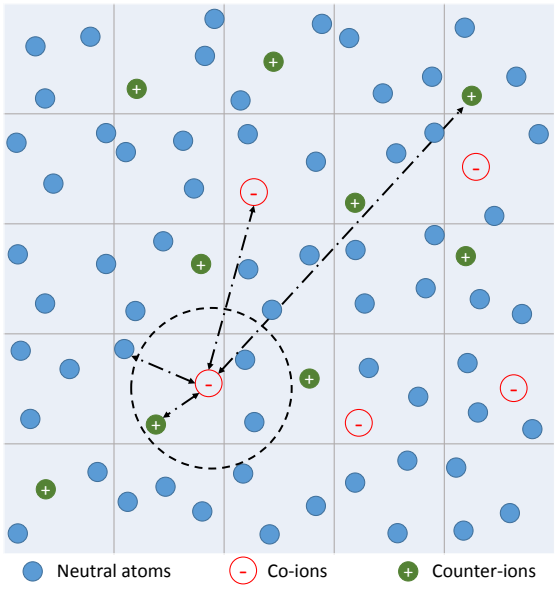

Figure 3.3: A two dimensional presentation of the system and particles mapped to a mesh to calculate the reciprocal space Coulomb interactions using P^3M algorithm. At each mesh point, the reciprocal electrostatic energy and potential are calculated.

Espresso is characterised by a function that determines the appropriate cutoff and mesh points values required for our system. The function is based on determining different appropriate set of parameters, and based on the time required by each set to compute the Coulomb interactions it chooses the set with the shortest time. More details are provided in[143;150]. Using Espresso tuning feature, Espresso was instructed to determine the mesh size, and cutoff with a rms force error below 10^{-4} $k_BT/\text{Å}$ between the exact continuous space result and the mesh calculation[149;151].

Finally, one of the main issues that should be taken care of is the charge density in the two baths that should be carefully maintained. By specifying the concentration, the number of ions in every bath was fixed at the beginning of every simulation. To maintain the initial concentration setting, any ion escaping a chamber will be replaced by another ion akin to an elastic reflection process. Whenever an imbalance situation takes place, ions will be reflected

from one chamber of the reservoir to the other.

3.3.1 Equilibration Loop

The system is prepared using two chambers of ions with random initial conditions. Before extracting any useful measurement the system needs to be monitored as it relaxes towards equilibrium[152–155].

The arbitrary distribution of ions allows us to consider different nonequilibrium initial states, leading to different trajectories towards equilibrium. To conclude the optimal relaxation time required for the system to move from any initial random configuration to equilibrium, the time evolution of the temperature and the energy of different systems characterised by different initial conditions are observed as a function of time. Figure 3.4 illustrates the relaxation behaviour by showing the pattern followed by the energy and the temperature as a function of time for systems with different ionic concentration. Despite beginning from different initial states, the temperature and the energy of all the systems converge towards constant values. Using those measurements, we arrive at the average characteristic time required by the system to reach its equilibrium state. The temperature was calculated by accounting for the number of ions and the number of degrees of freedom. Tables 3.2 and 3.3 below list the average values of the temperature and the energy of the system after the relaxation phenomena with the corresponding standard deviation for six different samples with different ionic concentrations.

Moreover, because of the random distribution of ions when building the system, the overlap energy reaches millions of k_BT, a condition that needs to be revised before taking any measurement, otherwise the system will blow up. To approach this issue, we can cap the forces by allowing the Lennard-Jones potential to acquire a constant value below a certain radius. The following equilibrium loop idea is applied.

The idea is based on integrating the system with an initial force cap 10 with an increment of

10 and final force cap 500. The energy and the temperature are printed at each cap value to ensure that we reach a constant value. Finally, the cap is reset to 0, and the simulation can be carried on.

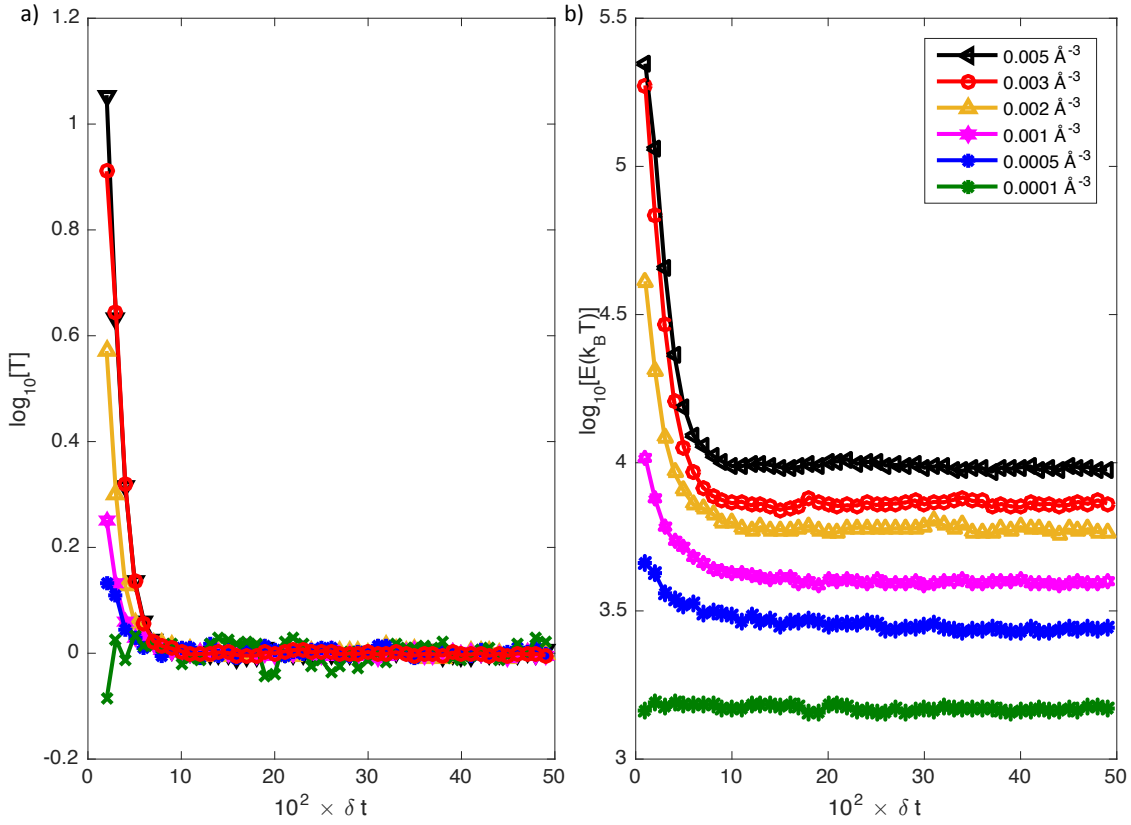

Figure 3.4: The temperature and the energy relaxation values as a function of the time step. To get the above example results a pore with radius $R = 25$ Å and a varying concentration from 0.0001 Å^{-3} to 0.005 Å^{-3} were used. Figure (a) shows that the temperature stabilizes around 1 and Figure (b) shows as well that the energy reaches a constant value that increases at higher ionic concentration.

Concentration $C_0(\text{Å}^{-3})$	Average Temperature	Temperature standard deviation
0.005	0.9991	0.0072
0.003	1.0011	0.0070
0.002	1.0006	0.0110
0.001	0.9973	0.0105
0.0005	1.0004	0.0048
0.0001	1.0002	0.0067

Table 3.2: The average temperature in the last 3000 steps of the equilibration loop. It shows that the temperature stabilizes varying marginally around 1.

Concentration $C_0(\text{Å}^{-3})$	Average Energy(k_BT)	Energy standard deviation
0.005	9.7157×10^3	232.8076
0.003	7.2929×10^3	129.3007
0.002	5.9544×10^3	132.9434
0.001	$3.9516e \times 10^3$	57.6333
0.0005	2.7701×10^3	62.1763
0.0001	1.4730×10^3	23.0262

Table 3.3: The average system energy in the last 3000 steps of the equilibration loop. It shows that the energy stabilizes with very small standard deviation around 2% .

3.3.2 Integration Method

We employ the velocity-Verlet algorithm for the integration of the equations of motion. Its idea is based on updating particle i velocity $\mathbf{u}_i(t)$ to $\mathbf{u}_i(t + \frac{\Delta t}{2})$ based on the force $\mathbf{f}_i(t)$ experienced by the particle (Eq. (3.17a)). Using the new velocity $\mathbf{u}_i(t + \frac{\Delta t}{2})$ the position of the particle is then updated from $\mathbf{r}_i(t)$ to $\mathbf{r}_i(t + \Delta t)$ as shown in Eq. (3.17b) and the new corresponding force $\mathbf{f}_i(t + \Delta t)$ is then determined. Finally the velocity will be propagated again to $\mathbf{u}_i(t + \Delta t)$ based on Eq. (3.17c). Following those steps, the simulation time is moved.

$$\mathbf{u}_i(t + \frac{1}{2}\Delta t) = \mathbf{u}_i(t) + \frac{\Delta t}{2}\frac{\mathbf{f}_i(t)}{m_i} \tag{3.17a}$$

$$\mathbf{r}_i(t + \Delta t) = \mathbf{r}_i(t) + \Delta t \mathbf{u}_i(t + \frac{\Delta t}{2}) \tag{3.17b}$$

$$\mathbf{u}_i(t + \Delta t) = \mathbf{u}_i(t + \frac{\Delta t}{2}) + \frac{\Delta t}{2}\frac{\mathbf{f}_i(t + \Delta t)}{m_i}. \tag{3.17c}$$

We use Langevin-Thermostat for the system to ensure that the simulation will be performed at an average constant temperature with particles having the appropriate velocities. The idea is based on slowing down and accelerating particles by applying the appropriate forces [156–158]. A random force $\boldsymbol{\zeta}_i(t)$ with zero average and an autocorrelation function $\langle \boldsymbol{\zeta}_i(t) \cdot \boldsymbol{\zeta}_j(t') \rangle = 2k_BT\gamma\delta_{ij}\delta(t - t')$ will be applied on every particle at every time step, where γ is the friction coefficient. This process can be simply represented by the Langevin equation for particle i

with mass m_i, velocity $\mathbf{u}_i$, and momentum $\mathbf{p}_i = m_i\mathbf{u}_i$:

$$m_i\dot{\mathbf{u}}_i = -\boldsymbol{\nabla}_i V - m\gamma\mathbf{u}_i + \boldsymbol{\zeta}_i(t). \tag{3.18}$$

The Langevin thermostat can operate due to the presence of the friction coefficient set to $\gamma = 1k_BT\tau/\text{Å}^2$ [143]. To elaborate on this concept, Eq. (3.18) is modified so as to describe the change in momenta at each time step as following:

$$\dot{\mathbf{p}}_i = -\boldsymbol{\nabla}_i V - \gamma\mathbf{p}_i + \boldsymbol{\zeta}_i(t). \tag{3.19}$$

Equation (3.19) indicates that the final canonical ensemble will be built through the combination of the momenta damping factor $\gamma\mathbf{p}_i$ and the random force $\boldsymbol{\zeta}_i$ [159–161].

The role of the Langevin-Thermostat extends to handling the random noise term. As explained in the velocity-Verlet method in the previous paragraph, any change in the particles interactions leads to a force recalculation at every time step including any random term. To deal with this situation, the amplitude of the random noise is modified. This can be done by rescaling the noise by $\sqrt{3}$ when entering a new integration loop, a solution that is taken into account by Langevin-Thermostat in Espresso [143;162–165].

3.3.3 Finite-Size Effect

Periodic boundary conditions were applied in all directions. We verify that the effect of the periodic boundary conditions, which affects fluctuations in general [166], is negligible in our case.

To study the influence of the simulation box size, we vary the reservoir size between 50 Å and 288 Å in the parallel direction($x_\parallel$) and between 96 Å and 288 Å in the planar direction($x_\perp$). The corresponding current power spectra are shown in Fig. 3.5. As the figure displays, the generated spectra are independent of the reservoir size, an aspect that demonstrates that

periodic boundary conditions do not affect the ion fluctuations.

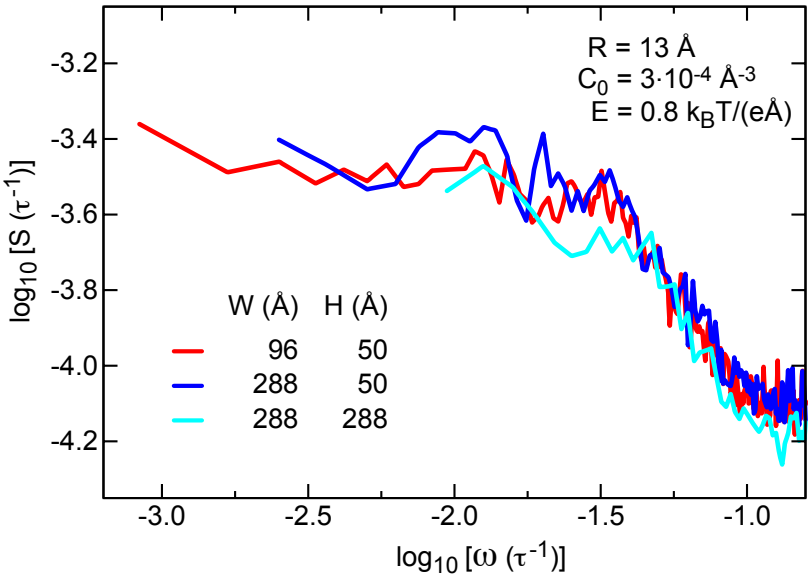

Figure 3.5: The current power spectra of pores with radius $R = 13$ Å and length $L = 48$ Å, each connected to two reservoirs of size $W \times W \times H$. The total simulation box is $W \times W \times L + 2H$, with periodic boundary conditions in all directions. The simulations are performed with $V_{ion\text{-}ion} = 0$.

3.4 The Current Fluctuations derived from the Simulations

Using a time step $\delta t = 0.006\tau$, we perform simulations of 4×10^8 time steps, discarding 5000 steps for equilibration. We calculate the current $I_{\parallel}(t) = \int_A [J_{\parallel}^{+}(\boldsymbol{x}, t) - J_{\parallel}^{-}(\boldsymbol{x}, t)]\, \mathrm{d}\boldsymbol{x}$, from the integrated velocity in parallel direction:

$$I_{\parallel} = \frac{1}{L} \sum_i \begin{cases} Q_i \left(\boldsymbol{u}_i\right)_{\parallel} & \text{if } 0 < x_{\parallel} < L \\ 0 & \text{otherwise,} \end{cases} \tag{3.20}$$

where the index i runs over all positive and negative ions. From the current, using the Welch method with a Hamming window and an overlap of 0.5, we calculate the power spectrum in frequency domain $S_I(\omega) = \left|I(\omega)\right|^2$ [167].

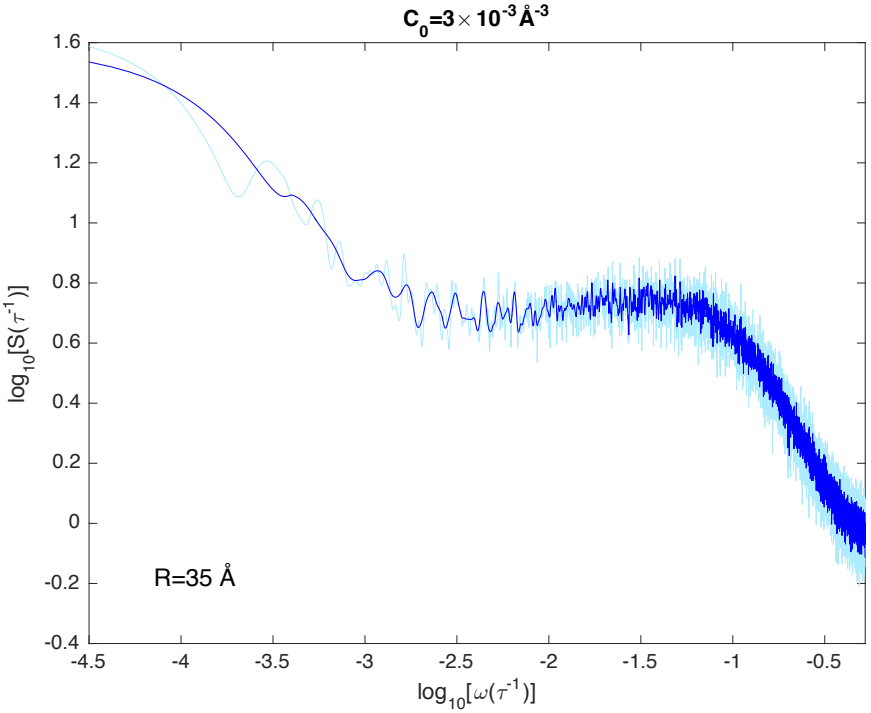

Figure 3.6: Power spectrum of the ionic current through a pore of $R = 35$ Å at a concentration of $C_0 = 3 \times 10^{-3}$ Å^{-3} (5.0 mol/l), at an applied electric-field $E_{\parallel} = 0.8\ k_B T/(e\text{Å})$. It features two power-laws at low and high frequencies connected by a transition domain.

Discarding the background white noise at very high frequencies, two decreasing power-law connected by a transition frequency describe the generated current power spectral density as shown in Fig. 3.6.

The time consumed by a simulation to generate a power spectral density depends largely on the concentration of ions imposed. On average, a simulation with $C_0 = 0.0005$ Å^{-3} required a month of 16 Dual-cores CPU time and increased to two months when $C_0 = 0.003$ Å^{-3} or one month and a half when $C_0 = 0.001$ Å^{-3}.

3.5 Comparison of Simulation and Theory

Throughout our simulations, several parameters were altered independently, and their induced effects on the current fluctuations were explored.

Figure 3.7 shows the obtained spectrum of ionic current fluctuations from the simulations

performed over a range of various parameters. All the generated spectra at high frequency ω can be described by a power law, inversely proportional to the frequency $S \propto 1/\omega^b$ covering approximately one order of magnitude, and a small bump independent of the frequency. At low frequencies, a second power law is perceived, before it again saturates at higher noise level. The two regimes are connected by a transition frequency that occurs around $\omega = 10^{-2}\ \tau^{-1}$. The perceived plateau at low frequencies has been predicted by Hooge and Tasserit et al., but was never seen experimentally[35;133]. We fit the low-frequency increase with another power law $S \propto 1/\omega^a$. The black dashed lines represent the theoretical prediction of equation (2.25) in Chap. 2, which provides a perfect fit for all values of the parameters used without any further rescaling using $\Lambda = 3$ Å, $D = 1$ Å$^2/\tau$, and C_{pore} calculated from the simulations. The fitting matches the power law perfectly at high frequencies, but a clear discrepancy is seen at low frequencies. Whereas the fitting is characterised by a plateau at low frequencies, the simulated power spectral density $S(\omega)$ continues to increase with decreasing frequency, a behaviour reminiscent of the $1/\omega^\alpha$ found experimentally.

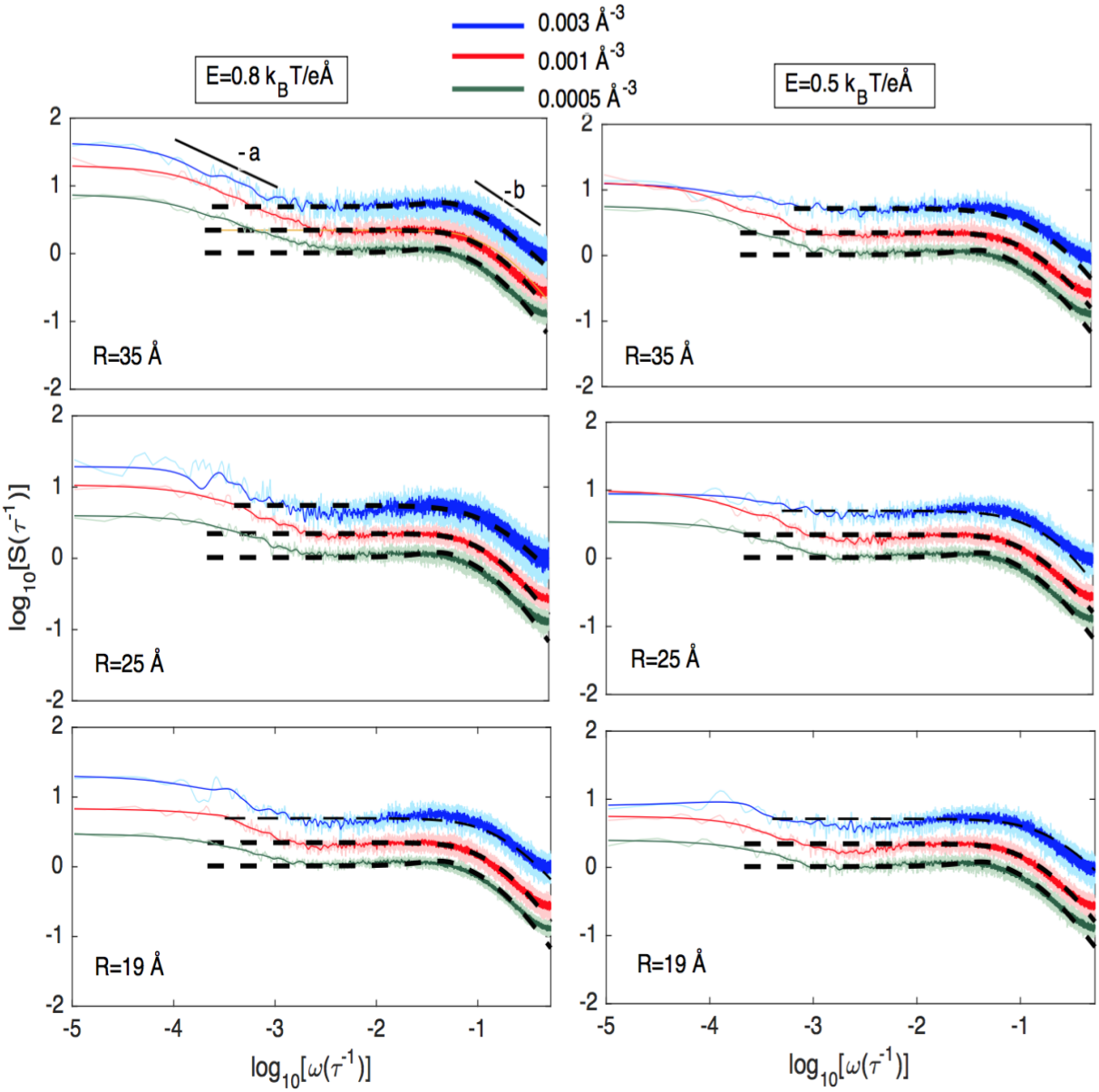

Figure 3.7: The current power spectral density $S(\omega)$ of the ionic current in units of the inverse of the time scale τ, as a function of the frequency ω on a log-log scale, for ion concentrations (a) $C_0 = 5 \times 10^{-4}$ Å^{-3} (0.8 mol/l), (b) $C_0 = 1 \times 10^{-3}$ Å^{-3} (1.7 mol/l), and (c) $C_0 = 3 \times 10^{-3}$ Å^{-3} (5.0 mol/l). The solid curves denote $S(\omega)$ from simulations, smoothed using a moving average for improved clarity, and the shaded areas indicate the standard deviation of the blocks. The dashed lines denote fits to Eq. (2.25). The diffusion coefficient $D = 1$ Å$^2/\tau$ and the small-scale cutoff length is set to the ion size, $\Lambda = 3$ Å, for all curves. The applied electric field are $E_\parallel = 0.5\ k_BT/(e\text{Å})$ and $E_\parallel = 0.8\ k_BT/(e\text{Å})$.

3.5.1 The Characteristic Exponents Describing the Power Laws

The power laws at low and high frequencies are described by two exponents a and b as it is shown in Fig. 3.7. As the concentration is increased from $C_0 = 5 \times 10^{-4}$ Å^{-3} to

$C_0 = 1 \times 10^{-3}$ Å^{-3} and $C_0 = 3 \times 10^{-3}$ Å^{-3} at all the radii implemented, $R = 19,\ 25$, and 35 Å, the power a describing the low frequency regime increases from 0.24 to 0.65 (see Fig. 3.8). This positive correlation between the power law exponent a and the concentration and the radius delineates the major role played by the ion transport in the generation of the power law at low frequencies (More results are shown in Chap. 5).

However, the exponent b proven not to vary for any radii larger than 19 Å, appears to follow this relation, as it is shown in Fig. 3.9 (details in Chap. 5)[2]. Otherwise, increasing the ion concentration as shown in Fig. 3.9, appears to influence very negligibly the value of the exponent b as predicted from the mean-field theory[2].

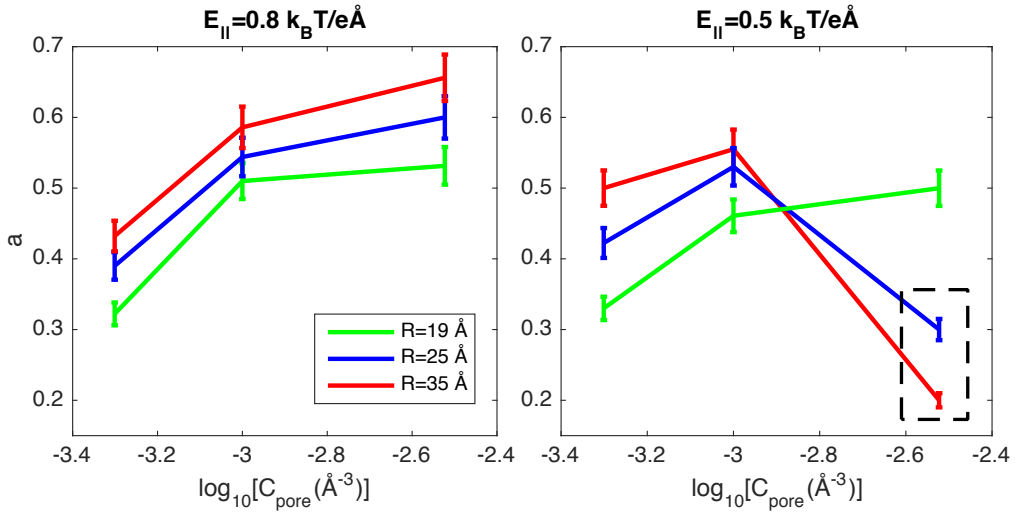

Figure 3.8: The exponent a of the fits $S(\omega) \approx \omega^{-a}(-4.5 < \log_{10}\omega < -2.6)$ as a function of the ion concentration C_0, at two electric fields $E_{\|} = 0.5\ k_BT/(e\text{Å})$ and $E_{\|} = 0.8\ k_BT/(e\text{Å})$. An anomalous behaviour is indicated by the black dashed square in the right panel, where a sudden decrease in the exponent occurs provoked by ions freezing at low electric field.

3.6 Ion Correlations Major Role

The discrepancy observed between the mean-field theory and the simulation behaviours at low frequencies and the strong dependence of the exponent a on C_0 suggests a strong effect of ion correlations, a feature that needs to be explored. To investigate this low-frequency power-law dependence of the power spectrum in more details, we perform simulations with

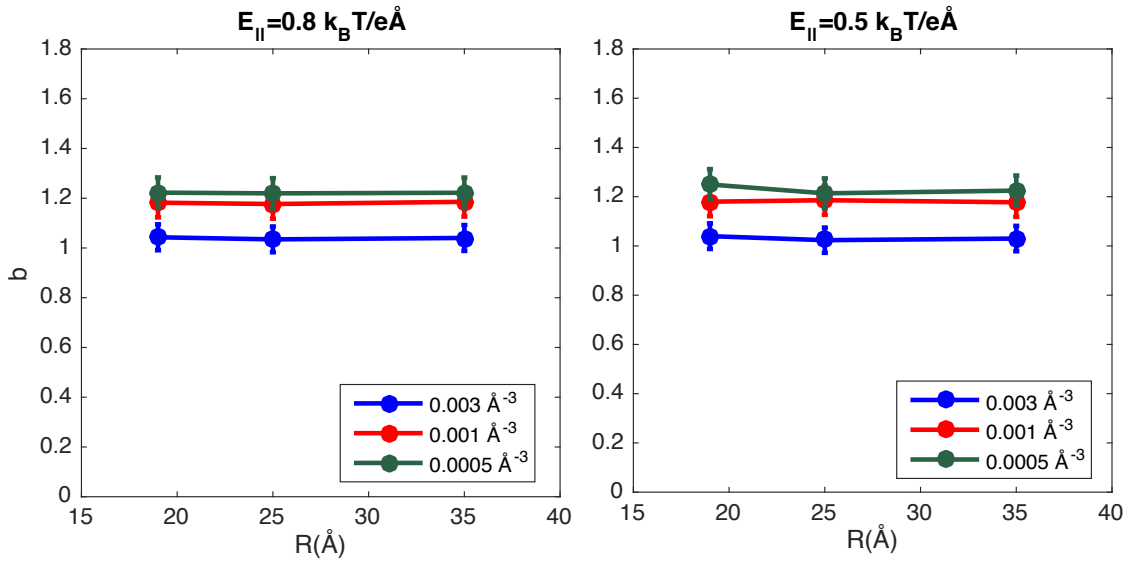

Figure 3.9: The power b of the fits $S(\omega) \propto \omega^{-b}$ $(-1.0 < \log_{10}\omega < -0.4)$ as a function of the radius R at two electric fields $E_{\parallel} = 0.5\ k_BT/(e\text{Å})$ and $E_{\parallel} = 0.8\ k_BT/(e\text{Å})$.

$V_{ion-ion} = 0$ (Eq. (3.10)) for the ion-ion interactions at two concentrations that lead to high values for the exponent a. In the first simulation, we use the concentration $C_0 = 3 \times 10^{-3}$ Å^{-3} (5.0 mol/l), $R = 35$ Å, and $E_{\parallel} = 0.8\ k_BT/(e\text{Å})$, whereas in the second simulation, we use a lower concentration $C_0 = 1 \times 10^{-3}$ Å^{-3} (1.67 mol/l), $R = 19$ Å, and $E_{\parallel} = 0.8\ k_BT/(e\text{Å})$. Ion-membrane interactions were left unchanged. We perform very expensive simulations to extract more data at low frequencies. In Fig. 3.10, the two extracted power spectra after the elimination of ion-ion interactions are plotted on top of the power spectra obtained with full interactions. Clearly, with $V_{ion-ion}(r_{ij}) = 0$ the power spectrum saturates at low frequency; a behaviour that matches quantitatively with our theoretical predictions (dashed lines) without any further adjustments regardless of the parameters used.

However, the current spectra obtained from our simulations at both ion concentrations, with full ion-ion interactions between multiple ions in our system (Eq. (3.10)), exhibit a power-law behaviour at low frequencies with an exponent that is significantly different from zero. This remarkable result revokes the conditions considered when deriving the mean-field theory power spectrum equation. To avoid any non-linear terms, we did not include ion correlations, a condition that we conclude to be mandatory for the generation of the low frequency power

law.

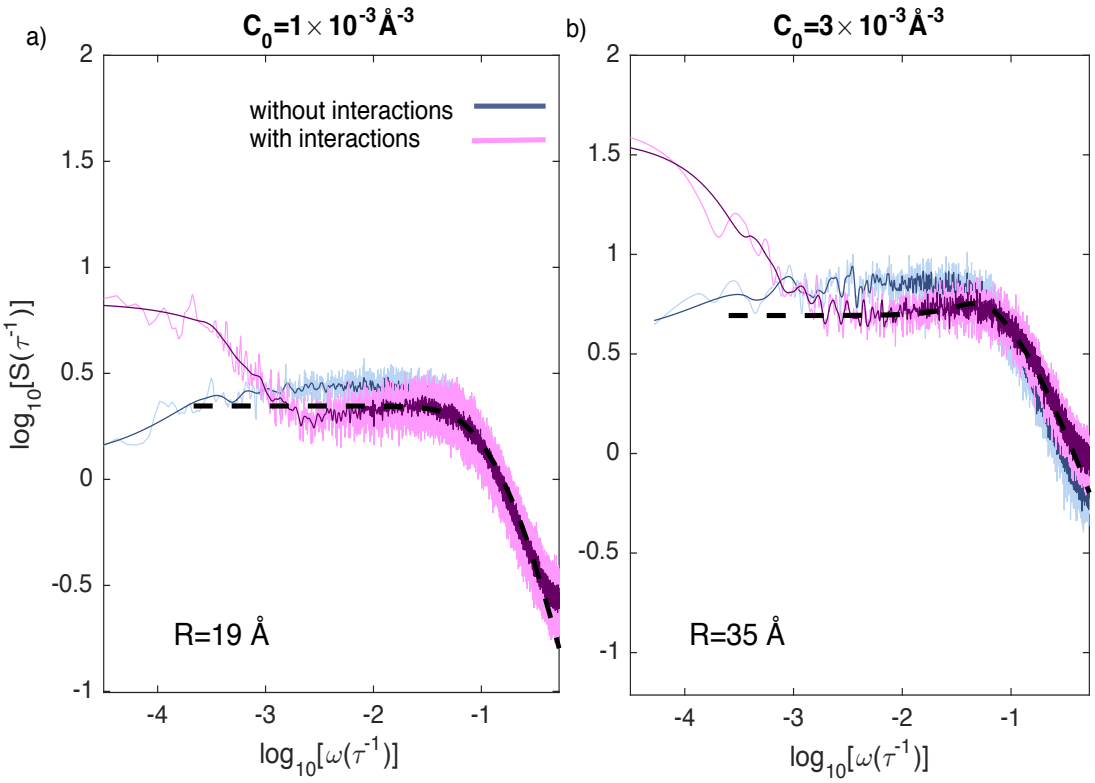

Figure 3.10: The current power spectrum with the ion-ion interactions potential $V_{ion-ion}(r_{ij})$ given by Eq. (3.10) (with interactions, violet line) and with $V_{ion-ion}(r_{ij}) = 0$ (without interactions, blue line). (a) The spectrum is calculated in a $R = 19$ Å channel with $E_{\|} = 0.8\ k_BT/(e\text{Å})$, and $C_0 = 1 \times 10^{-3}$ Å^{-3}. (b) The spectrum is calculated in a $R = 35$ Å channel with $E_{\|} = 0.8\ k_BT/(e\text{Å})$, and $C_0 = 3 \times 10^{-3}$ Å^{-3}. The dashed lines in both figures denote fits to Eq. (2.25). The diffusion coefficient $D = 1$ Å$^2/\tau$ and the small-scale cutoff length is set to the ion size, $\Lambda = 3$ Å, for all curves.

3.6.1 The Influence of the Electric-Field on the Current Fluctuations

In the simulations analysed above, we used two different electric fields $E_{\|} = 0.5\ k_BT/(e\text{Å})$ and $E_{\|} = 0.8\ k_BT/(e\text{Å})$. As Fig. 3.7 and Fig. 3.11 indicate, a higher electric field plays a role in generating a higher exponent a at low frequencies. To explore the validity of this feature, we have performed two simulations at a higher electric field $E_{\|} = 1.1\ k_BT/(e\text{Å})$, using the highest ionic concentration $C_0 = 3 \times 10^{-3}$ Å^{-3} (5.0 mol/l), and radii $R = 25$, 35 Å. Figure 3.11 below depicts the corresponding results.

Noticeably, the power a derived from the simulation perfomed using a pore with radius

$R = 35$ Å increased from ≈ 0.65 to 0.72 and from 0.60 to 0.70 when dealing with a pore of radius $R = 25$ Å (More results are shown in the appendix (8.3)). Those results delineate distinctly the role played by the electric field in generating a higher exponent a at low fequencies, but it is not the key reason behind its persistence.

Another crucial role for the electric field prevails in preventing ion blockage. When dealing with high ionic concentration and low electric field, ions start to build up along the pore length and block the current flow. Those conditions will not only alter the Debye length but also accumulated ions will affect the flow of like-charge ions. Increasing electric field will drive ions and avoid this problem as shown in Fig. 3.11 [168–171]. The response of the power spectrum to a weaker or a stronger electric field is further developed in Chap. 5.

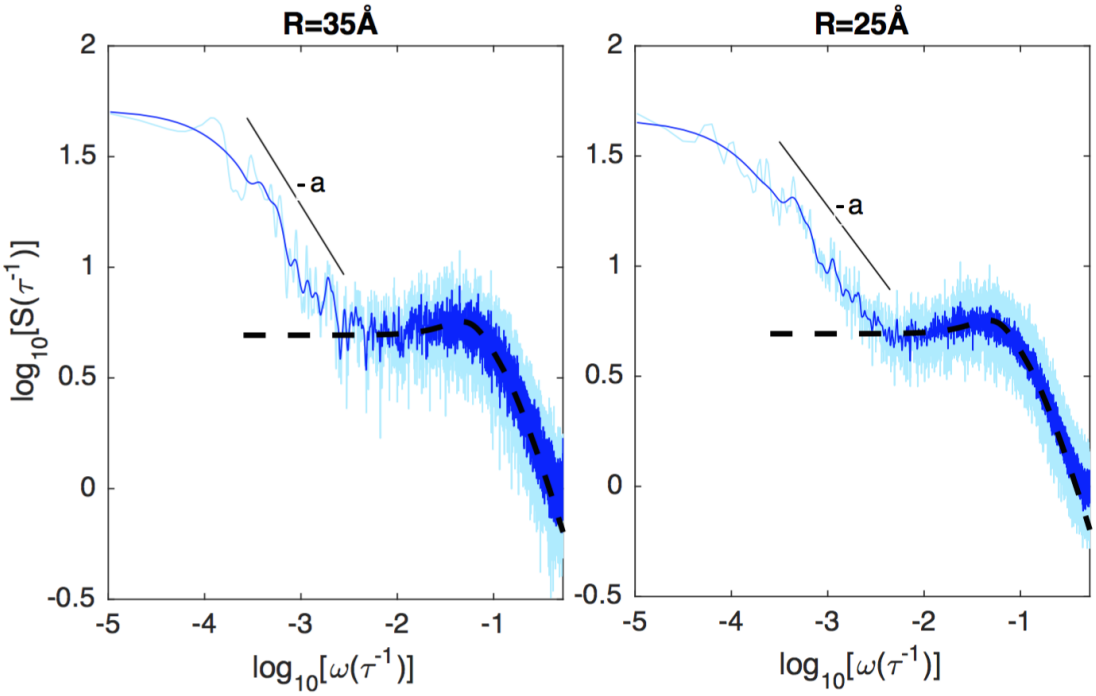

Figure 3.11: The current power spectra calculated in a $R = 25$ Å and $R = 35$ Å channels with $E_{\|} = 1.1\ k_BT/(e\text{Å})$, and $C_0 = 3 \times 10^{-3}$ Å^{-3}. The exponent a characterising the power law at low frequencies increases to 0.72 for $R = 35$ Å and 0.62 for $R = 25$ Å. The dashed lines denote fits to Eq. (2.25). The diffusion coefficient $D = 1$ Å$^2/\tau$ and the small-scale cutoff length is set to the ion size, $\Lambda = 3$ Å, for the two curves.

3.6.2 The Current Power Spectral Density On a Linear Scale: Any New Features?

Figure 3.12 shows the current power spectral density plot on a linear scale. The plot in the top panel represents the current power spectral density derived from a simulation including ion-ion interactions $V_{ion-ion}$ (Eq. (3.10)) and the plot in the bottom panel illustrates the simulation results without ion-ion interactions. Figure 3.12 is the corresponding linear plot of Fig. 3.10(b).

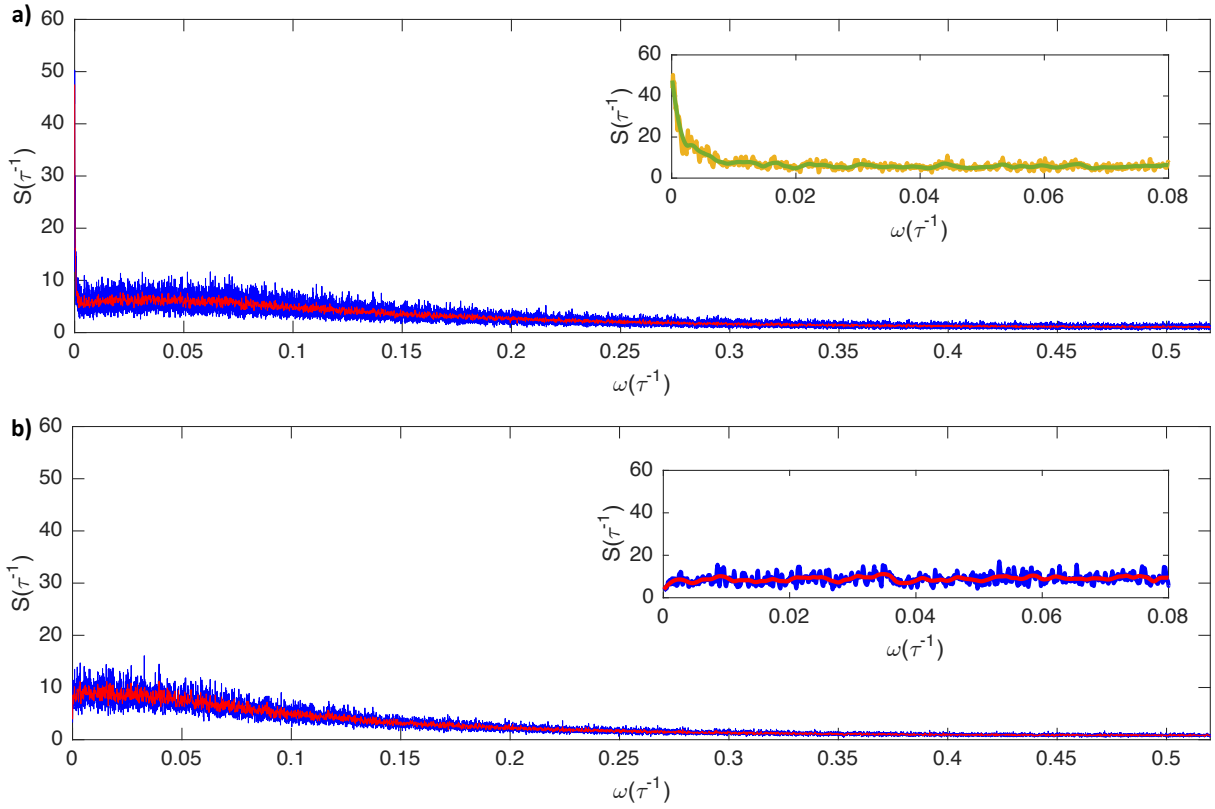

Figure 3.12: (a) The current power spectral density involving interionic interaction potential $V_{ion-ion}\,(r_{ij})$ given by Eq. (3.10). (b) The current power spectral density without ion-ion interaction potential $V_{ion-ion}\,(r_{ij}) = 0$. To get the spectra, an ion channel with radius $R = 35$ Å was used. The ion concentration was set to $C_0 = 3 \times 10^{-3}$ Å^{-3} and the electric field applied is $E_{\|} = 0.8\ k_B T/(e\text{Å})$.

As the insets of the figures indicate explicitly, when the Coulomb interactions are included, the current power spectral density shows a major decrease that recalls the power law at low frequencies. At higher frequencies, the power spectrum shows a very modest decrease

that corresponds to the bump and the high frequency power law observed in the logarithmic plot. Similarly, when the Coulomb interactions are turned off, a slowly decreasing behaviour is observed followed by white noise at very high frequencies, in total agreement with the logarithmic plot.

3.7 Conclusion

To explore the applicability of our theory derived in Chap. 2, we calculate the current power spectrum of electric-field-driven ion transport through cylindrical nanometer-scale pores. The power spectra derived from the simulations are fitted using the Linearized mean-field theory expression. Whereas the linearized mean-field theory predicts a plateau in the current power spectrum at low frequencies, the simulations did not, but instead a power law is present. However, at high frequencies the linearized mean-field theory predicts a decreasing power law that accurately describes the simulation data. The power law $S(\omega) \propto 1/\omega^a$ at low frequencies showed a clear increase from 0.2 to 0.72, with the ion concentration, a strong evidence on the role of ion-ion interactions.

To analyse those findings, and the disagreement between theory and simulations, we generated the current power spectral density after removing ion-ion interactions. The resulting spectra indicated clearly that the deviation from the mean-field theory plateau is induced by ion-ion correlations that were not included in the theory derivation. Other factors that influence the ion-ion interactions, such as a bigger radius or a higher electric field, reduce the probability of freezing, and enhance the power law.

All the above conclusions are supported by further analysis detailed in Chap. 5.

CHAPTER 4

Linearized Mean Field Theory Simplified

Everything should be made as simple as possible but not simpler.

Albert Einstein (1879-1955)

4.1 Introduction

In Chap. 3, using the equation derived for the current fluctuations, we succeeded to highlight a new source for the long-studied $1/f$ noise. However, the full expression for the current fluctuations developed in Chap. 2 looks very complicated, and it would be helpful if under certain conditions Eq. (2.18) can be simplified without losing the essence of the theory. The question regarding the existence and the applicability of a reduced form for $S(\omega)$ will be developed throughout this chapter.

To approach a simplified form for the current fluctuations expression $S(\omega)$, we divide the current density fluctuations equation into two categories: The terms including the screening factor C_{pore} were grouped together and the terms independent of C_{pore} were put in a separate fraction. By considering the value of C_{pore} and the order of magnitude of the dependent terms, we conclude that their influence on the overall spectrum could be simplified to

an amplitude difference and a small frequency shift that we can account for using other variables. Rearranging the left-over terms, we derive a simplified version for the current density fluctuations expression $\left\langle \left| \widetilde{J}_{\parallel}^{+}(\mathbf{q},\omega) - \widetilde{J}_{\parallel}^{-}(\mathbf{q},\omega) \right|^2 \right\rangle$. The limits are studied using the same criteria, and again similar trends were extracted.

In section (4.5), we study another suitable choice for the integrand. We show in particular how an integration over an area section in the bulk can be used to calculate the current power spectrum.

A detailed comparison between both versions of the current fluctuations expression $S(\omega)$ is explicitly visualised in section (4.6), where the similarities between the complete and the simplified form of $S(\omega)$ are clearly illustrated.

4.2 Current Fluctuations

The concluded expression for the current fluctuations derived in Chap. 2 took the following form:

$$S(\omega) = \frac{1}{2\pi^2} \int_{\pi L^{-1}}^{\pi \Lambda^{-1}} \mathrm{d}q_{\parallel} \int_{\pi R^{-1}}^{\pi \Lambda^{-1}} q_{\perp} \mathrm{d}q_{\perp} \left|\widetilde{\mathcal{A}}(q_{\perp})\right|^2 \left|\widetilde{\mathcal{L}}(q_{\parallel})\right|^2 \langle | \left[\tilde{J}^{+}(\mathbf{q},\omega) - \tilde{J}^{-}(\mathbf{q},\omega) \right] |^2 \rangle, \quad (4.1)$$

where the current density fluctuations $\langle | \left[\tilde{J}^{+}(\mathbf{q},\omega) - \tilde{J}^{-}(\mathbf{q},\omega) \right] |^2 \rangle$, was calculated as:

$$\begin{aligned}
&\left\langle \left| \widetilde{J}_{\parallel}^{+}(\mathbf{q},\omega) - \widetilde{J}_{\parallel}^{-}(\mathbf{q},\omega) \right|^2 \right\rangle = \\
&4DC_{\mathrm{pore}} \Bigg[1 + \frac{\omega^2 \left[D^2 \mathcal{E}_{\parallel}^2 q^2 [2q_{\parallel}^2 + q^2] - \kappa^2 D^2 q_{\parallel}^2 (\kappa^2 + 2q^2) - D^2 q_{\parallel}^2 q^4 \right]}{q^2 \left[(-\omega^2 + D^2 q^4 + D^2 q^2 \kappa^2 + D^2 q_{\parallel}^2 \mathcal{E}_{\parallel}^2)^2 + \omega^2 D^2 (2q^2 + \kappa^2)^2 \right]} \\
&+ \frac{[q_{\perp}^2 - q_{\parallel}^2][2D^4 \kappa^2 q^4 \mathcal{E}_{\parallel}^2 + D^4 \mathcal{E}_{\parallel}^4 q_{\parallel}^2 q^2 + D^4 \kappa^4 \mathcal{E}_{\parallel}^2 q^2]}{q^2 \left[(-\omega^2 + D^2 q^4 + D^2 q^2 \kappa^2 + D^2 q_{\parallel}^2 \mathcal{E}_{\parallel}^2)^2 + \omega^2 D^2 (2q^2 + \kappa^2)^2 \right]} \\
&+ \frac{-D^4 \kappa^2 q^4 q_{\parallel}^2 [\kappa^2 + 2q^2] + D^4 q^8 [\mathcal{E}_{\parallel}^2 - q_{\parallel}^2] + D^4 \kappa^4 q_{\parallel}^4 \mathcal{E}_{\parallel}^2 - D^4 q_{\parallel}^2 q^4 \mathcal{E}_{\parallel}^2 [q_{\parallel}^2 + 2q^2]}{q^2 \left[(-\omega^2 + D^2 q^4 + D^2 q^2 \kappa^2 + D^2 q_{\parallel}^2 \mathcal{E}_{\parallel}^2)^2 + \omega^2 D^2 (2q^2 + \kappa^2)^2 \right]} \Bigg],
\end{aligned} \quad (4.2)$$

where $q^2 = [q_{\perp}^2 + q_{\parallel}^2]$.

In deriving the expression for the current fluctuations in Chap. 2, two major factors

were considered. First, we distinguished between noise terms corresponding to positive and negative ions, and second the screening effect was included in number fluctuations $C = C^{+} + C^{-} - 2C_{\text{pore}}$.

To study the screening effect influence, we rearrange the terms in Eq. (4.2) by grouping the terms that depend on $\kappa^2 = 8\pi\ell_B C_{\text{pore}}$ in the numerator, we obtain:

$$\begin{aligned}
&\left\langle \left| \widetilde{J}_{\parallel}^{+}(\mathbf{q},\omega) - \widetilde{J}_{\parallel}^{-}(\mathbf{q},\omega) \right|^2 \right\rangle = \\
&4DC_{\text{pore}}\Bigg[1 + \frac{\omega^2[D^2\mathcal{E}_{\parallel}^2 q^2[2q_{\parallel}^2 + q^2] - D^2 q_{\parallel}^2 q^4] + [q_{\perp}^2 - q_{\parallel}^2]D^4\mathcal{E}_{\parallel}^4 q_{\parallel}^2 q^2}{q^2\left[(-\omega^2 + D^2q^4 + D^2q^2\kappa^2 + D^2q_{\parallel}^2\mathcal{E}_{\parallel}^2)^2 + \omega^2 D^2(2q^2+\kappa^2)^2\right]} \\
&+ \frac{D^4 q^8[\mathcal{E}_{\parallel}^2 - q_{\parallel}^2] - D^4 q_{\parallel}^2 q^4 \mathcal{E}_{\parallel}^2[q_{\parallel}^2 + 2q^2]}{q^2\left[(-\omega^2 + D^2q^4 + D^2q^2\kappa^2 + D^2q_{\parallel}^2\mathcal{E}_{\parallel}^2)^2 + \omega^2 D^2(2q^2+\kappa^2)^2\right]} \\
&+ \frac{\omega^2[-D^2\kappa^2 q_{\parallel}^2(\kappa^2+2q^2)] + [q_{\perp}^2 - q_{\parallel}^2][2D^4\kappa^2 q^4\mathcal{E}_{\parallel}^2 + D^4\kappa^4\mathcal{E}_{\parallel}^2 q^2]}{q^2\left[(-\omega^2 + D^2q^4 + D^2q^2\kappa^2 + D^2q_{\parallel}^2\mathcal{E}_{\parallel}^2)^2 + \omega^2 D^2(2q^2+\kappa^2)^2\right]} \\
&+ \frac{-D^4\kappa^2 q^4 q_{\parallel}^2[\kappa^2 + 2q^2] + D^4\kappa^4 q_{\parallel}^4\mathcal{E}_{\parallel}^2}{q^2\left[(-\omega^2 + D^2q^4 + D^2q^2\kappa^2 + D^2q_{\parallel}^2\mathcal{E}_{\parallel}^2)^2 + \omega^2 D^2(2q^2+\kappa^2)^2\right]}\Bigg].
\end{aligned} \tag{4.3}$$

If we reorganize the terms in the first and the second fractions of Eq. (4.3), we get:

$$\begin{aligned}
&4DC_{\text{pore}}\Bigg[\frac{\omega^2 q^2\left[D^2\mathcal{E}_{\parallel}^2[2q_{\parallel}^2 + q^2] - D^2 q_{\parallel}^2 q^2\right] + D^4\mathcal{E}_{\parallel}^2 q^4 q_{\perp}^4}{q^2\left[(-\omega^2 + D^2q^4 + D^2q^2\kappa^2 + D^2q_{\parallel}^2\mathcal{E}_{\parallel}^2)^2 + \omega^2 D^2(2q^2+\kappa^2)^2\right]} \\
&+ \frac{D^4 q_{\parallel}^2 q^2\left[\mathcal{E}_{\parallel}^4[q_{\perp}^2 - q_{\parallel}^2] - q^2[q^4 + 2\mathcal{E}_{\parallel}^2 q_{\parallel}^2]\right]}{q^2\left[(-\omega^2 + D^2q^4 + D^2q^2\kappa^2 + D^2q_{\parallel}^2\mathcal{E}_{\parallel}^2)^2 + \omega^2 D^2(2q^2+\kappa^2)^2\right]}\Bigg].
\end{aligned} \tag{4.4}$$

However, if we focus on the third and fourth fractions of Eq. (4.3), we can rewrite them as:

$$\begin{aligned}
&4DC_{\text{pore}}\Bigg[\frac{2D^2\kappa^2\left[-q_{\parallel}^2 q^2\left[\omega^2 + D^2q^4\right] + D^2 q^4\mathcal{E}_{\parallel}^2[q_{\perp}^2 - q_{\parallel}^2]\right]}{q^2\left[(-\omega^2 + D^2q^4 + D^2q^2\kappa^2 + D^2q_{\parallel}^2\mathcal{E}_{\parallel}^2)^2 + \omega^2 D^2(2q^2+\kappa^2)^2\right]} \\
&+ \frac{D^2\kappa^4[-\omega^2 q_{\parallel}^2 + D^2\mathcal{E}_{\parallel}^2 q_{\perp}^4 - D^2 q^4 q_{\parallel}^2]}{q^2\left[(-\omega^2 + D^2q^4 + D^2q^2\kappa^2 + D^2q_{\parallel}^2\mathcal{E}_{\parallel}^2)^2 + \omega^2 D^2(2q^2+\kappa^2)^2\right]}\Bigg].
\end{aligned} \tag{4.5}$$

4.3 Simplified Form

First, the order of magnitude acquired by C_{pore} in our systems does not surpass -3, hence the maximum value of κ^2 is 0.1. The diffusion coefficient is considered to have a constant

value $D = 1$ Å$^2/\tau$ and the value of the electric field $\mathcal{E}_\parallel$ varies between 0.5 and 1.1 $k_BT/\left(e\text{Å}\right)$. The first simplification could arise if the size of the pore is sufficiently small compared to the Debye length. In this case, we can apply the $\kappa \to 0$ limit that cancels Eq. (4.5) and cancels the κ dependence from Eq. (4.4) recalling the simpler expression given in equation (2.41). Therefore Equation (4.4) can be rearranged in the following simplified form independent of κ:

$$2DC_{\text{pore}}\left[\frac{2D^2\mathcal{E}_\parallel^2 q^2\left[\omega^2 + D^2q_\perp^4\right]}{\left[(-\omega^2 + D^2q^4 + D^2q_\parallel^2\mathcal{E}_\parallel^2)^2 + 4\omega^2D^2q^4\right]}\right.$$
$$\left. + \frac{2\omega^2D^2q_\parallel^2\left[2\mathcal{E}_\parallel^2 - q^2\right] + 2D^4q_\parallel^2\left[\mathcal{E}_\parallel^4[q_\perp^2 - q_\parallel^2] - q^2[q^4 + 2\mathcal{E}_\parallel^2q_\parallel^2]\right]}{\left[(-\omega^2 + D^2q^4 + D^2q_\parallel^2\mathcal{E}_\parallel^2)^2 + 4\omega^2D^2q^4\right]}\right]. \tag{4.6}$$

We see that the numerator of the second fraction of Eq. (4.6): $2D^2\omega^2q_\parallel^2[2{\mathcal{E}_\parallel}^2 - q^2] + 2D^4q_\parallel^2\left[\mathcal{E}^4(q_\perp^2 - q_\parallel^2) - q^2(q^4 + 2{\mathcal{E}_\parallel}^2q_\parallel^2)\right]$, is a collection of terms with positive and negative contributions that happen to lead to a small net quantitative contribution in the range of parameters that are relevant to our system. Following those reductions, Eq. (4.2) can take the following simplified form:

$$\langle|\widetilde{J}_\parallel^+(\mathbf{q},\omega) - \widetilde{J}_\parallel^-(\mathbf{q},\omega)|^2\rangle \approx$$
$$4DC_{\text{pore}}\left[1 + \frac{{\mathcal{E}_\parallel}^2\left[\omega^2D^2 + D^4q_\perp^4\right]\left[q_\perp^2 + q_\parallel^2\right]}{\left(D^2\left[q_\perp^2 + q_\parallel^2\right]^2 + D^2{\mathcal{E}_\parallel}^2q_\parallel^2 - \omega^2\right)^2 + 4\omega^2D^2\left(q_\perp^2 + q_\parallel^2\right)^2}\right], \tag{4.7}$$

From this analysis, we can conclude that an amplitude difference would exist between the graphs corresponding to Eqs. (4.2) and (4.7) that we can better delineate when we compare the limiting behaviours.

4.4 Limits

To verify our simplification and emphasize better the differences between both formulas, we compare the behaviour of Eqs. (4.2) and (4.7) at the lower and the upper limits excluding the

white noise represented by $4DC_{\text{pore}}$. Direct inspection shows that the two expressions exhibit the same limit as ω approaches ∞. Inversely proportional to the square of the frequency, Eqs. (4.2) and (4.7) tend to 0 on the upper limit and a decaying behaviour would be observed on a log-log scale. Regarding the lower limit illustrated by ω approaching 0, Eq. (4.2) reads:

$$\begin{aligned}&\lim_{\omega\to 0}\left\langle\left|\widetilde{J}_{\parallel}^{+}(\mathbf{q},\omega)-\widetilde{J}_{\parallel}^{-}(\mathbf{q},\omega)\right|^{2}\right\rangle=\\&2DC_{\text{pore}}\left[\frac{[q_{\perp}^{2}-q_{\parallel}^{2}][4D^{4}\kappa^{2}q^{4}\mathcal{E}_{\parallel}^{2}+2D^{4}\mathcal{E}_{\parallel}^{4}q_{\parallel}^{2}q^{2}+2D^{4}\kappa^{4}\mathcal{E}_{\parallel}^{2}q^{2}]}{q^{2}(D^{2}q^{4}+D^{2}q^{2}\kappa^{2}+D^{2}q_{\parallel}^{2}\mathcal{E}_{\parallel}^{2})^{2}}\right.\\&\left.+\frac{-2D^{4}\kappa^{2}q^{4}q_{\parallel}^{2}[\kappa^{2}+2q^{2}]+2D^{4}q^{8}[\mathcal{E}_{\parallel}^{2}-q_{\parallel}^{2}]+2D^{4}\kappa^{4}q_{\parallel}^{4}\mathcal{E}_{\parallel}^{2}-2D^{4}q_{\parallel}^{2}q^{4}\mathcal{E}_{\parallel}^{2}[q_{\parallel}^{2}+2q^{2}]}{q^{2}(D^{2}q^{4}+D^{2}q^{2}\kappa^{2}+D^{2}q_{\parallel}^{2}\mathcal{E}_{\parallel}^{2})^{2}}\right].\end{aligned}\tag{4.8}$$

However, Eq. (4.7) takes the following form at this limit:

$$\begin{aligned}\lim_{\omega\to 0}\left\langle\left|\widetilde{J}_{\parallel}^{+}(\mathbf{q},\omega)-\widetilde{J}_{\parallel}^{-}(\mathbf{q},\omega)\right|^{2}\right\rangle&=\frac{4DC_{\text{pore}}{\mathcal{E}_{\parallel}}^{2}D^{4}q_{\perp}^{4}\left[q_{\perp}^{2}+q_{\parallel}^{2}\right]}{\left(D^{2}\left[q_{\perp}^{2}+q_{\parallel}^{2}\right]^{2}+D^{2}{\mathcal{E}_{\parallel}}^{2}q_{\parallel}^{2}\right)^{2}}\\&=\frac{4DC_{\text{pore}}{\mathcal{E}_{\parallel}}^{2}D^{4}q_{\perp}^{4}q^{2}}{\left(D^{2}q^{4}+D^{2}{\mathcal{E}_{\parallel}}^{2}q_{\parallel}^{2}\right)^{2}}.\end{aligned}\tag{4.9}$$

Grouping and arranging the terms involving κ^2 in the numerator of Eq. (4.8) we get:

$$D^{4}\kappa^{4}\left[\mathcal{E}_{\parallel}^{2}q_{\perp}^{4}-q^{4}q_{\parallel}^{2}\right]+4D^{4}\kappa^{2}q^{4}\left[\mathcal{E}_{\parallel}^{2}\left[q_{\perp}^{2}-q_{\parallel}^{2}\right]-q^{2}q_{\parallel}^{2}\right].$$

Characterised by opposite signs and lower magnitude, the terms involving κ^2 in the numerator of Eq. (4.8) approximately cancel each other, hence along with the second term in the denominator they can be discarded. Their effect will be constrained to a positive magnitude shift that becomes stronger for higher values for the electric field $\mathcal{E}_{\parallel}$. Equation (4.8), therefore can be expressed as following:

$$\begin{aligned}&\lim_{\omega\to 0}\left\langle\left|\widetilde{J}_{\parallel}^{+}(\mathbf{q},\omega)-\widetilde{J}_{\parallel}^{-}(\mathbf{q},\omega)\right|^{2}\right\rangle=\\&2DC_{\text{pore}}\left[\frac{2D^{4}\mathcal{E}_{\parallel}^{4}q_{\parallel}^{2}q^{2}[q_{\perp}^{2}-q_{\parallel}^{2}]+2D^{4}q^{8}[\mathcal{E}_{\parallel}^{2}-q_{\parallel}^{2}]-2D^{4}q_{\parallel}^{2}q^{4}\mathcal{E}_{\parallel}^{2}[q_{\parallel}^{2}+2q^{2}]}{q^{2}(D^{2}q^{4}+D^{2}q_{\parallel}^{2}\mathcal{E}_{\parallel}^{2})^{2}}\right].\end{aligned}\tag{4.10}$$

Rearranging the factors of Eq. (4.10), we rewrite it as the sum of two fractions:

$$\lim_{\omega\to 0}\left\langle\left|\widetilde{J}_{\parallel}^{+}\left(\mathbf{q},\omega\right)-\widetilde{J}_{\parallel}^{-}\left(\mathbf{q},\omega\right)\right|^{2}\right\rangle= \\ 2DC_{\text{pore}}\left[\frac{2D^{4}\mathcal{E}_{\parallel}^{2}q_{\perp}^{4}q^{2}}{(D^{2}q^{4}+D^{2}q_{\parallel}^{2}\mathcal{E}_{\parallel}^{2})^{2}}+\frac{2D^{4}q_{\parallel}^{2}\left[\mathcal{E}_{\parallel}^{4}[q_{\perp}^{2}-q_{\parallel}^{2}]-q^{2}\left[q^{4}+2q_{\parallel}^{2}\mathcal{E}_{\parallel}^{2}\right]\right]}{(D^{2}q^{4}+D^{2}q_{\parallel}^{2}\mathcal{E}_{\parallel}^{2})^{2}}\right]. \tag{4.11}$$

The first term in Eq. (4.11) exactly compares to the limit concluded using the simplified version of our calculation, a feature that supports our derivation in section (4.3). Because of the order of magnitude of the terms, the second fraction in Eq. (4.11) will lead to an amplitude shift that will add to the shift produced by κ^2 terms since $\mathcal{E}_{\parallel}$ dominates the values of q^2.

This agreement allows us to assert our previous conclusion that the complicated and the simplified versions of $\left\langle\left|\widetilde{J}_{\parallel}^{+}\left(\mathbf{q},\omega\right)-\widetilde{J}_{\parallel}^{-}\left(\mathbf{q},\omega\right)\right|^{2}\right\rangle$ describe the same trend (see Fig. 4.1).

4.5 Current Fluctuations Expression

In Chap. 2, the current fluctuations $S(\omega)$ was evaluated over a confined pore with length L and radius R taking the following final form:

$$S(\omega)=\frac{1}{2\pi^{2}}\int_{\pi L^{-1}}^{\pi\Lambda^{-1}}\mathrm{d}q_{\parallel}\int_{\pi R^{-1}}^{\pi\Lambda^{-1}}q_{\perp}\mathrm{d}q_{\perp}\left|\widetilde{\mathcal{A}}(q_{\perp})\right|^{2}\left|\widetilde{\mathcal{L}}(q_{\parallel})\right|^{2}\langle|\left[\tilde{J}^{+}\left(\mathbf{q},\omega\right)-\tilde{J}^{-}\left(\mathbf{q},\omega\right)\right]|^{2}\rangle. \tag{4.12}$$

However, here we employ an alternative approach to find the expression for the current fluctuations $S'(\omega)$ using Eq. (4.7), the simplified form of the average squared Fourier-transformed current density $\left\langle\left|\widetilde{J}_{\parallel}^{+}\left(\mathbf{q},\omega\right)-\widetilde{J}_{\parallel}^{-}\left(\mathbf{q},\omega\right)\right|^{2}\right\rangle$. Instead of the pore volume, we evaluate the current power spectrum over a cross section in the infinite space, a calculation that allows us to eliminate the longitudinal integration $x_{\parallel}$.

We start by writing $I\left(t\right)$ as the integral of the current density $J_{\parallel}^{+}\left(\boldsymbol{x},t\right)-J_{\parallel}^{-}\left(\boldsymbol{x},t\right)$ at a given

position in the direction of $x_\parallel$ over the lateral surface area A of the pore.

$$\begin{aligned} S'(\omega) =& \frac{1}{T}\int_T \mathrm{d}t \int_T \mathrm{d}t'\, e^{-i\omega(t-t')} \iint_A \mathrm{d}x_{\perp 1}\mathrm{d}x_{\perp 2} \int \mathrm{d}x_\parallel \iint_A \mathrm{d}x'_{\perp 1}\mathrm{d}x'_{\perp 2} \int \mathrm{d}x'_\parallel \delta(x_\parallel)\delta(x'_\parallel) \\ & \times \langle \left[J^+_\parallel(\boldsymbol{x},t) - J^-_\parallel(\boldsymbol{x},t) \right] \left[J^+_\parallel(\boldsymbol{x}',t') - J^-_\parallel(\boldsymbol{x}',t') \right] \rangle. \end{aligned} \tag{4.13}$$

Expressing the delta functions and the current density in Eq. (4.13) in terms of their Fourier transforms, we arrive at:

$$\begin{aligned} S'(\omega) =& \frac{1}{T}\int_T \mathrm{d}t \int_T \mathrm{d}t'\, e^{-i\omega(t-t')} \iint_A \mathrm{d}x_{\perp 1}\mathrm{d}x_{\perp 2} \int \mathrm{d}x_\parallel \iint_A \mathrm{d}x'_{\perp 1}\mathrm{d}x'_{\perp 2} \int \mathrm{d}x'_\parallel \\ & \times \int \frac{\mathrm{d}q_{\perp 1}}{2\pi} \int \frac{\mathrm{d}q_{\perp 2}}{2\pi} \int \frac{\mathrm{d}q_\parallel}{2\pi}\, e^{-i(q_{\perp 1}x_{\perp 1} + q_{\perp 2}x_{\perp 2} + q_\parallel x_\parallel)} \\ & \times \int \frac{\mathrm{d}q'_{\perp 1}}{2\pi} \int \frac{\mathrm{d}q'_{\perp 2}}{2\pi} \int \frac{\mathrm{d}q'_\parallel}{2\pi}\, e^{-i(q'_{\perp 1}x'_{\perp 1} + q'_{\perp 2}x'_{\perp 2} + q'_\parallel x'_\parallel)} \\ & \times \int \frac{\mathrm{d}\omega'}{2\pi} \int \frac{\mathrm{d}\omega''}{2\pi}\, e^{i\omega' t} e^{i\omega'' t'} \int \frac{\mathrm{d}q''_\parallel}{2\pi} e^{iq''_\parallel x_\parallel} \int \frac{\mathrm{d}q'''_\parallel}{2\pi} e^{iq'''_\parallel x'_\parallel} \\ & \times \langle \left[\widetilde{J}^+_\parallel(\mathbf{q},\omega') - \widetilde{J}^-_\parallel(\mathbf{q},\omega') \right] \left[\widetilde{J}^+_\parallel(\mathbf{q}',\omega'') - \widetilde{J}^-_\parallel(\mathbf{q}',\omega'') \right] \rangle. \end{aligned} \tag{4.14}$$

Performing the integrals over ω'', $\mathbf{q}'$, $q''_\parallel$, $q'''_\parallel$, $x_\parallel$, and $x'_\parallel$, leads to:

$$\begin{aligned} S'(\omega) =& \frac{1}{T}\int_T \mathrm{d}t \int_T \mathrm{d}t'\, e^{-i\omega(t-t')} \iint_A \mathrm{d}x_{\perp 1}\mathrm{d}x_{\perp 2} \iint_A \mathrm{d}x'_{\perp 1}\mathrm{d}x'_{\perp 2} \\ & \times \int \frac{\mathrm{d}q_{\perp 1}}{2\pi} \int \frac{\mathrm{d}q_{\perp 2}}{2\pi} \int \frac{\mathrm{d}q_\parallel}{2\pi} e^{-i(q_{\perp 1}(x_{\perp 1} - x'_{\perp 1}) + q_{\perp 2}(x_{\perp 2} - x'_{\perp 2}))} \\ & \times \int \frac{\mathrm{d}\omega'}{2\pi} e^{i\omega'(t-t')} \langle | \left[\tilde{J}^+_\parallel(\mathbf{q},\omega') - \tilde{J}^-_\parallel(\mathbf{q},\omega') \right] |^2 \rangle. \end{aligned} \tag{4.15}$$

We rearrange the exponential functions and perform the integrals over t, t' and ω', which yields in the limit $T \to \infty$ to:

$$S'(\omega) = \int \frac{\mathrm{d}q_{\perp 1}}{2\pi} \int \frac{\mathrm{d}q_{\perp 2}}{2\pi} \int \frac{\mathrm{d}q_\parallel}{2\pi} \left| \widetilde{\mathcal{A}}(q_{\perp 1}, q_{\perp 2}) \right|^2 \langle | \left[\tilde{J}^+_\parallel(\mathbf{q},\omega) - \tilde{J}^-_\parallel(\mathbf{q},\omega) \right] |^2 \rangle, \tag{4.16}$$

with the Fourier-transformed area function being given by:

$$\left|\widetilde{\mathcal{A}}(q_{\perp 1}, q_{\perp 2})\right|^2 = \iint_A \mathrm{d}x_{\perp 1}\mathrm{d}x_{\perp 2}\, e^{-i(q_{\perp 1}x_{\perp 1}+q_{\perp 2}x_{\perp 2})}, \tag{4.17}$$

developed in section (2.3.5). Comparing Eq. (4.12) to Eq. (4.16), we can conclude that the limited volume system is characterised by an extra function generated from $q_{\parallel}$ dependence, that would induce a positive shift in the current power spectrum.

Following this analysis, in summary, the differences between $S(\omega)$ and $S'(\omega)$ are constrained to an amplitude shift and a very negligible shift along the frequency scale that mainly depend on the electric field applied and the ionic density inside the pore.

4.6 Comparison Using Figures

Finally, to illustrate the discrepancies between both expressions for the current fluctuations in Eqs. (4.12) and (4.16), $S(\omega)$ and $S'(\omega)$, we plot the generated spectra altering the various parameters R, C_{pore}, and $\mathcal{E}_{\parallel}$ on top of each other as shown in Fig. 4.1 (The red curve corresponds to $S(\omega)$ whereas the blue curve represents $S'(\omega)$). The properties previously concluded are clearly depicted in the generated spectra. The graph corresponding to the current power spectral density $S'(\omega)$ exhibits an expected shift along the y axis due to the discarded terms. However, both curves are always characterised by a plateau at low frequencies and a power law at high frequencies, regardless of the variations employed. Increasing the radius between $R = 6\ \Lambda$ and $R = 8\ \Lambda$ does not lead to any major variations in the power spectra except of an amplitude shift. Varying the average concentration value C_{pore} shifts both graphs by one order of magnitude.

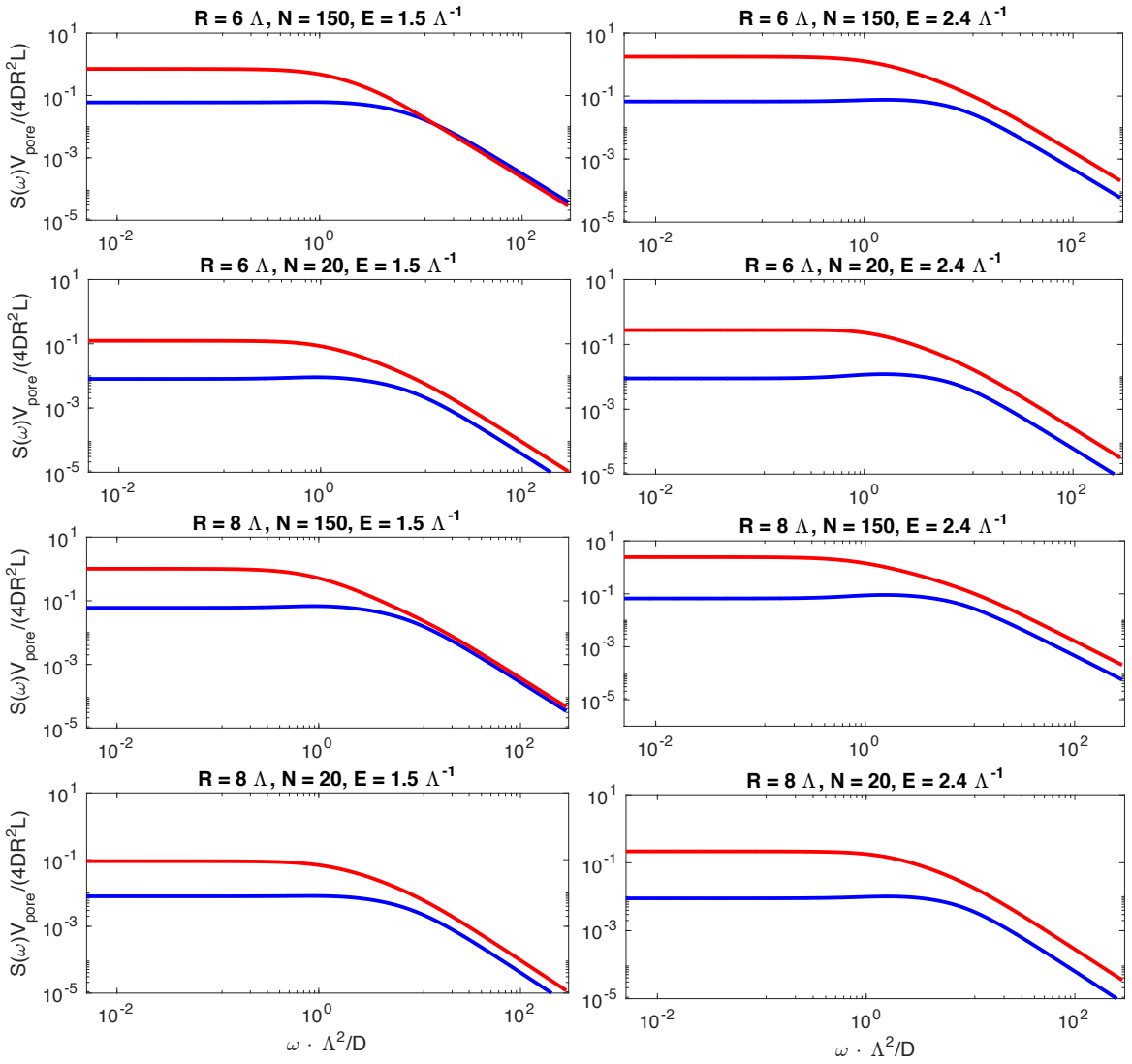

Figure 4.1: A comparison between the theoretical expression for the current fluctuations using the simplified expression for the Fourier-transform current density evaluated over a slice $S'(\omega)$ (blue curve) and the theoretical expression for the current fluctuations using the full detailed expression for the Fourier-transform current density evaluated over a the pore $S(\omega)$ (red curve). We vary the values of the average number of ions $\langle N \rangle$ inside the pore, the applied electric field $E_{\|}$, and the radius of the pore R. All graphs using both theories, show always the same behaviour combining a plateau and a power law characterised by the same exponent. In the calculation we use cut-off $\Lambda = 3$.

However, altering the electric field influences the spectra on both scales. A higher value for the electric field leads to a higher magnitude in the power spectrum and a shift in the transition frequency in both curves as detailed in our simplification. To account for the difference between $S(\omega)$ and $S'(\omega)$, we can refer to the choice of the area function.

4.6.1 Area Function

In Chap.2 (2.3.5), we have considered two expressions for the cross sectional area of the pore, the circular and the square shapes. Similarly, we need to study how the current fluctuations expression $S'(\omega)$ (Eq. (4.16)) is influenced by the area choice. Figure (4.2), shows the resulting power spectra $S'(\omega)$ using circle and square area functions. The shape of the curves appear to depend only mildly on the choice of the geometry, but the amplitudes differ by an order of magnitude with a very insignificant shift along the frequency scale. Because it is a priori not clear which area function provides the better approximation, we have the freedom to choose the appropriate function.

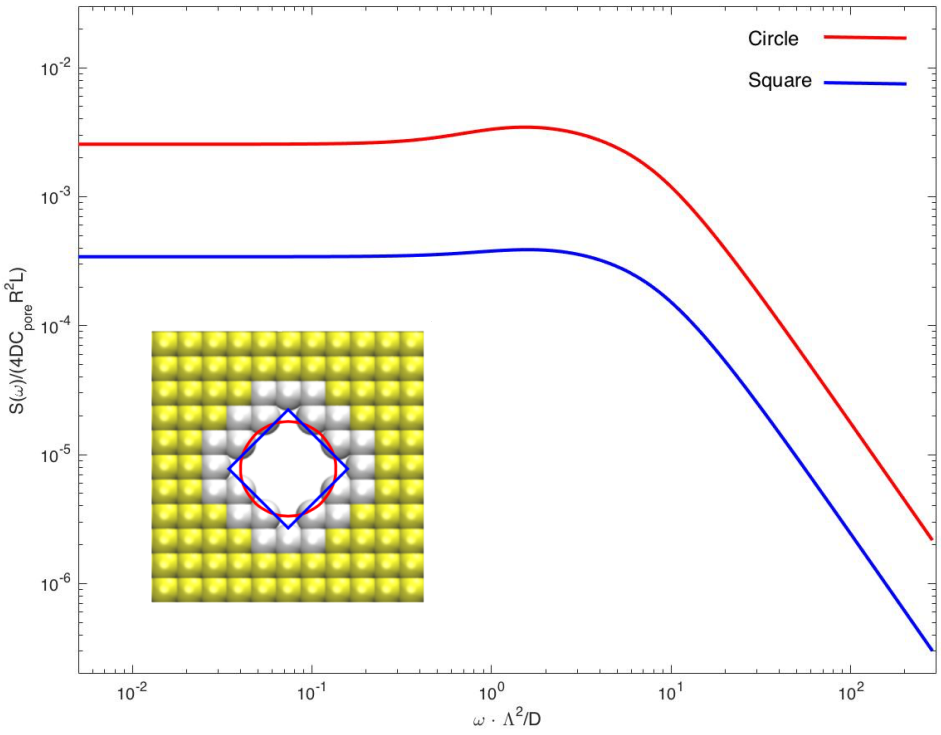

Figure 4.2: The simplified current fluctuations expression calculated according to the linearized mean field theory using two different approximations for the area function calculated in Chap.2 (Eq. (2.28) and Eq. (2.29)). The circle and the square both have the same lateral area, equal to the surface area of the particles left out of the membrane to form the pore.

4.7 Conclusion

In this chapter, we have provided a comparison between the full expression for the current fluctuations and its corresponding simplified version evaluated over a slice. The two versions showed a reasonable agreement despite the large number of terms that we did not account for in the simplified form of the average squared Fourier-transform current density. However, the flexibility in the choice of the area allows more freedom in varying the amplitude of the power spectrum.

In conclusion, both expressions $S(\omega)$ and $S'(\omega)$ can be used to fit the data generated from the simulations. However, when using $S'(\omega)$, graphs need to be rescaled to account for the amplitude difference based on the geometry chosen and the mass chosen in simulations (see Appendix (8.4) and (8.5)).

CHAPTER 5

Experimental Suggestions

Success is the sum of details.

Harvey S. Firestone (1868-1938)

5.1 Introduction

The conclusion reached in Chap. 3 stemmed from previous analysis performed on pores with different properties[2]. In the introduction, the various propositions delivered after numerous experiments trying to understand the $1/f$ noise source were highlighted[113;172;173]. Among these suggestions, we list the applied electric field, the charges on the pore wall, the valency, the pore geometry, and the gating process.

To study the effect induced by those parameters on the current fluctuations, and the role of each in generating the flicker noise at low frequencies, we vary each parameter separately and examine its effect on the power spectrum.

Again, Langevin dynamics simulations were developed to extract the current power spectral density that we fit using the linearized mean-field theory.

Power spectra generated using low ion concentrations, follow our theoretical linearized mean-

field theory supportive of the previous finding and demonstrating the dominant role of the ion-ion correlation. Adding charges across the pore wall does not induce any change in the generated spectra, similarly for the ions valency that only lead to an amplitude increase without tackling the power law. Higher or lower electric field appeared to influence the background noise, whereas fluctuations in the pore radius increases marginally the low frequency power law at high ion concentration.

5.2 Simulation

For our analysis, we use a Langevin dynamics simulation with a time step of 0.06τ (see Chap. 3). We perform simulations of 3×10^7 time steps to calculate the current $I(t) = \int_A [J_{\parallel}^{+}(\boldsymbol{x}, t) - J_{\parallel}^{-}(\boldsymbol{x}, t)]\, \mathrm{d}\boldsymbol{x}$. Again, from the current, we calculate the current power spectrum using the Welch method with a Hamming window and an overlap of 0.5 [167].

5.3 Results and Discussion

5.3.1 Radius and Ions Concentration

Although, the role of the pore radius and the concentration of ions had been thoroughly studied in Chap. 3, here we shed light on the behaviour of the power spectrum at lower concentrations and pores with smaller radii. The below analysis, constituted the stimulus for the main conclusion developed in Chap. 3. In Fig. 5.1, we show the current power spectral density $S(\omega)$, calculated from the Langevin dynamics simulations, as a function of the frequency ω (solid lines). The power spectra generated have been fitted with the linearized mean-field expression of Eq. (4.16) (dashed lines) using $\Lambda = 3$ Å, $D = 1$ Å$^2/\tau$, and C_{pore} determined from the simulations.

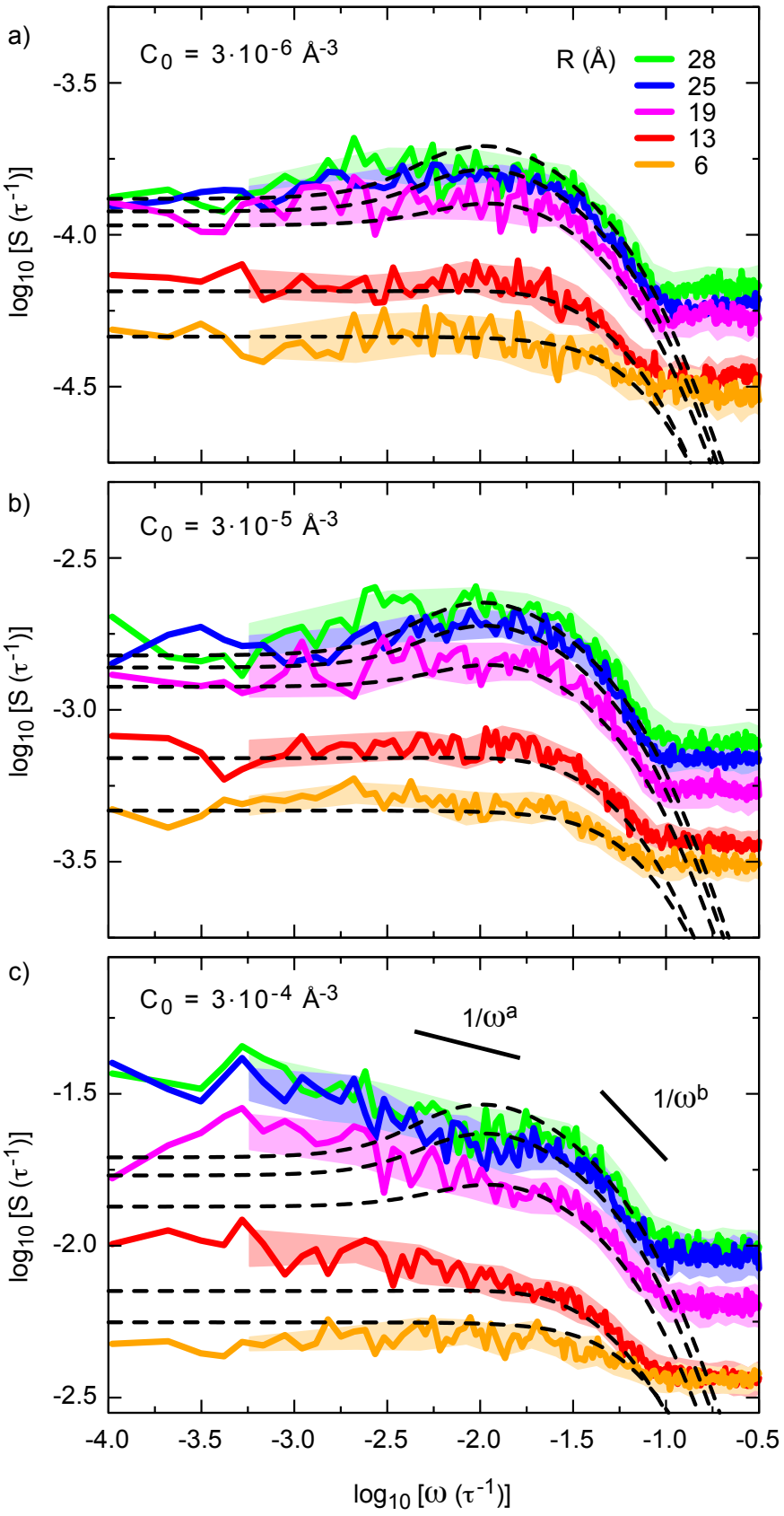

Figure 5.1: The power spectral density $S(\omega)$ of the ionic current in units of the inverse of the time scale τ, as a function of the frequency ω on a log-log scale, for ion concentrations (a) $C_0 = 3 \times 10^{-6}$ Å^{-3} (0.005 mol/l), (b) $C_0 = 3 \times 10^{-5}$ Å^{-3} (0.05 mol/l), and (c) $C_0 = 3 \times 10^{-4}$ Å^{-3} (0.5 mol/l). The solid curves denote $S(\omega)$ from simulations, block-averaged for improved clarity, and the shaded areas indicate the standard deviation of the blocks. The dashed lines denote fits to Eq. (4.16), including the adjustments (see Appendix (8.5)). The diffusion coefficient $D = 1$ Å$^2/\tau$ and the small-scale cutoff length is set to the ion size, $\Lambda = 3$ Å, for all curves. The applied electric field is $E_{\|} = 0.8\ k_B T/(e\text{Å})$.

As Fig. 5.1 indicates, all curves are characterised by a transition around $\omega = 10^{-2}\ \tau^{-1}$, and a power-law decrease $S \propto 1/\omega^b$ at high frequencies. At even higher frequencies, because of the relatively high simulation time step used, $S(\omega)$ is dominated by white background noise. The developed results show a good agreement with the developed theoretical analysis.

The power spectra generated using a high ion concentration, $C_0 = 3 \times 10^{-4}$ Å^{-3} (0.5 mol/l), shown in Fig. 5.1(c), continues to increase with decreasing frequency, following a power law $S(\omega) \propto 1/\omega^a$ that is not captured by the linearized mean-field theory spectra. Following the analysis delivered in Chap. 3, this behaviour is totally expected provoked by ion-ion correlations. However, at lower ion concentrations, $C_0 = 3 \times 10^{-6}$ Å^{-3}(0.005 mol/l) and $C_0 = 3 \times 10^{-5}$ Å^{-3} (0.05 mol/l), shown in Figs. 5.1(a-b), $S(\omega)$ exhibits a small bump around $\omega = 10^{-2}\ \tau^{-1}$ that is followed by a plateau. Remarkably, at every radius both features are captured accurately by the linearized mean-field theory. This result emphasizes more the role of ion-ion correlations in generating the power law in relation to the mean-field theory.

5.3.2 Limiting Behaviours

Previously, we have indicated that the power law at high frequencies is approximately constant for any radii larger than 19 Å, however the power law at low frequencies increases with the concentration. Those conclusions were primarily induced from Fig. 5.2. We fit the low frequency regime ($\log_{10}\omega < -1.8$) and the high frequency regime ($-1.4 < \log_{10}\omega < -1.0$) with power laws with exponents a and b respectively (see Fig. 5.1(c)). The exponent a shows a strong dependence on the ion concentration C_{pore} (Fig. 5.2(a)), except for the case $R = 6$ Å. The value of a increases from being close to or below zero for $C_{\text{pore}} < 10^{-4}$ to $0.10 < a < 0.18$ for the highest concentration.

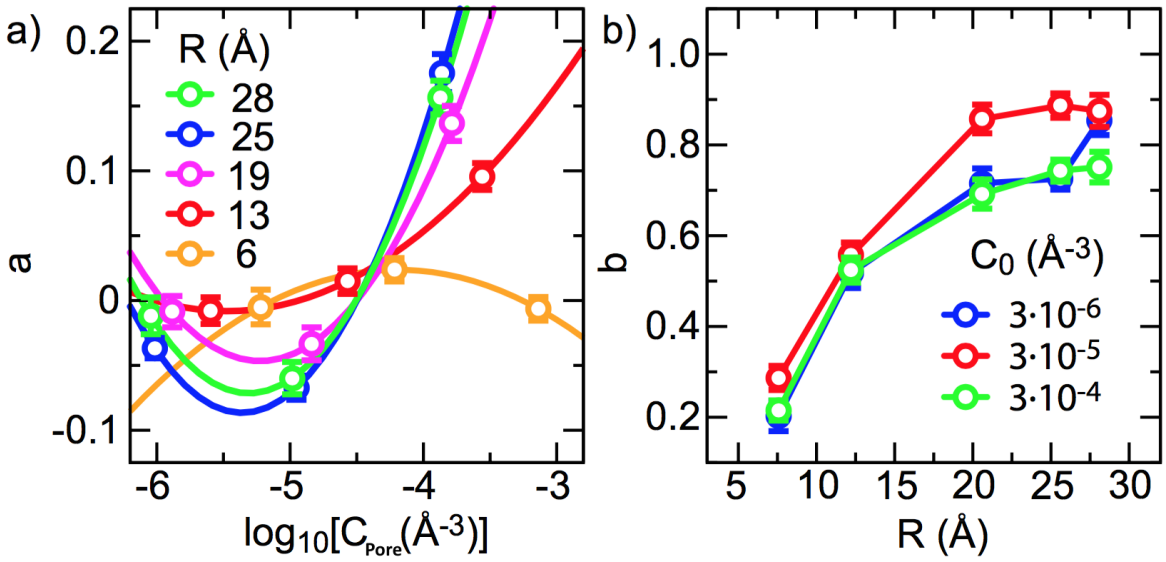

Figure 5.2: (a) The exponent a of the fits $S(\omega) \propto \omega^{-a}$ ($\log_{10}\omega < -1.8$) as a function of the concentration in the pore C_{pore}. (b) The power b of the fits $S(\omega) \propto \omega^{-b}$ ($-1.4 < \log_{10}\omega < -1.0$) as a function of the radius R. The electric field is set to $E_{\|} = 0.8\ k_BT/(e\text{Å})$.

For radii $R > 13$ Å, a becomes largely independent of R, suggesting that the power-law behaviour is an intrinsic property of non-equilibrium ion transport, rather than a consequence of the confinement. In contrast, the exponent b shows up a radius dependence for $R < 19$ Å, but is independent of the ion concentration, as predicted by Eq. (4.16) (Fig. 5.2(b)).

5.3.3 The Effect of Varying the Electric Field

The electric field in Chap. 3, appeared to play an important role in driving the ions through the pore. To highlight more its role, we perform simulations using a pore of radius $R = 25$ Å with an ion concentration of $C_0 = 3 \times 10^{-4}$ Å^{-3} (0.5 mol/l), varying the electric field from 0.3 to 1.6 $k_BT/(e\text{Å})$ (Fig. 5.3). At all electric fields applied, using a high ion concentration induces a deviation from a plateau behaviour at low frequencies. The linearized mean-field theory (dashed lines) fits the transition in the frequency domain very well for all electric fields without any adjustable parameters. We can notice that decreasing the electric field shifts the transition frequency to lower frequencies. Particularly, as expected at vanishing electric field $E_{\|}$, the noise spectrum $S(\omega)$ becomes independent of ω.

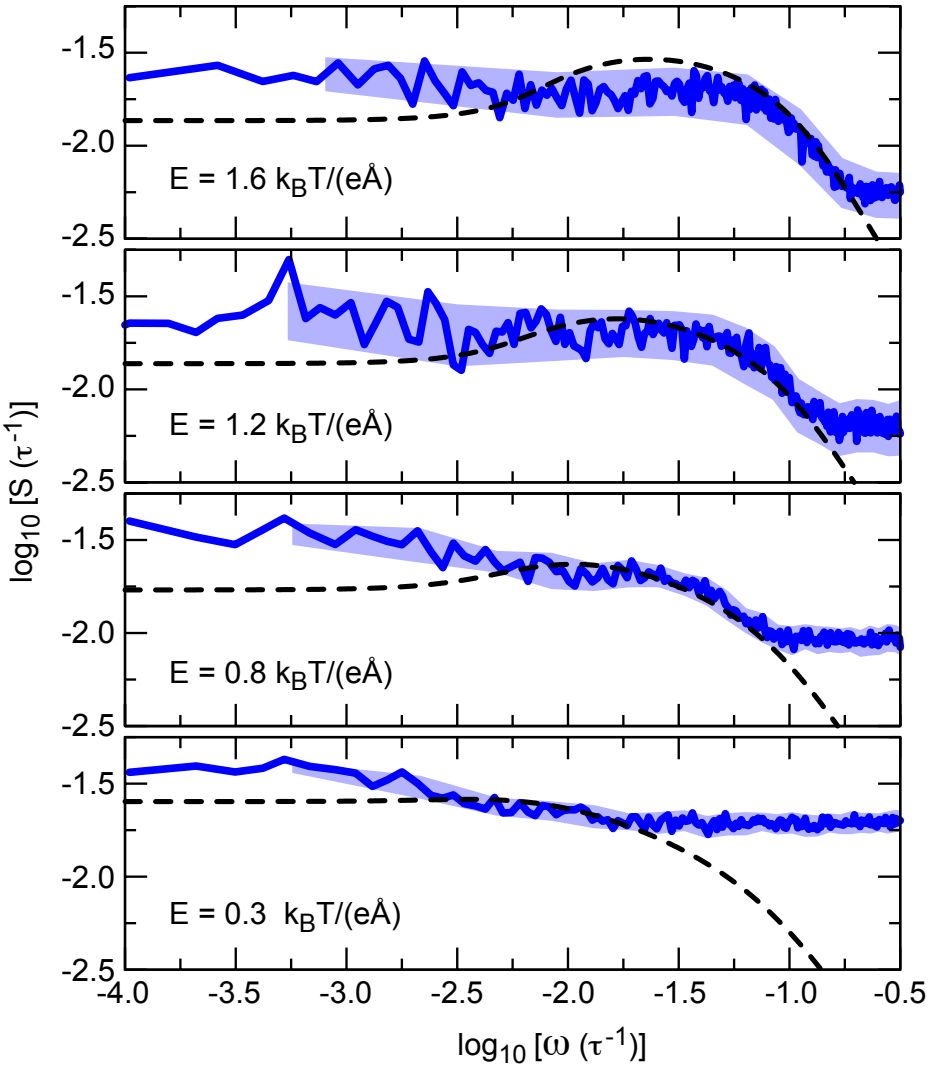

Figure 5.3: The power spectra of the ion current through a pore of $R = 25$ Å at a concentration of $C_0 = 3 \times 10^{-4}$ Å^{-3} (0.5 mol/l), at different applied electric field strengths inside the pore (0.3, 0.8, 1.2, and 1.6 $k_BT/\left(e\text{Å}\right)$). With increasing electric field strength, the transition frequency shifts upward, and the background white noise decreases.

5.3.4 Surface-Charge Role

The second factor to study its role is the surface charge. Typically, both synthetic and biological aqueous pores have a finite surface charge density. As it was suggested in several previous experiments, those charges on the membrane pore might be playing a crucial role in generating the power law $1/\omega$ at low frequencies[172;174].

To approach the validity of this assumption, we allocate negative charges on the surface of the pores, that we balance by extra positive ions in solution to maintain charge neutrality.

The charges are distributed to membrane particles positioned in a cylindrical shell between $R < x_\perp < R + 6$ Å, adding up a surface charge density of -0.3×10^{-2} $e/\text{Å}^2$. Typically, in experimental systems, surface charges come from dynamic equilibria of protonation and deprotonation of surface groups, depending heavily on the pH of the solution. In contrast, in our simulations, the surface charge is static, and we do not treat the noise that might originate in the dynamics of the chemical reactions. The corresponding power spectra are shown in Fig. 5.4.

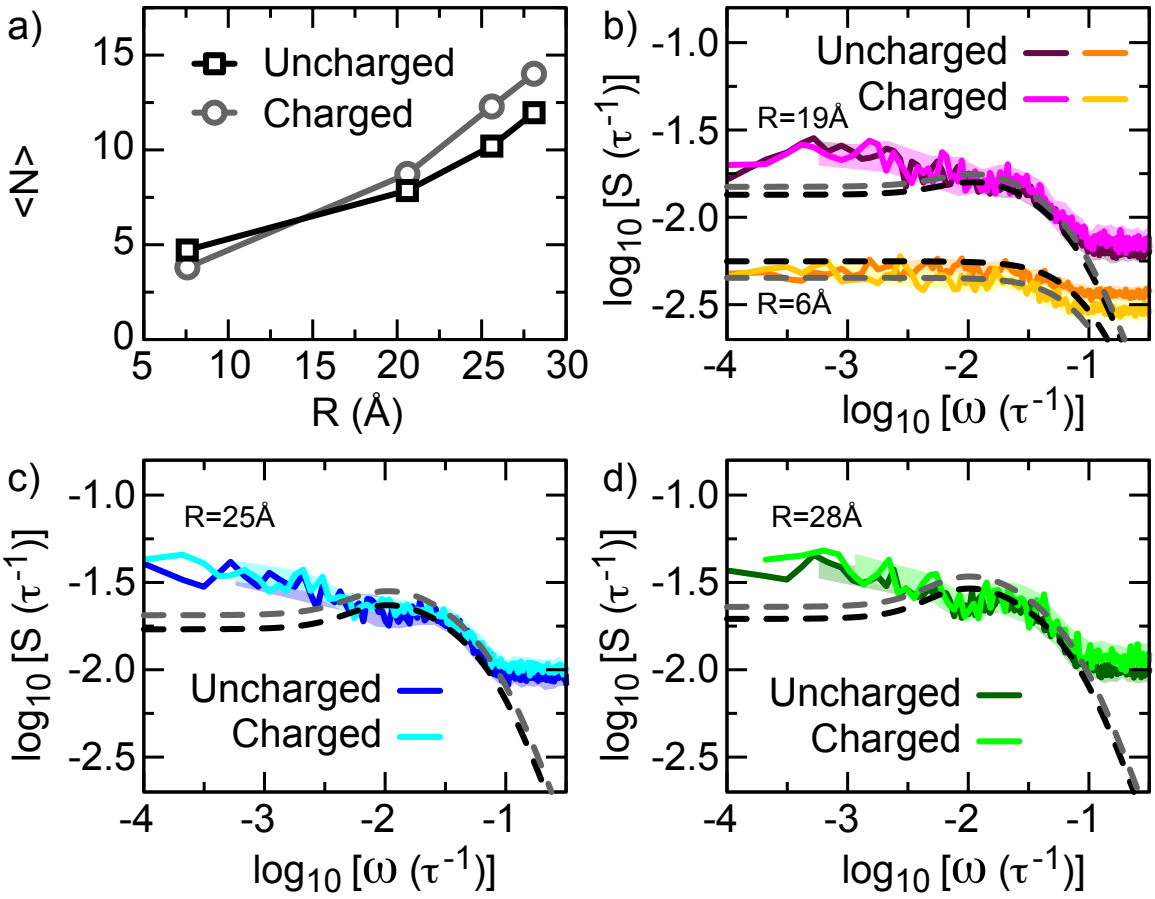

Figure 5.4: The power spectral density of the ionic current through charged and uncharged pores of radii 25 Å and 13 Å at a concentration of 3×10^{-4} Å^{-3} and an electric field of 0.8 $k_BT/(e\text{Å})$.

As we can observe, no differences are depicted in the shape, the transition frequency, or the power laws at low and high frequencies, in absolute agreement with Ref.[133]. However, the surface charge density influences the average particle numbers $\langle N \rangle$ inside the pores. Dealing

with a negatively charged surface, counterions are attracted to the interior of the charged pores, increasing the total ion concentration within a layer with a width approximately equal to the Debye length, which equals 4.4 Å in our pores. At the same time, due to the surface charge, co-ions are repelled, affecting the current passing through the pore. For pores with small radius, this results in one-way traffic for counterions. Together, these effects decrease the average particle number $\langle N \rangle$ for $R = 6$ Å, where the Debye length covers most of the pore's radius, and increases $\langle N \rangle$ for all other radii (Fig. 5.4(a)). The amplitudes of the power spectra scale accordingly (Figs. 5.4(b-d)).

5.3.5 Varying the Pore Length

Contrary to biological membrane pores characterised by an invariable length, the pore length of synthetic nanopores varies. To study the influence of this parameter, we simulate pores of different pore length L with a radius of $R = 25$ Å at a bulk concentration of $C_0 = 3 \times 10^{-4}$ Å^{-3}. As Fig. 5.5(b) shows, the power spectra of the different pore lengths converge at low frequencies. The decrease of the power spectrum in the intermediate frequency range shifts to lower frequencies with increasing L, a trend that is satisfactorily captured by the linearized mean-field theory. However, using the same set of fit parameters as used for all other curves, we could not capture the amplitude of the noise level. This difference is mainly attributed to the approximate nature of our integration over $\boldsymbol{q}$, pertaining to both the area function and the integration boundaries, which mainly influence the amplitude of the noise spectrum. Thereby, we propose two alternatives to fit the curves which have largely the same effect. Either we can adjust the amplitude of $S(\omega)$ independently, or we can vary the value of the high-wave-vector cutoff Λ as a fitting parameter. Choosing the second option for the curves in Fig. 5.5(b), the value of Λ for the integration over $q_{\parallel}$ in Eq. (4.16) has been increased by the same factor as L, to $\Lambda = 7$ Å and $\Lambda = 15$ Å respectively.

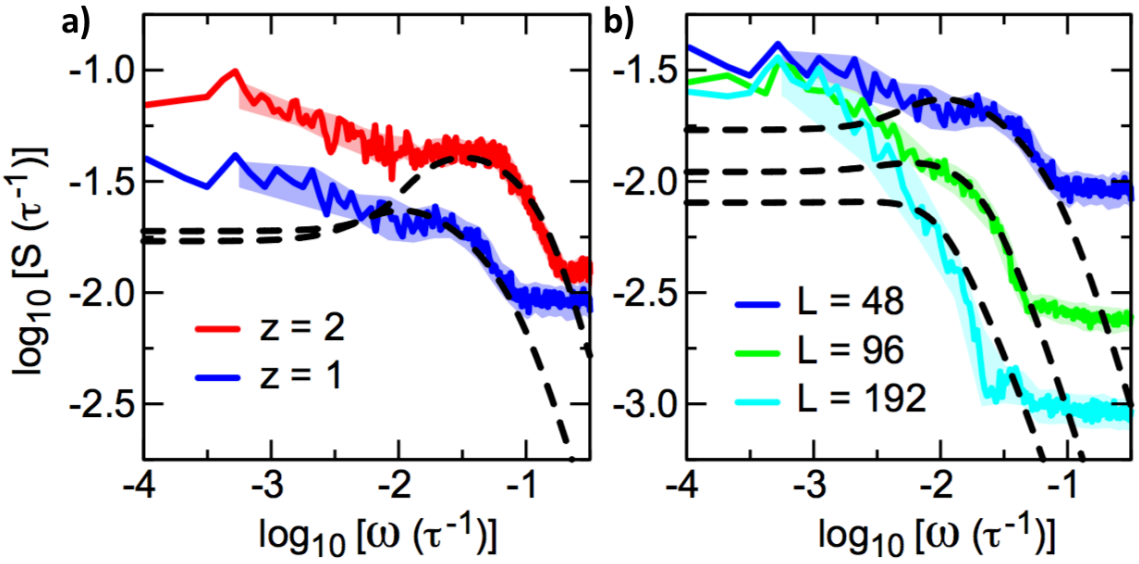

Figure 5.5: (a) The power spectra of pores with radius $R = 25$ Å and length $L = 48$ Å for two different values of the ion valency z. (b) The power spectra of pores with radius $R = 25$ Å, $z = 1$, $E_{\|} = 0.8\ k_BT/(e\text{Å})$ for different values of the pore length L. For the fitted curve, the small-scale cutoff parameter Λ for the integral over $\mathrm{d}q_{\|}$ in Eq. (4.16) has been scaled by the same factor as L.

5.3.6 Ion Valency

To accentuate more the effect of the ion correlations, we perform simulations of divalent ions at a bulk concentration of $C_0 = 3 \times 10^{-4}$ Å^{-3} in the $R = 25$ Å pore. In Fig. 5.5(a), we show the power spectral density of both the monovalent and the divalent ions. At low concentration, the exponent of the power-law scaling for divalent ions equals $a = 0.20 \pm 0.03$. Although the exponent is marginally higher than the exponent $a = 0.18 \pm 0.02$ found for the monovalent ions, the increased valency does not appear to have a large effect on the scaling of the power spectral density at low frequencies. On the other side, the effect of the ion valency on the power spectrum at high frequencies is exactly captured by the linearized mean-field theory (dashed lines).

5.4 Flexible Pores

As it was described in the introduction, experiments performed on biological pores indicated that the gating process was the major source of $1/f$ noise from[114]. In other experiments it was evoked that perturbations in the membrane shape can affect interactions between ions[175]. To study this suggestion and extend our work, we perform Langevin dynamics simulations on nanopores of approximately cylindrical but fluctuating geometry embedded in an elastic membrane.

5.5 Flexible Pore Simulations

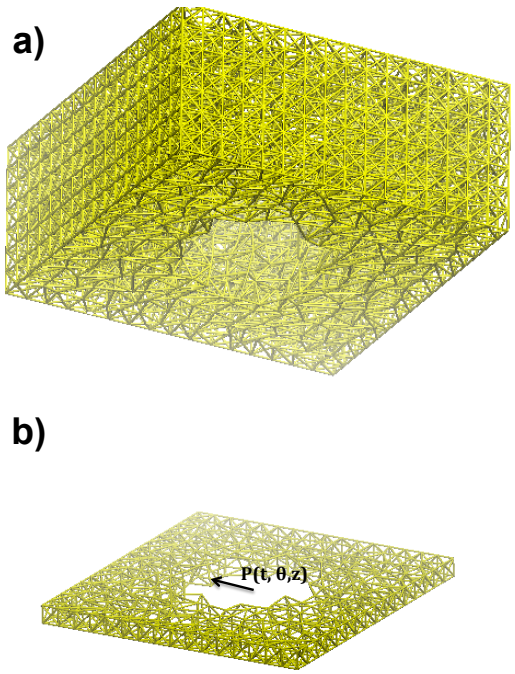

Figure 5.6: Simulation snapshots with (a) the membrane with the nanopore, (b) the cross section of the membrane with the cross-sectional area of the pore. The harmonic bonds are represented by the yellow lines connecting the particles. The ions are not shown.

Again, using Espresso we perform coarse grained molecular dynamics simulations of monovalent ions driven through a fluctuating nanopore by an external electric field[143].

An elastic membrane is modelled as a sheet of particles on a regular grid with lattice constant

$l = 6$ Å, interconnected by harmonic bonds between nearest neighbours in the axis-parallel and in-plane diagonal directions (for a total of 18 bonds per non-boundary particle). The bond potential reads:

$$V_{ij}^{bond} = \frac{k}{2}(r_{ij} - r_0)^2, \tag{5.1}$$

where $r_{ij} = |r_i - r_j|$ denotes the distance between two bonded particles and a resting bond length of $r_0 = l$ and $r_0 = \sqrt{2}l$ is chosen for axis parallel and diagonal bonds respectively so that the membrane is initialised in its equilibrium configuration. The spring constant k is varied between 0.01 $k_BT/\text{Å}^2$ and 10 $k_BT/\text{Å}^2$ and the temperature is set to 300 K[176].

We constrain the movement of the membrane to the x-y plane and we immobilise particles located within $2l$ of the box boundaries. The pore radius was given two values, $R = 13$, and 25 Å. As with fixed pores, altering the box size did not give any finite size effects.

The ion concentration at both ends of the pore was varied between $C_0 = 3\times10^{-6}, 3\times10^{-5}$, and $3 \times 10^{-4}\text{Å}^{-3}$. As in the simulations with a fixed pore, we maintain Coulomb interactions and Weeks-Chandler-Anderson interactions with $\sigma_{ij} = 3$ Å for ion-ion and membrane-membrane interactions, whereas we set $\sigma_{ij} = 6$ Å for ion-membrane interactions to avoid any permeation (Eq. (3.10)).

The electric field $\mathbf{E} = (0, 0, E_\parallel)$, applied along the pore length was set to 0.8 $\text{k}_\text{B}\text{T}/\text{eÅ}$.We maintain the simulation time scale $\tau = 5$ ps and the integration time step $\delta t = 0.06\tau$.

Interested in the current flow, we measure the particles' velocity through the membrane every 100 time steps. To produce the current power spectrum we use Welch's method with a Hamming window and an optimal segment overlap of 0.5. (Spectra shown in Fig. 5.7 and Fig. 5.8).

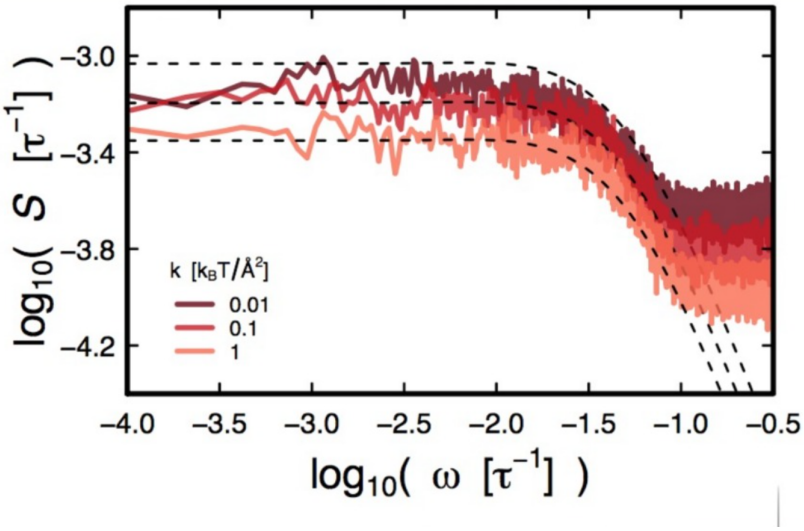

Figure 5.7: Power spectral density of the ionic current as a function of membrane elasticity using $C_0 = 3 \times 10^{-5}$ Å^{-3}, $R = 13$ Å, and $L = 48$ Å. Dashed black lines represent the fitting using the linearised mean-field theory (Eq. (4.16)).

5.5.1 Cross-Sectional Area

The vibration in the pore will induce a variation in its cross sectional area. Hence, we describe the radial distance as a function of three parameters, time, angle, and z-position along the membrane length $\rho(t, \theta, z)$. The cross sectional area $A(t, z)$ for each layer of membrane particles can be calculated using the following integral:

$$A(t,z) = \frac{1}{2}\int_{-\pi}^{\pi} \left[\, \rho(t,z,\theta) \,\right]^2 d\theta. \tag{5.2}$$

To evaluate Eq. (5.2), we use trapezoid quadrature with $N_\theta = 1000$ angular support points.

5.5.2 Membrane Elasticity

The membrane elasticity influence on the current spectrum is the next factor to be studied. Decreasing the value of the spring constant k increases the area fluctuations but only shifts the power spectrum upwards as shown in Fig. 5.7. This difference is triggered by the variation in the area that induces a concentration increase, and can only be seen when dealing with pores with small radii $R \leq 13$ Å. A plateau is seen at low frequencies, in total agreement

with the fixed pore power spectra shown in Fig. 5.1(b). Comparison to mean-field theory is clearly represented by the black dashed lines that accurately fit the simulation graphs. Results using a higher concentration are developed in the following section.

5.5.3 Power Spectra of Flexible Pores

When dealing with fixed pores, the cross-sectional area is described by a square shape equivalent to a flexible membrane with $k = 1\ k_BT/\text{Å}^2$. However, decreasing the value of k leads to an irregular cross-sectional area. This effect becomes stronger as k approaches 0 and that is mainly dependent on the pore radius. Precisely, smaller pore radius leads to stronger variation in the cross sectional area inducing more variation in the ions' current flow.

The power spectra of the ionic current obtained from the Langevin dynamics simulations using pores with radii $R = 13$ Å and $R = 25$ Å and an ion concentration $C_0 \leq 10^{-4}$ Å^{-3} are shown in Fig. 5.8. The power spectra generated did not exhibit any major difference compared to fixed pore results, two power laws at low and high frequencies are seen. The power spectrum of the flexible pore exhibits an increase in the power law and a shift in the magnitude that is provoked by the radius fluctuations. The perturbations in the radius lead to bigger cross-sectional area allowing more ions to cross the pore, hence stronger ion-ion correlations. However, the difference in the power spectrum becomes less pronounced when we increase the radius to $R = 25$ Å as shown in Fig. 5.8 (left panel). At this radius, the influence of the radius fluctuations on the cross-sectional area of the pore decreases, and the density of ions in the pore does not exhibit a remarkable variation.

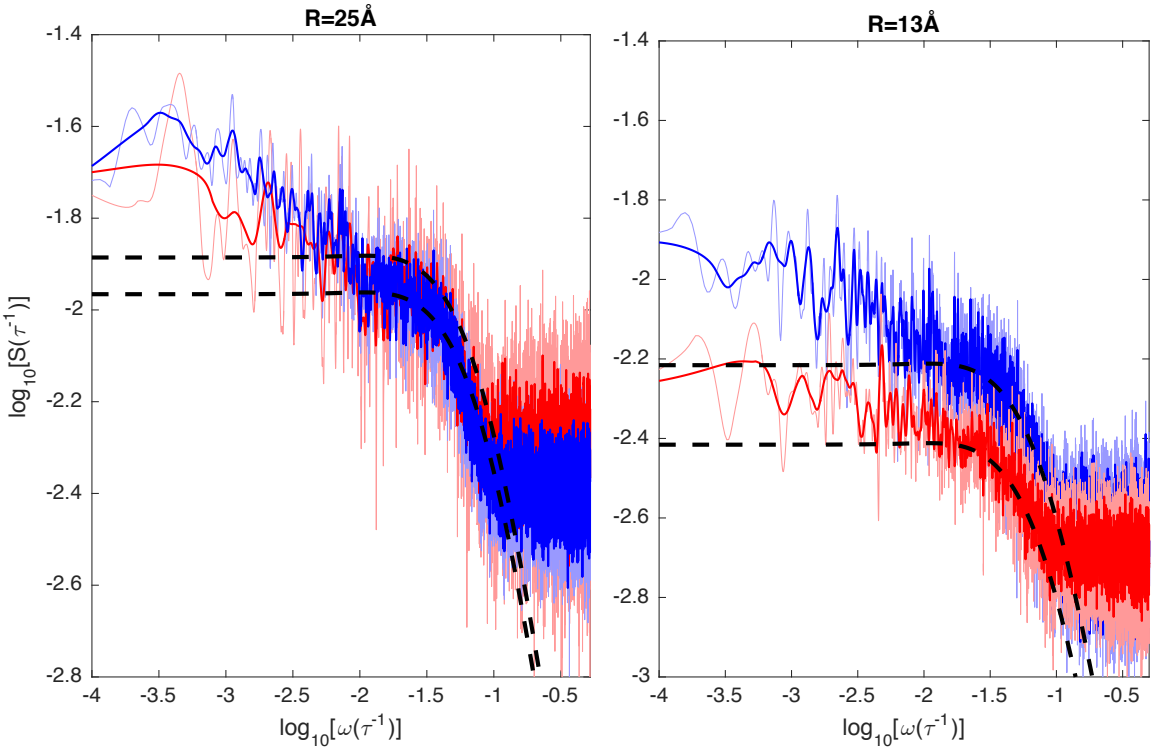

Figure 5.8: Power spectral density of the ionic current as a function of the membrane elasticity using $C_0 = 3 \times 10^{-4}$ Å^{-3}, $R = 25$ Å, $k = 0.1\ k_BT/$Å^2 and $L = 48$ Å. Dashed black lines represent the fitting using the linearised mean-field theory (Eq. (4.16)), where the small-scale cutoff length is set to the ion size, $\Lambda = 3$ Å, for all curves.

5.6 Conclusion

In this chapter, we have studied in details the influence of each parameter in our system on the power laws perceived in the current power spectral density. At low ion concentrations (0.005 mol/l - 0.05 mol/l), the Langevin dynamics simulations confirm the mean-field predictions with high accuracy, including the electric-field dependence of the power-law decrease at high frequencies and the plateau at low frequencies. Contrary to reports in literature[172;174], we find no significant dependence of the power spectrum on the surface charge density or the gating process. Fluctuations in the pore cross-sectional area initiate a higher ionic density inside the pore that at high ion concentration induce a higher power law at low frequencies. Pores with relatively small radii are the most affected by the flexibility of the pore.

CHAPTER 6

The effects of electrostatic and hydrodynamic interactions

Hydrodynamics procreated complex analysis, partial differential equations, Lie groups and algebra theory, cosmology theory and scientific computing.

Vladimir Arnold (1937-2010)

6.1 Introduction

An ultimate question following our analysis would be about the role of hydrodynamics that would be expected to have a major role on the ions' flow. Hydrodynamic interactions have a strong influence on the dynamics of Brownian particles suspended in a solvent, producing self-organized states, nonlinear dynamics, and synchronization[177–180]. To investigate this impact and answer those queries, we attempted to add hydrodynamic effects on the ions in the pore. Hydrodynamic interactions between objects decay slowly. Their strength in bulk is inversely proportional to the distance between the particles, analogous to the electrostatic potential.

The effects of hydrodynamic interactions are extremely sensitive to geometric confinement.

In a fluid between stationary confining walls, density perturbations give rise to a long-time tail in the velocity autocorrelation function of colloidal particles[181]. Conjointly, through experiments, Misiunas et al. have shown that hydrodynamic interactions become independent of the distance between particles inside small pores[182]. Ergo, these hydrodynamic effects are considered to have a discernible effect on the dynamics of larger molecules, such as DNA translocating through a nanopore[183;184]. Whereas the role of hydrodynamic interactions on colloidal particles and polymer dynamics has intrigued lot of attention and researches over the past decades, the effect of hydrodynamic interactions on ion flow remains mostly unexplored. In addition to experimental measurement and analysis, we have thoroughly shown in this thesis that molecular modeling of the power spectral density presents a promising technique to study ion motion in unprecedented detail[2;134].

In previous chapters, we showed that ion correlations at high particle density produce a power-law spectrum at low frequencies, with an exponent depending on the ion density[2]. Due to the ubiquity of the power law, and the tremendous number of experiments to explore its molecular origin, exploring the hydrodynamics role emerges as another major factor to study. Theoretical analysis of the power spectrum including the multi-body interactions between the ions and the effect of hydrodynamics remains challenging. Although hydrodynamic interactions are usually present in experimental studies, their effects on the frequency dependence of the power spectral density remain uncharted. However, with the recent advances of fast and versatile molecular simulation techniques, systematic computational investigations are now achievable and this problem can be tackled.

In this chapter, we show that whereas an increase in the ion density evoke a power-law behaviour in the power spectrum at low frequencies, introducing hydrodynamic interactions by increasing the solvent density does not have the same effect.

6.2 Hydrodynamics in Simulations

To understand the effect of hydrodynamic interactions, we use Langevin dynamics simulation of the ionic current through a nanometer-scale pore filled with an electrolyte, using the Espresso molecular dynamics package used in our previous analysis[143]. In our model, we use a mixture of ions and explicit solvent for which we use a coarse-grained description of neutral, nonpolar Lennard-Jones particles. In the simulations detailed below, we not only vary the ionic density but also the solvent particle density to give a better insight on the role of hydrodynamic interactions. Subsequently, we calculate the power spectral density of the ionic current that we compare to the power spectra generated in Chap. 5 without solvent and with the linearized mean-field theory of ions' current without hydrodynamic interactions developed in Chaps. 2 and 4.

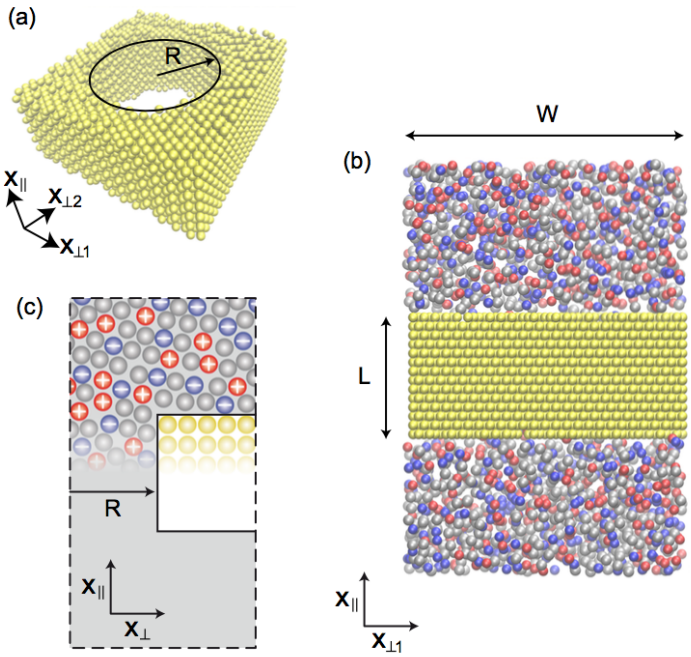

Figure 6.1: (a) Simulation snapshot of the membrane with the pore of radius R. Ions and solvent are not shown. (b) Side view of the simulation box with ions shown in blue and red, and solvent particles in grey. (c) Schematic drawing of the nanopore, with either $x_\perp^2 = x_{\perp 1}^2 + x_{\perp 2}^2$ (cylindrical coordinates) or $x_\perp = x_{\perp 1} = x_{\perp 2}$ (cartesian coordinates).

6.3 Simulation Details

Using the simulation package Espresso[143], we set up three-dimensional Langevin dynamics simulations of ion channels. We model the electrolyte by monovalent positive and negative ions, added to neutral solvent particles (Fig. 6.1). The Langevin equation for particle i is expressed as:

$$m_i \frac{d\mathbf{u}_i}{dt} = -\sum_{j \neq i} \boldsymbol{\nabla} V_{ij} + \mathbf{F}_i - \gamma \mathbf{u}_i + \boldsymbol{\zeta}_i, \tag{6.1}$$

where $\boldsymbol{\zeta}_i$ corresponds to the random force satisfying:

$$\begin{aligned} &\langle \boldsymbol{\zeta}_i(t) \boldsymbol{\zeta}_j(t') \rangle = 6 k_B T \gamma \delta_{ij} \delta(t - t'), \\ &\langle \boldsymbol{\zeta}_i(t) \rangle = 0. \end{aligned} \tag{6.2}$$

The particle i velocity is denoted by $\mathbf{u}_i$ and $m_i = 1 k_B T \tau^2 / \text{Å}^2$ denotes its corresponding mass. $\mathbf{F}_i$ is an external force applied to the particle, $k_B T$ accounts for the thermal energy, and the friction coefficient γ equals $1 k_B T \tau / \text{Å}^2$. By using an equal and arbitrary mass for all particles, m_i is incorporated in the time scale τ. We model excluded volume and van der Waals interactions between all bead pairs using a Weeks-Chandler-Andersen (shifted Lennard-Jones) potential $V_{ij}(r_{ij})$:

$$V_{ij} = l_B k_B T \frac{Q_i Q_j}{r_{ij}} + 4\epsilon_{ij} \Big[\big(\frac{\sigma_{ij}}{r_{ij}}\big)^{12} - \frac{\sigma_{ij}}{r_{ij}}\big)^{6} \Big] + \epsilon_{ij}, \tag{6.3}$$

where σ_{ij} denotes the distance between particles i and j, Q_i is the charge of particle i in units of the elementary charge e, and ϵ_{ij} represents the interaction strength. The Bjerrum length l_B equals $e^2/(4\epsilon\epsilon_0 k_B T)$, and r_{ij} is the distance between any pair of particles.

To decrease the calculation costs, the repulsive Lennard-Jones interaction is truncated at

$r_{ij} = 2^{1/6}\sigma_{ij}$ for all combinations of i and j. Ions crossing the pore experience an electric field that we represent by a force applied inside the pore in the direction along the length L of the pore $x_{\|}$ (Fig. 6.1). We vary the electric field between $E_{\|} = 0.3$ and 1.6 $k_BT/(e\text{Å})$ and we express it as:

$$\mathbf{F_i} = \begin{cases} Q_i E_{\|} & \text{if} \quad 0\langle x_{\|} \langle L, \\ 0 & \text{otherwise.} \end{cases} \tag{6.4}$$

In our simulations, we build a cylindrical nanopore with a radius ranging from 19 Å to 30 Å, permeating a rigid membrane. We set the membrane width to $W = 96$ Å and its length to $L = 48$ Å (Fig. 6.1). The solvent density is increased from $C_s = 5.5 \times 10^{-4}$ Å^{-3} to 2.1×10^{-3} Å^{-3} and 5.5×10^{-3} Å^{-3}, which are all below the bulk freezing density of the Weeks-Chandler-Andersen fluid model. All the boundary and initial conditions developed in Chap. 3 (3.3) are also employed in the following simulations.

6.3.1 Anti-Freeze Water Molecules

Compared to the molecular density of water, the maximum density corresponds to a coarse-grained force field where each particle represents approximately 6 water molecules. A smooth surface introduces a crystalline order in the fluid, over a range that depends on the molecular properties of the liquid[185–187]. In a fluid consisting of identical Lennard-Jones spheres, the crystalline order spreads over a distance larger than our simulation box, leading to a crystallization of the Lennard-Jones fluid. To prevent this contingency, we break the uniformity of the membrane surface by randomly removing half of the particles from the outer layer as shown in Fig. 6.1(a). As represented in Fig. 6.2, the solvent particles interact with the ions through L-J potential whereas ions interact among themselves through Coulomb interactions and L-J. As in our previous analysis, the membrane particles are frozen, and for the membrane-ion, membrane-solvent, ion-solvent, ion-ion and solvent-solvent interactions

we use $\epsilon_{ij} = 2\ k_B T$ and $\sigma_{ij} = 4.7$ Å[185]. For the membrane and solvent particles we use $Q_i = 0$, and for the ions we use $Q_i = \pm 1$. We use an increasing electrolyte density of $C_i = \{5.5 \times 10^{-5},\quad 5.5 \times 10^{-4},\quad 1.0 \times 10^{-3},\quad 2.1 \times 10^{-3}\}$ Å^{-3}.

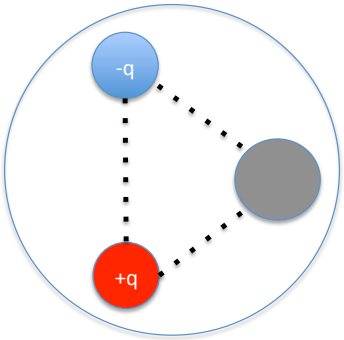

Figure 6.2: The solvent(represented in grey)-ion and ion-ion interactions within the van der Waals radius of the solvent particle.

6.3.2 Particle Diffusion

When the surrounding solvent is perturbed by the motion of the particle i, the hydrodynamic signal diffuses at a rate governed by the kinematic viscosity ν. Only when this viscous momentum diffuses at a much faster rate than the particle itself, hydrodynamic interactions occur. The corresponding relation is governed by the Schmidt number $Sc = \nu/D$, where D accounts for the diffusion coefficient of the solvent particles.

In the strongly confined environment of the nanopore, we need to verify that the coarse-grained solvent particles produce hydrodynamic interactions. For this purpose, we simulate a pressure difference across the length of the channel by applying a constant force to all particles inside a pore filled with pure solvent. We calculate the fluid velocity as a function of the radial coordinate, and we average it across the length of the channel:

$$u_{\parallel} = \frac{-F_{\parallel}}{4m_i\nu}\left[R^2 + 2bR - x_{\perp}^2\right]. \tag{6.5}$$

The flow of ions in a slit-like cylindrical channel forms a Hagen-Poiseuille flow profile with a finite slip length b. Precisely, R refers to the pore radius and the pressure gradient across the

length of the pore, is represented by $F_{\|}C_s = \nabla_{\|}p$. In our case, it is derived from the uniform applied force $F_{\|} = 0.8\ k_BT/\text{Å}$ on the solvent particles inside the pore characterised by a mass $m_i = 1\ k_BT\tau^2\text{Å}^2$ and number density C_s. The velocity profile for the lowest solvent density $C_s = 5.5 \times 10^4\ \text{Å}^{-3}$ is shown in Fig. 6.3(a). The fit shown by the blue line using Eq. (6.5) yields $\nu = 900\ \text{Å}^2/\tau$, which in combination with $D = 1\ \text{Å}^2/\tau$ leads $Sc = 900$. Therefore, we can conclude that all our simulations satisfy the conditions for hydrodynamic interactions since the Schmidt number at higher solvent densities is even higher,

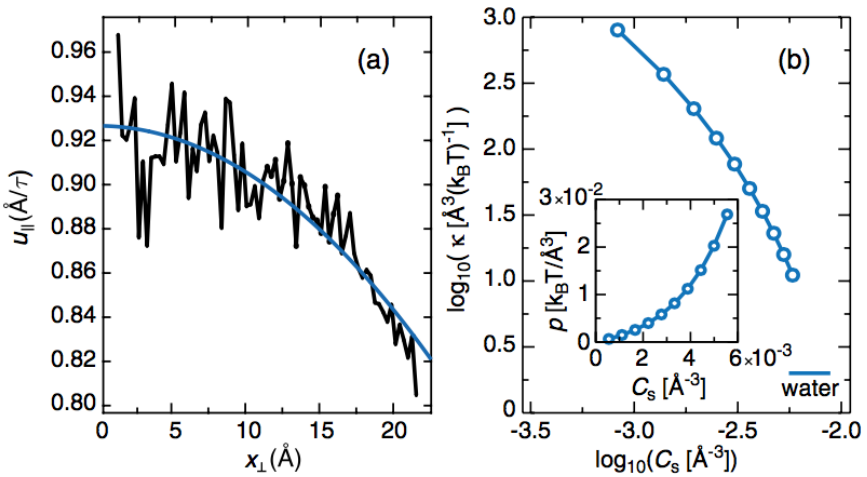

Figure 6.3: (a) The connected black dots represent the tangential flow velocity $u_{\|}$ as a function of the radial position $x_\perp$ in response to an applied pressure gradient, and the solid blue line is the fitted Poiseuille flow profile (Eq. (6.5)). (b) The bulk compressibility κ as a function of the solvent concentration C_s. The experimental compressibility of water at room temperature is shown as a reference. The inset shows the pressure p as a function of C_s.

6.3.3 Hydrodynamics Interactions

Not only propagating by viscous momentum diffusion, hydrodynamic interactions are also transmitted by sound wave propagation. The sound velocity in an incompressible fluid is infinite, and the viscous momentum diffusion is solely responsible for the time evolution of the hydrodynamic interactions.

The compressibility of our model solvent is finite, however, depending on the solvent density C_s, which might have implications for the hydrodynamic interactions[188]. To check this assumption, using $\kappa_T = (\text{dln}(\text{C}_\text{s})/\text{d}p)_T$, where p is the pressure, we calculate the isothermal

compressibility from the graph featuring the pressure p as a function of solvent density C_s in separate bulk simulations see Fig. 6.3(b).

As we alter the solvent density, we vary the compressibility over two orders of magnitude. Nevertheless, the compressibility of water is still a factor 5 below the compressibility of our highest-density solution, equal to $\kappa_T = 2$ Å$^3/(k_BT)$. Next we calculate the sound velocity $u_s = \gamma/(m_i C_s \kappa_T)$ to quantify the effect of the compressibility, where γ is the heat capacity ratio, which, in a liquid is of order $\gamma \approx 1$.

The sound velocity increases drastically by a factor of 80 as we change the solvent density in our simulations. It varies from $u_s = 3$ Å$/\tau$ at the lowest density to $u_s = 239$ Å$/\tau$ at the highest density. Thereby, we use the Mach number $Ma = \sqrt{k_BT/m_i}/u_s$ to estimate the importance of the compressibility effects, where we adapt the estimate of the thermal velocity k_BT/m_i as the typical velocity of the particles.

As the value of Ma is well below 1 in all our simulations, the compressibility is not expected to have a large effect on the hydrodynamic properties[188].

In the Langevin dynamics simulations, the stochastic force $\boldsymbol{\xi}$ provides a truncation length beyond which it exceeds the force due to hydrodynamic interactions[188]. Because the truncation length of $\boldsymbol{\xi}$ depends on the magnitude of the force from which the hydrodynamic interactions originate, quantification is considered complicated. However, a part of the long-ranged hydrodynamic interactions will be preserved as the interparticle forces in the system reach considerably high values.

6.4 Results

6.4.1 Ions and Solvent Concentrations

We use three different solvent concentrations C_s in simulations to calculate the power spectral density of the ionic current. The resulting power spectra are shown in Fig. 6.4.

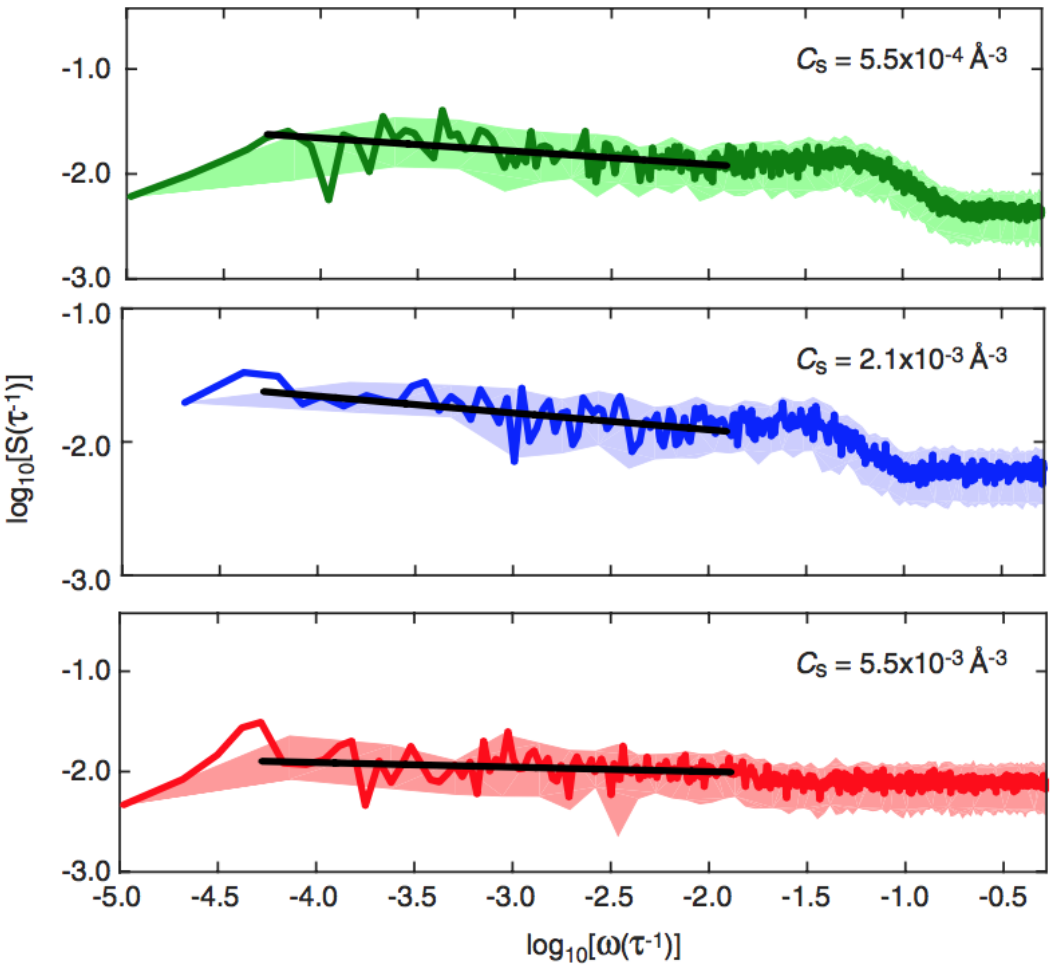

Figure 6.4: The power spectra of the ionic current through pores with different solvent densities C_s in units of the inverse time scale τ^{-1}. Solid black lines indicate the fit with $S \approx 1/\omega^{\alpha}$. We use a fixed ion concentration $C_i = 5.5 \times 10^{-4}$ Å^{-3} , radius $R = 25$ Å and an applied electric field $E_{\|} = 1.6\ k_B T/(e\text{Å})$.

At low solvent density, the curves exhibit a transition around $\omega = 0.1\ \tau^{-1}$, similar to the implicit solvent case[2]. With increasing solvent density, the transition becomes less pronounced due to an increase in the high-frequency noise level. Surprisingly, increasing the solvent density did not alter the power spectral density at low frequencies, even for a tenfold increase in solvent density. As it was described in Chaps. 3 and 5, ion concentration was the major factor that triggered the discovery of the ion-correlations role in generating the power law at low frequencies. Below, we will examine the effect of increasing ion concentration on the power spectral density in the presence of solvent particles (Fig. 6.5).

From Fig. 6.5, we notice a higher noise amplitude at higher ion concentration, and a shift in the transition frequency. However, once more a new behaviour is depicted at lower frequencies. The power spectral density exhibits a power law, with an exponent that increases sharply with increasing ion concentration. Those results recall the results found in simulations with implicit solvent in Chaps. 3 and 5[2]. Furthermore as the curves in Fig. 6.5 indicates, higher ion concentration leads to a continuous increase in the exponent of the power law, reaching $a = 0.4$ at an ion concentration of $C_i = 2 \times 10^{-3}$ Å^{-3}.

6.4.2 Hydrodynamics Interactions Role

To test the effect of the hydrodynamic interactions and to check the applicability of the mean-field theory in the presence of solvent, we fit the linearized mean-field theory to our simulation results (Fig. 6.5). Although in our mean-field theory derivation we did not include hydrodynamic interactions, the simulated curves are well described by the implicit-solvent model at high frequencies, and the expected disvergence is seen at low frequencies. As discussed earlier, the ion-ion correlations are the source of the power-law at low frequencies, hence the discordance between theory plot and simulations results (Chaps. 3 and 5)[2]. Remarkably, it is not necessary to take hydrodynamic interactions into account to describe the power spectrum of the ionic current through an electrolyte-filled pore.

6.4.3 Limiting Behaviours and Charged Particles

At low frequencies, we fit the exponent a of the power law $S(\omega) \sim \omega^{-\alpha}$ for the curves shown in Figs. 6.4 and 6.5. We fit the noise spectra for $\log_{10}(\omega) < -1.8$ and discard the lowest frequency data points because of their statistical uncertainty. The exponent is shown in Fig. 6.6 as a function of ion concentration C_i for fixed solvent concentration (top panel) and as a function of solvent concentration C_s at fixed ion concentration (bottom panel). As we can notice from Fig. 6.5, whereas the exponent increases sharply as a function of the ion density,

increasing the solvent concentration has no effect.

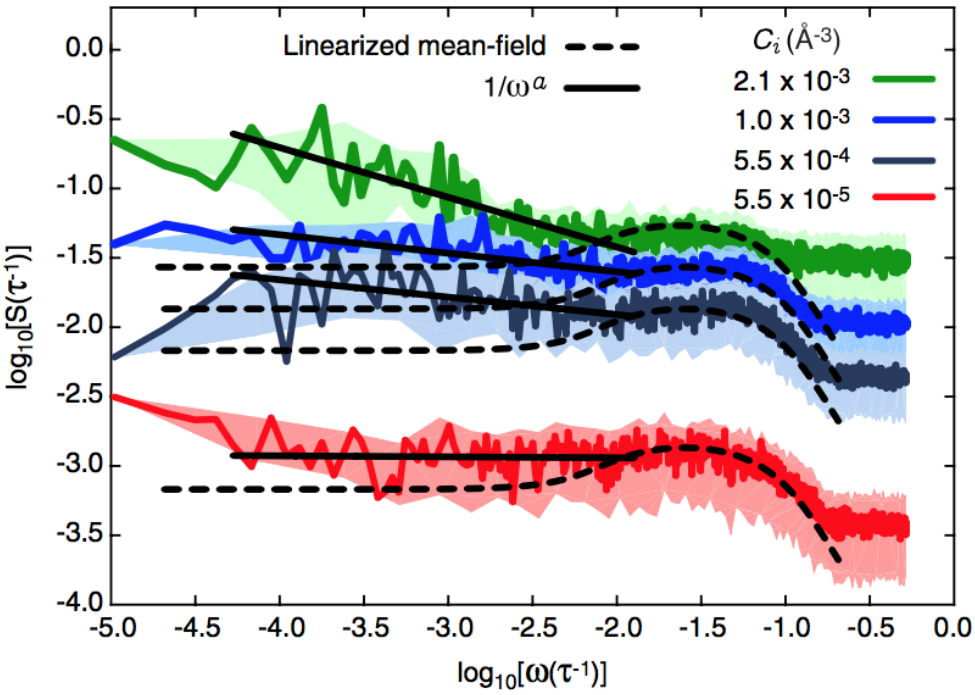

Figure 6.5: The power spectral density $S(\omega)$ of the ionic current in units of the inverse of the time scale τ , as a function of the frequency ω on a log-log scale, for different ion concentration C_i , in combination with a solvent density of $C_s = 5.5 \times 10^{-4}$ Å^{-3}. The solid colored lines show the simulation results and the shaded region represents the standard deviation that we get when applying a block-averaging method to improve the readability. The dashed lines represent the fits derived from the linearized mean field theory, with parameters taken from the simulations: applied electric field $E_{\|} = 1.6\ k_BT/(e\text{Å})$, pore radius $R = 25$ Å, diffusion coefficient $D = 1$ Å$^2/\tau$, and the small-scale cutoff length is set to a value of the order of the ion size, $\delta = 2.5$ Å, for all curves (Eq. (4.16)). The solid black lines indicate the fit to $S \approx 1/\omega^a$.

Because the charge is the only difference between an ion and a solvent particle, we conclude that electrostatic interactions cause the increasing exponent. Hydrodynamic interactions, despite having a similar long-ranged spatial dependence, do not have the same effect. We perform an extra simulation without solvent particles ($C_s = 0$), and compare the power spectra of simulations with and without explicit solvent directly in Fig. 6.7. Clearly, the curves have the same frequency dependence over the entire frequency range, confirming the results of the preceding sections.

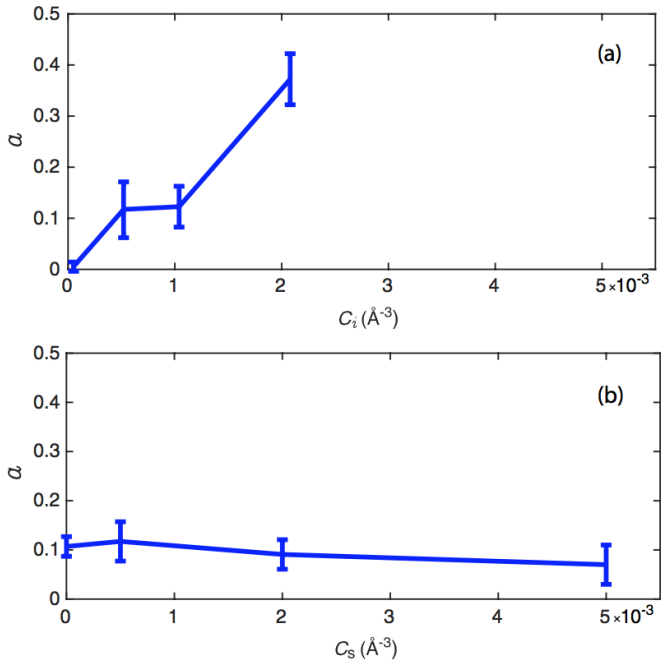

Figure 6.6: (a) The exponent a of the fits of Fig. 6.5 as a function of ion concentration with fixed solvent concentration, that shows a sharp increase with ion concentration. (b) The exponent a of the fits of Fig. 6.4 as a function of solvent concentration, with fixed ion concentration.

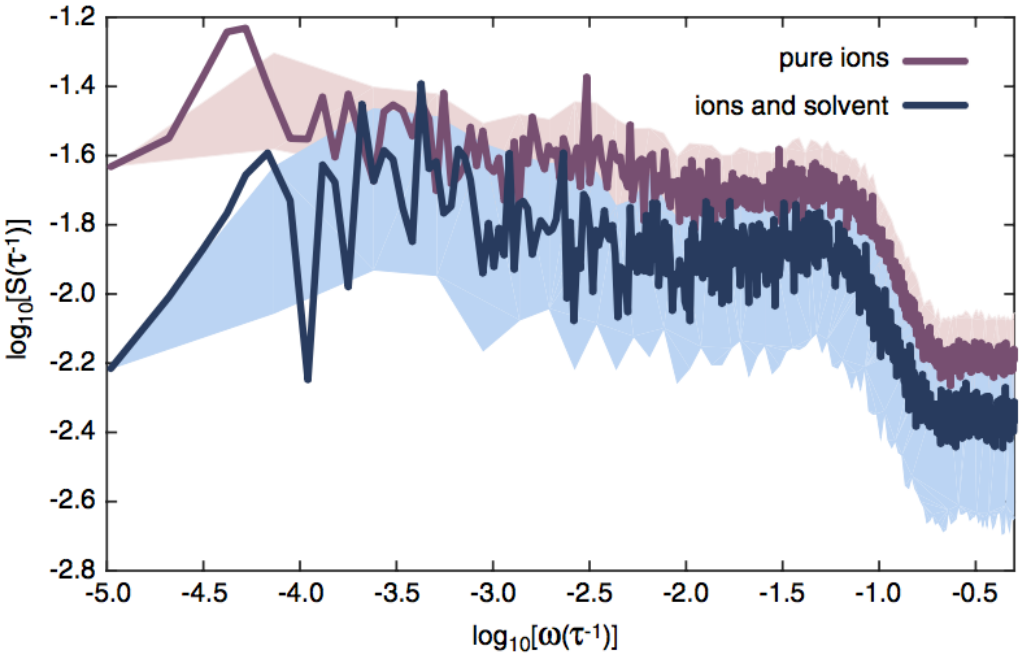

Figure 6.7: The power spectral density $S(\omega)$ of the current through a pore ($R = 25$ Å) filled with only ions ($C_i = 5.5 \times 10^{-4}$ Å^{-3}, implicit solvent) and with ions and explicit solvent ($C_i = C_s = 5.5 \times 10^{-4}$ Å^{-3}). The electric field is set to $E_{\|} = 1.6\ k_BT/(e\text{Å})$.

6.4.4 Pore Radius

Finally, we study the dependence of the power spectral density on the pore radius R and the applied electric field $E_{\|}$. In Fig. 6.8, we show once more that the linearized mean-field-theory developed in Chap. 4 captures the dependence on the pore radius and the electric field without further fit parameters, for all values of R and $E_{\|}$ studied.

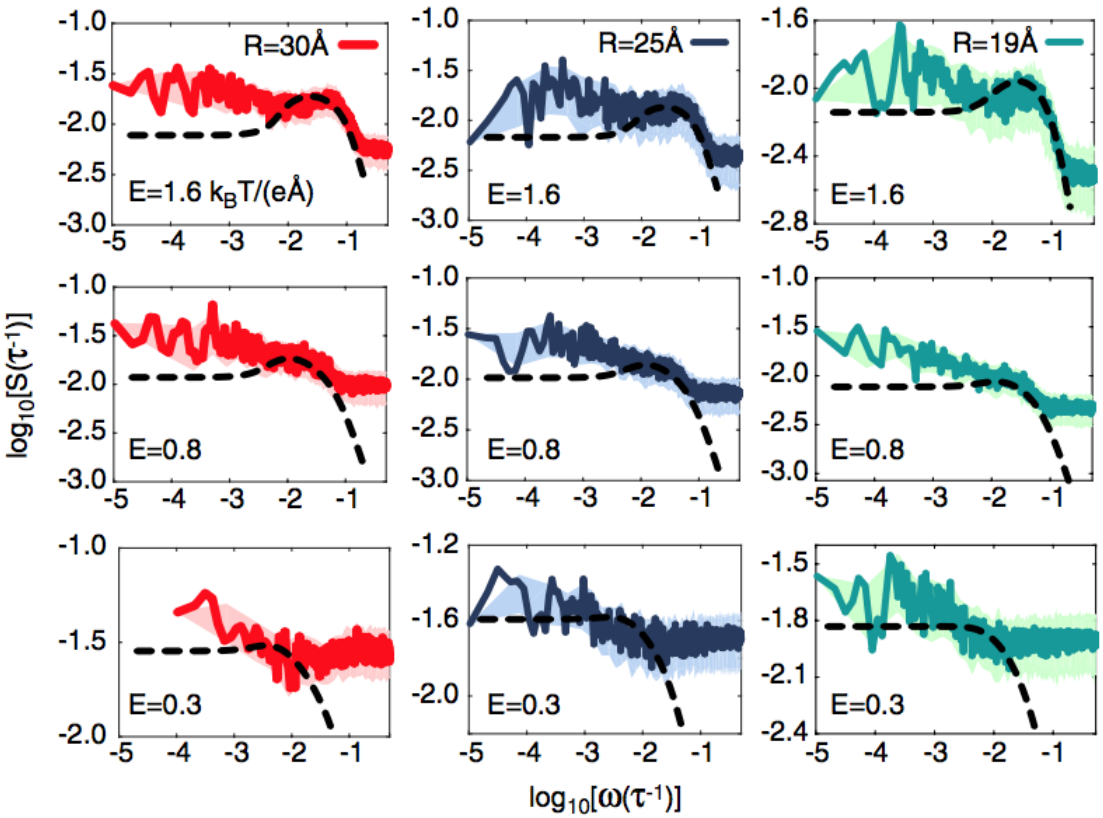

Figure 6.8: The power spectra of the ionic current through pores with different radii $R =$ 19, 25, 30 Å at equal solvent and ion concentrations of $C_i = C_s = 5.5 \times 10^{-4}$ Å^{-3}, at different applied electric field strengths $E_{\|} = 0.3,\ 0.8,\ 1.6\ k_BT/(e\text{Å})$. With increasing $E_{\|}$, the transition frequency shifts upward, and the background white noise decreases. With increasing radius the slope at high frequency increases without any alteration of the power law at low frequency. The dashed lines indicate the theory fit Eq. (4.16).

6.5 Conclusion

In this chapter, using numerical simulations with explicit coarse-grained solvent, we have presented a systematic investigation of the effects of hydrodynamic and electrostatic interactions on the power spectral density of ionic currents in nanopores. We have found that an

increase in the ion concentration at a fixed solvent density leads to a power-law behaviour at low frequencies with an exponent a increasing with ion density. The exponent reaches $a = 0.4$ at an ion concentration of $C_i = 2 \times 10^{-3}$ Å^{-3}. This conclusion is in line with our previous conclusions reached in Chaps. 3 and 5 using simulations with implicit water.

Hydrodynamic interactions appeared to influence the power spectral density at high frequencies. In particular, the transition in the power spectral density becomes less pronounced with increasing solvent density. However, at low frequencies, the hydrodynamic interactions have no effect on the power spectrum. The linearized mean-field theory without hydrodynamics, which has been derived and simplified in Chaps. 2 and 4, appeared to describe simulation results with hydrodynamic interactions equally well. Inclusion of electrostatic ion-ion correlations is paramount to describe the low-frequency power-law behaviour as a function of ion density.

However, it is important to note that in the present analysis the solvent used has a higher compressibility than water, and that the Langevin noise provides a truncation distance, which might influence the hydrodynamic interactions.

Although a direct comparison with experimental results is not yet feasible, we have asserted in this chapter that the combination of simulations and analytical work provides a promising framework for the systematic investigation of experimental noise spectra.

CHAPTER 7

Conclusion and Outlook

There is a good reason they call these ceremonies commencement exercises. Graduation is not the end; it is the beginning

Orrin Hatch (1934-)

7.1 Summary of Chapters

In Chap. 2, to approach the origin of $1/f$ noise, we present a comprehensive theoretical derivation describing the current fluctuations. To avoid non-linear terms, Coulomb interactions between ions were ignored in the derivation. A low-frequency regime and a high-frequency regime described the generated power spectrum. Contrary to experiments where at low frequencies $1/f$ noise is found, the generated spectrum was characterised by a plateau. Our focus in this thesis was to explain and analyse the concluded discrepancy. The effect of various control parameters and the resulting changes in the behaviour of the current fluctuations was studied through an analysis of the asymptotic limiting forms of the obtained expression. Theoretical derivations for the number and charge power spectra are also presented to be used later in support of our research.

Interactions between ions are essential to characterise the ionic flow through a biological or a

solid-state pore. In Chap. 3 using Langevin-dynamics simulations, we develop a model for the flow of ions through a cylindrical pore. The derived current power spectral density exhibits a power law at low frequencies indicative of $1/f$ noise. We vary several parameters and produce the corresponding power spectra. Using the formalism developed in Chap. 2 we fit the generated current power spectra. All curves showed excellent agreement at high frequencies, however only power spectra generated without ion-ion interactions followed our analytical analysis at low frequencies. Our results allowed us to propose that ion-ion correlations are a source of $1/f$ noise in nanopores.

Our linearized mean-field theory developed in Chap. 2 is considered complicated for the nanopore community. By considering the impact of each term on the current fluctuations graph, in Chap. 4 we introduce a simple expression for $S(\omega)$ evaluated over a lateral slice rather than a confined pore volume. Comparison between both expressions indicated mainly an amplitude discrepancy that can be explained by the choice of the area geometry.

In addition, numerous experiments considered that current flow of ions across the pore can be influenced by various parameters, hence the flicker noise. The advantage of our simulation is that each parameter can be tuned to analyse its effect on the power spectral density, and compare it to experiments. In Chap. 5, no differences were observed when surface charges were added to the pore wall. Varying the pore geometry by altering the pore radius or the pore length lead to an increase in the power law correlated with an increase in the ion-ion interactions. We demonstrated that at low ion concentrations our analytical derivation agrees perfectly with our simulation results at low and high frequencies. This result emphasized more the major role played by the ion-ion interactions in generating the power law at low frequencies. Varying the electric field appeared to play a role in driving the ions across the pore with a persistent power law except at vanishing values. To illustrate the influence of the gating process on the current spectrum, we built a fluctuating pore by allowing membrane particles to interact through harmonic bond potentials. Although, the resulting variation in

the cross-sectional area was found to be substantial in narrow nanopores with $R \leq 13$ Å, the power spectrum did not exhibit any distinctive variation.

Hydrodynamic interactions always posed a key question to be answered when dealing with active matter models. However, their effect is still unexplored in ionic systems. To improve nanopore reliability and to allow more translocation studies, in Chap. 6 we introduce a simplified model to simulate a nanopore with hydrodynamic interactions. Solvent particles were added to the system using a coarse-grained description. Generated current power spectra indicated that hydrodynamic interactions do not affect the shape of the power spectrum in the frequency range studied.

7.2 Ongoing Work

Throughout the chapters, we concluded that ion-ion correlations reside behind the generation of the power law at low frequencies, evocative of the searched mysterious $1/f$ noise. Hence, understanding the mechanism of the ions' current flow and elaborating on the role of the number and charge of ions across the pore arise as essential features to determine the source of the $1/f$ noise. Analysis of the charge and number autocorrelation is expected to give a better understanding of the fluctuations of the ionic current, and strengthen our theory on the role of ion-ion correlation. In Chap. 2, theoretical derivations for the number and charge density fluctuations were developed. To study their features, using Langevin-dynamics simulations developed in Chap. 3, we extract the number and charge autocorrelation, by counting the total number of positive and negative ions occupying the pore at each time step. Using collected data, we can derive the number and charge fluctuations expressions $S_N(\omega)$, $S_Q(\omega)$.

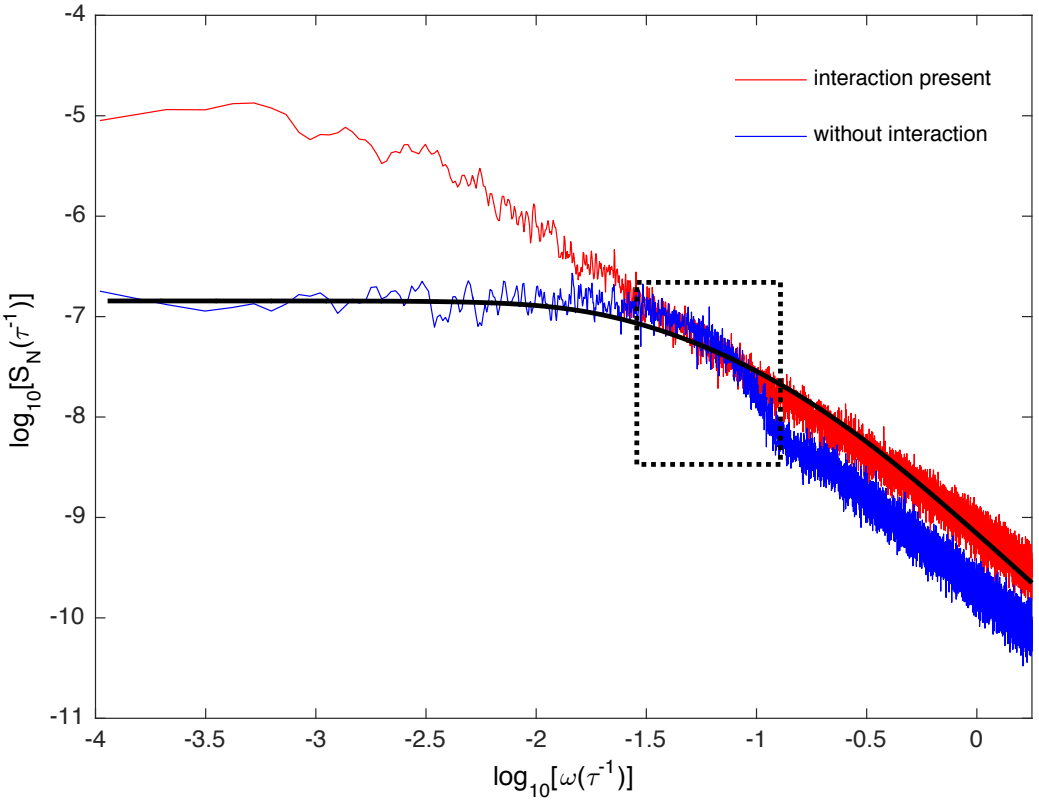

Figure 7.1: The number power spectral density $S_N(\omega)$ with the ion-ion interaction potential $V_{ion-ion}(r_{ij})$ given by Eq. (3.10) (with interactions, red line) and with $V_{ion-ion}(r_{ij}) = 0$ (without interactions, blue line). The spectra are calculated in a $R = 35$ Å channel with $E_{\|} = 0.8\ k_BT/(e\text{Å})$, and $C_0 = 3 \times 10^{-3}$ Å^{-3}.

To elaborate on the main message of the thesis, in Fig. 7.1 we show the resulting number power spectral density $S_N(\omega)$ obtained with $V_{ion-ion}(r_{ij}) = 0$, and the power spectrum obtained with full interactions ($V_{ion-ion}(r_{ij}) \neq 0$). The two curves shown were derived using a pore with a radius $R = 35$ Å, the ion concentration was set to $C_0 = 3 \times 10^{-3}$ Å^{-3}, and the applied electric field across the pore was fixed to $E = 0.8$ k$_B$T/eÅ. However, in the simulations corresponding to the blue curve, the interactions between ions were turned off contrary to the red curve where all interactions were turned on.

Explicitly the two curves reveal a discrepancy at low frequencies and a change in the exponent at high frequencies; two features that require further investigations. The black curve denotes a fit with the number power spectral density equation derived in Chap. 2, Eq. (2.48). The fitting features a plateau at low frequencies and a power law at high frequencies. The power

law exponent approaches the average exponent of the squared region of the blue curve in Fig. 7.1 and the exponent of the region at higher frequencies. The differences depicted in Fig. 7.1 recall the role of ion-ion correlations but they require more studies.

7.2.1 Future Work and Details to be Explored

In summary, in this thesis the role of ion-ion interactions in generating the commonly perceived power-law at low frequencies in the current power spectral density of the flow of ions across a channel was strongly highlighted, while at higher frequencies the dependence is controlled by other parameters such as geometric features, concentration of ions, the electric field and so on. A full analytical description of the system was presented and using various approximations simplified expressions were developed as well. However there were a few drawbacks that require further future investigations. From one side, the solvent used in studying the hydrodynamics effect did not totally mimic the water behaviour due to jamming problems, an obstacle that requires more analysis. On the other side, as highlighted in Chap. 2, dealing with pores with particular geometries change the shape of the current power spectral density. Thereby, various geometries remain to be explored to study how well the developed theoretical expression for the current power spectral density fits the generated spectra from the simulations. For instance, in Chap. 6, we had to rescale the small-scale cutoff parameter Λ when dealing with longer pores.

From another perspective, in our theory developed in Chap. 2, nonlinear terms were discarded. Recently, the structure of the nonlinear stochastic field theory was employed in developing a model for the homeostasis of a colony of cells with growth and chemical signalling using dynamical renormalization group (RG) methods[189]. To develop more our theory, we plan to perform a similar analysis with the current system in the future. This analysis would not only help in understanding more the role of ion interactions but it will also help in explaining all the features of the current power spectral density perceived at low frequencies such as the

limited plateau connecting the two power laws at low and high frequencies seen in Fig. 3.7.

7.3 Outlook

In this thesis, the evolution of our research is based on a "bottom-up" approach. In our work, we started from a simplified form of the continuity equation and the Nernst-Planck equation that we combined together to derive an accurate analytical description for the ions' current flow. For linearity purpose, in our derivation we did not account for the electric field produced by the ions themselves. To allow a better understanding of the developed current power spectral density formula, a simplified version of the derived linearized mean-field theory was developed. Langevin dynamics simulations were then performed to study the applicability of our theory. Several parameters were tuned independently to investigate their influence on the current power spectrum. This work presents the first theoretical attempt aiming at understanding the prevalence of the $1/f$ noise in ion channels. This research required very expensive simulations that demanded at least three months to be complete regardless of the machine failures, a factor that made the work more challenging. Although it is important to keep in mind that this is a theoretical study of an idealized system with implicit water or explicit solvent, the effects of the ion concentration and the pore geometry on the power spectral density can be tested experimentally.

CHAPTER 8

Appendix

8.1 Current Density Fluctuations Expression

In this section, we present a detailed derivation for $\left\langle \left| \widetilde{J^+}(\mathbf{q},\omega) - \widetilde{J^-}(\mathbf{q},\omega) \right|^2 \right\rangle$ a main component of the current power spectral density expression.

Using Eqs. (2.11) and (2.16) from Chap. 2 and ignoring the DC component of the current density, we write the expression for the current density $J_\rho(\mathbf{q},\omega)$:

$$\begin{aligned} J_\rho(\mathbf{q},\omega) = \; & iD\mathbf{q}\left(1+\frac{\kappa^2}{q^2}\right)[G_\rho^+(\mathbf{q},\omega)+G_\rho^-(\mathbf{q},\omega)][-i\mathbf{q}\cdot\boldsymbol{\eta}^+(\mathbf{q},\omega)] \\ & + iD\mathbf{q}\left(1+\frac{\kappa^2}{q^2}\right)[G_\rho^+(\mathbf{q},\omega)-G_\rho^-(\mathbf{q},\omega)][-i\mathbf{q}\cdot\boldsymbol{\eta}^-(\mathbf{q},\omega)] \\ & + D\boldsymbol{\mathcal{E}}[G_c^+(\mathbf{q},\omega)+G_c^-(\mathbf{q},\omega)][-i\mathbf{q}\cdot\boldsymbol{\eta}^+(\mathbf{q},\omega)] \\ & + D\boldsymbol{\mathcal{E}}[G_c^+(\mathbf{q},\omega)-G_c^-(\mathbf{q},\omega)][-i\mathbf{q}\cdot\boldsymbol{\eta}^-(\mathbf{q},\omega)] - \boldsymbol{\eta}^+(\mathbf{q},\omega)+\boldsymbol{\eta}^-(\mathbf{q},\omega). \end{aligned} \tag{8.1}$$

The electric field is nonzero only in the parallel direction $\boldsymbol{\mathcal{E}} = (0,0,\mathcal{E}_\parallel)$. Interested in the longitudinal flow of ions through the pore, we concentrate on the flux in the parallel direction. To proceed, we multiply the parallel component of $J_\rho(\mathbf{q},\omega)$ by its corresponding complex conjugate $J_\rho^*(\mathbf{q},\omega)$ and we take the corresponding average. For this target, we need to

specify the spectrum of the noise terms. Since the noise originates from Poissonian number fluctuations, a consistent prescription within our calculations will be to regard them as independent Gaussian distributed white noise terms of zero mean, with variances that are controlled by the average concentration. The corresponding expression in real and Fourier space using index notation are respectively:

$$\begin{aligned}\langle \eta_i^a(\boldsymbol{x},t)\,\eta_j^b(\boldsymbol{x}',t')\rangle &= 2DC_{\mathrm{pore}}\delta^{ab}\delta_{ij}\delta^3(\boldsymbol{x}-\boldsymbol{x}')\delta(t-t'),\\ \langle \eta_i^a(\mathbf{q},\omega)\eta_j^b(\mathbf{q}',\omega')\rangle &= 2DC_{\mathrm{pore}}\delta^{ab}\delta_{ij}(2\pi)^4\delta^3(\mathbf{q}+\mathbf{q}')\delta(\omega+\omega'),\end{aligned} \tag{8.2}$$

where a and b can be $+$ or $-$. We note that $q^2 = q_\parallel^2 + q_{\perp 1}^2 + q_{\perp 2}^2$ and $q_\perp^2 = q_{\perp 1}^2 + q_{\perp 2}^2$. The expression of $\langle J_\rho(\mathbf{q},\omega)J_\rho^*(\mathbf{q},\omega)\rangle$ reduces to:

$$\begin{aligned}\left\langle \left| \widetilde{J}_\parallel^+(\mathbf{q},\omega) - \widetilde{J}_\parallel^-(\mathbf{q},\omega)\right|^2\right\rangle = \; & 2DC_{\mathrm{pore}}\Big[[G_\rho^+ + G_\rho^-][G_\rho^{+*} + G_\rho^{-*}][D^2q_\parallel^2q^2 + 2\kappa^2D^2q_\parallel^2 + \kappa^4D^2\big(\frac{q_\parallel}{q}\big)^2]\\ & + [G_\rho^+ - G_\rho^-][G_\rho^{+*} - G_\rho^{-*}][D^2q_\parallel^2q^2 + 2\kappa^2D^2q_\parallel^2 + \kappa^4D^2\big(\frac{q_\parallel}{q}\big)^2]\\ & + [G_\rho^+ + G_\rho^-][G_c^{+*} + G_c^{-*}][iD^2\mathcal{E}_\parallel q_\parallel q^2 + i\kappa^2D^2\mathcal{E}_\parallel q_\parallel]\\ & + [G_\rho^+ - G_\rho^-][G_c^{+*} - G_c^{-*}][iD^2\mathcal{E}_\parallel q_\parallel q^2 + i\kappa^2D^2\mathcal{E}_\parallel q_\parallel]\\ & + [G_c^+ + G_c^-][G_\rho^{+*} + G_\rho^{-*}][-iD^2\mathcal{E}_\parallel q_\parallel q^2 - i\kappa^2D^2\mathcal{E}_\parallel q_\parallel]\\ & + [G_c^+ - G_c^-][G_\rho^{+*} - G_\rho^{-*}][-iD^2\mathcal{E}_\parallel q_\parallel q^2 - i\kappa^2D^2\mathcal{E}_\parallel q_\parallel]\\ & + 2iD\mathcal{E}_\parallel q_\parallel[G_c^- - G_c^{-*}] - 2Dq_\parallel^2[G_\rho^- + G_\rho^{-*}] - 2\kappa^2D\big(\frac{q_\parallel}{q}\big)^2[G_\rho^- + G_\rho^{-*}]\\ & + D^2\mathcal{E}_\parallel^2q^2[G_c^+ + G_c^-][G_c^{+*} + G_c^{-*}] + D^2\mathcal{E}_\parallel^2q^2[G_c^+ - G_c^-][G_c^{+*} - G_c^{-*}] + 2\Big],\end{aligned} \tag{8.3}$$

where we use "*" to denote the complex conjugate. Replacing $G_\rho(\mathbf{q},\omega)$, $G_\rho^*(\mathbf{q},\omega)$, $G_c(\mathbf{q},\omega)$, and $G_c^*(\mathbf{q},\omega)$ by their explicit expressions in Eq. (2.17), we conclude the final expression for

$\left\langle \left| \widetilde{J}_{\parallel}^{+}(\mathbf{q},\omega) - \widetilde{J}_{\parallel}^{-}(\mathbf{q},\omega) \right|^2 \right\rangle$:

$$\begin{aligned}
&\left\langle \left| \widetilde{J}_{\parallel}^{+}(\mathbf{q},\omega) - \widetilde{J}_{\parallel}^{-}(\mathbf{q},\omega) \right|^2 \right\rangle = \\
&4DC_{\text{pore}}\Bigg[1 + \frac{\omega^2\left[D^2\mathcal{E}_{\parallel}^2 q^2[2q_{\parallel}^2 + q^2] - \kappa^2 D^2 q_{\parallel}^2(\kappa^2 + 2q^2) - D^2 q_{\parallel}^2 q^4\right]}{q^2\left[(-\omega^2 + D^2q^4 + D^2q^2\kappa^2 + D^2q_{\parallel}^2\mathcal{E}_{\parallel}^2)^2 + (2\omega Dq^2 + \omega D\kappa^2)^2\right]} \\
&+ \frac{[q_{\perp}^2 - q_{\parallel}^2][2D^4\kappa^2 q^4\mathcal{E}_{\parallel}^2 + D^4\mathcal{E}_{\parallel}^4 q_{\parallel}^2 q^2 + D^4\kappa^4\mathcal{E}_{\parallel}^2 q^2]}{q^2\left[(-\omega^2 + D^2q^4 + D^2q^2\kappa^2 + D^2q_{\parallel}^2\mathcal{E}_{\parallel}^2)^2 + (2\omega Dq^2 + \omega D\kappa^2)^2\right]} \\
&+ \frac{-D^4\kappa^2 q^4 q_{\parallel}^2[\kappa^2 + 2q^2] + D^4 q^8[\mathcal{E}_{\parallel}^2 - q_{\parallel}^2] + D^4\kappa^4 q_{\parallel}^4\mathcal{E}_{\parallel}^2 - D^4 q_{\parallel}^2 q^4\mathcal{E}_{\parallel}^2[q_{\parallel}^2 + 2q^2]}{q^2\left[(-\omega^2 + D^2q^4 + D^2q^2\kappa^2 + D^2q_{\parallel}^2\mathcal{E}_{\parallel}^2)^2 + (2\omega Dq^2 + \omega D\kappa^2)^2\right]}\Bigg].
\end{aligned} \tag{8.4}$$

8.2 Number and Charge Densities

Similarly, to determine the power spectra of the charge and number densities, we begin by constructing the expressions for $C(\mathbf{q},\omega)$ and $Q(\mathbf{q},\omega)$ in Fourier space in terms of $G(\mathbf{q},\omega)$ functions:

$$\begin{cases}
C(\mathbf{q},\omega) = [G_c^{+}(\mathbf{q},\omega) + G_c^{-}(\mathbf{q},\omega)][-i\mathbf{q}\cdot\boldsymbol{\eta}^{+}(\mathbf{q},\omega)] + [G_c^{+}(\mathbf{q},\omega) - G_c^{-}(\mathbf{q},\omega)][-i\mathbf{q}\cdot\boldsymbol{\eta}^{-}(\mathbf{q},\omega)], \\
\rho(\mathbf{q},\omega) = [G_\rho^{+}(\mathbf{q},\omega) + G_\rho^{-}(\mathbf{q},\omega)][-i\mathbf{q}\cdot\boldsymbol{\eta}^{+}(\mathbf{q},\omega)] + [G_\rho^{+}(\mathbf{q},\omega) - G_\rho^{-}(\mathbf{q},\omega)][-i\mathbf{q}\cdot\boldsymbol{\eta}^{-}(\mathbf{q},\omega)].
\end{cases} \tag{8.5}$$

By taking the average of the product of Eqs. (8.5) by their complex conjugates, we get:

$$\begin{cases}
\langle C(\mathbf{q},\omega)C^{*}(\mathbf{q},\omega)\rangle = \left|G_c^{+}(\mathbf{q},\omega) + G_c^{-}(\mathbf{q},\omega)\right|^2 q^2 + \left|G_c^{+}(\mathbf{q},\omega) - G_c^{-}(\mathbf{q},\omega)\right|^2 q^2, \\
\langle \rho(\mathbf{q},\omega)\rho^{*}(\mathbf{q},\omega)\rangle = \left|G_\rho^{+}(\mathbf{q},\omega) + G_\rho^{-}(\mathbf{q},\omega)\right|^2 q^2 + \left|G_\rho^{+}(\mathbf{q},\omega) - G_\rho^{-}(\mathbf{q},\omega)\right|^2 q^2.
\end{cases} \tag{8.6}$$

From this point, we replace $G_c(\mathbf{q},\omega)$ and $G_\rho(\mathbf{q},\omega)$ by their explicit expressions defined in Eq. (2.17), to reach the final form for $\langle\left|\tilde{C}^+(\mathbf{q},\omega)+\tilde{C}^-(\mathbf{q},\omega)\right|^2\rangle$ and $\langle\left|\tilde{C}^+(\mathbf{q},\omega)-\tilde{C}^-(\mathbf{q},\omega)\right|^2\rangle$:

$$\begin{cases} \langle\left|\tilde{C}^+(\mathbf{q},\omega)+\tilde{C}^-(\mathbf{q},\omega)\right|^2\rangle \\ = \dfrac{4DC_{\text{pore}}q^2\left[D^2(q^2+\kappa^2)^2+\omega^2+D^2Q_\parallel^2\mathcal{E}_\parallel^2\right]}{(-\omega^2+D^2q^4+\kappa^2D^2q^2+D^2q_\parallel^2\mathcal{E}_\parallel^2)^2+(2\omega Dq^2+\omega\kappa^2D)^2}, \\ \langle\left|\tilde{C}^+(\mathbf{q},\omega)-\tilde{C}^-(\mathbf{q},\omega)\right|^2\rangle \\ = \dfrac{4DC_{\text{pore}}q^2\left[D^2q^4+D^2q_\parallel^2\mathcal{E}_\parallel^2+\omega^2\right]}{(-\omega^2+D^2q^4+D^2q^2\kappa^2+D^2q_\parallel^2\mathcal{E}_\parallel^2)^2+(2\omega Dq^2+\omega D\kappa^2)^2}. \end{cases} \tag{8.7}$$

8.3 More Data for Chapter 3

Using higher electric field $E_\parallel = 1.1\ k_BT/(e\text{Å})$ induces a higher power law at low frequency and prevents the freezing of the ions. In Fig. 8.1 we show data from two simulations using a radii $R = 25$ and $R = 19$ Å and $C_{\text{pore}} = 1\times10^{-3}$ Å^{-3}. The value of the exponent a characterising the power law at low frequency increases from 0.54 to 0.59 for the pore with the radius $R = 25$ Å and from 0.48 to 0.51 when $R = 19$ Å.

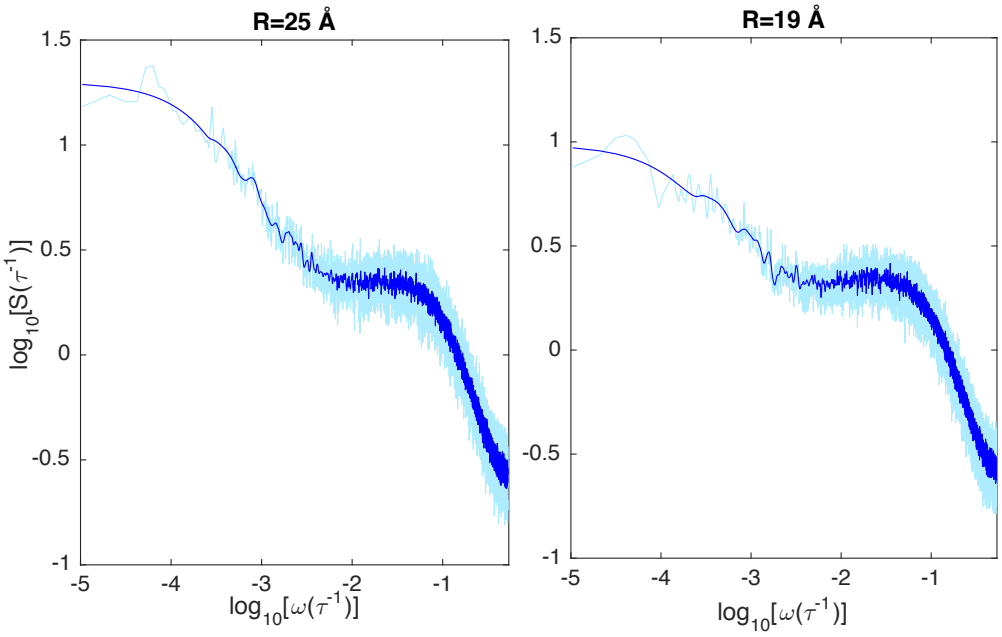

Figure 8.1: The power spectra calculated in a $R = 25$ Å and $R = 19$ Å channels with $E_{\|} = 1.1\ k_BT/(e\text{Å})$, and $C_{pore} = 1 \times 10^{-3}$ Å^{-3}. The exponent a characterising the power law at low frequencies increases to 0.59 for $R = 25$ Å and 0.51 for $R = 19$ Å. The dashed lines denote fits to Eq. (2.25). The diffusion coefficient $D = 1$ Å$^2/\tau$ and the small-scale cutoff length is set to the ion size, $\Lambda = 3$ Å, for the two curves.

8.4 Mass Dependence

Previously we mentioned that we treat the ions equally with the same mass. To study the influence of this constraint we alter the mass of the ions. The mass m_i of the ions in the Langevin dynamics simulations is directly related to the time scale. To study its role, we generate the current power spectral density from simulations using different values of m_i (Fig. 8.2). When the time scale τ is scaled by the mass of the particles, the curves all fall on top of each other (inset), showing that the time scale is linearly coupled to the mass scale. The value of m_i that correctly reproduces the physical properties of an electrolyte depends on the properties of the ions, such as their interaction potentials and valency. For our fit curves, the unknown mass allows us to rescale the time scale τ, shifting the curves along the diagonal axis by a constant amount.

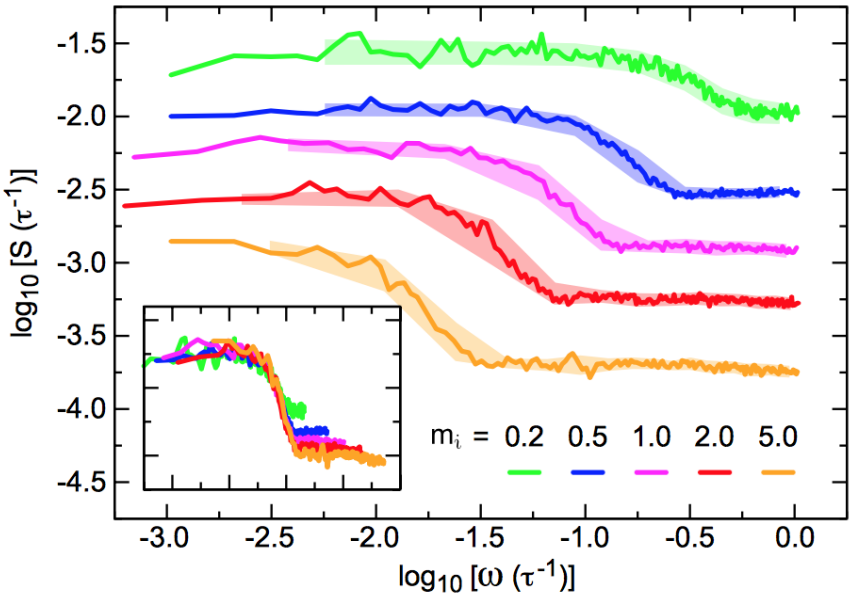

Figure 8.2: The power spectral density as a function of the ion mass m_i. The pores have a radius $R = 25$ Å and a length $L = 48$ Å. We use $\delta t = 3\tau$ and only Lennard-Jones interactions between the particles. In the inset, the curves have been scaled by the mass.

8.5 Graph rescaling

In the Langevin dynamics simulations, the fluctuations are coarse-grained in discrete time steps and over individual particles. Thereby, one of the consequences of the coarse-graining is that even at vanishing electric field and at high frequency, the power spectra of the flux of positive and negative ions do not cancel. Instead a background noise level depending on the number of particles and the time step is generated. The power spectral density of the electric current due to these background fluctuations in terms of the time step δt of the simulation equals $S = (z/L)^2 \langle N \rangle \delta t$. At high frequency, the background noise dominates depending on δ as well. (Details in the following section)

The current power spectral density generated using the simplified form of the mean field theory developed in Chap. 5, exhibits an amplitude difference. As it was developed, this difference depends strongly on the choice of the area function. Because the shape of the pores

in our simulations is irregular due to the discrete particles used for the pore wall, there are multiple justifiable choices for the shape of the area function, each resulting in a different amplitude. To take this uncertainty into account, we allow the amplitudes of the fit curves in Chaps. 5 and 6 to be scaled by a single factor. To fit the data, we can scale all the fit curves $S(\omega)$ by the same factor 110. Finally, as we have shown, the choice of the time step influence the persistence of the white noise at high frequency and the time scale τ of the simulations scales linearly with the mass m_i of the ions (8.4). Because the mass in the simulations is set to an arbitrary constant, the time scale of the simulations does not necessarily correspond to the time scale of the linearized mean-field theory. To account for this discrepancy, we allow the time scale of the fit curves in Chaps. 5 and 6 to be scaled by a single factor depending only on the properties of the ions. To fit the data, we use a factor 0.05 for all the simulations of monovalent ions, and 0.07 for the divalent ions.

8.6 Background noise level.

Contrary to the fluctuations $\boldsymbol{\eta}(\boldsymbol{x}, t)$ in the linearized mean-field theory, the fluctuations $\boldsymbol{\xi}(t)$ in the simulations are coarse-grained over time and applied to individual particles. As a result, the simulated data in Chaps. 5 and 6 contain a background noise level that neither vanishes with vanishing electric field, nor with increasing frequency. We calculate the level of the noise at high frequency, where the background noise dominates, and plot it as a function of the theoretical expression $S(\omega) = D\langle N\rangle(\delta t/\tau)(z/L)^2$ (Fig. 8.3). For all radii, concentrations, vallencies, and electric field strengths, the theoretical prediction fits the data very well, substantiating our expression for the background noise correction.

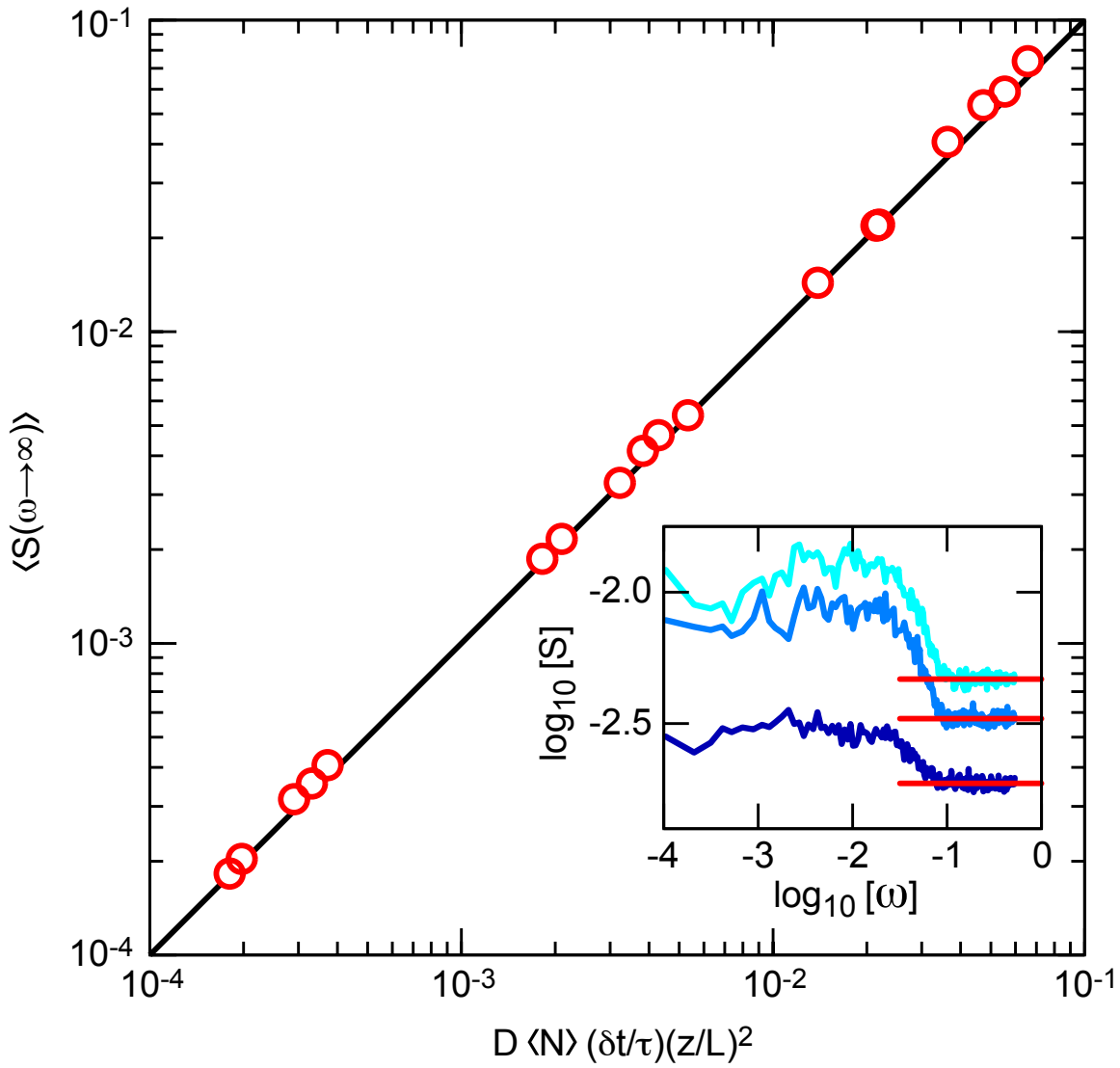

Figure 8.3: The mean amplitude of the high frequency plateau in the power spectrum as a function of the theoretical expression for all power spectra.The black line indicates $\langle S(\omega \to \infty)\rangle = D\langle N\rangle(\delta t/\tau)(z/L)^2$. Three examples of the determination of the mean high frequency noise level are shown in the inset.

CHAPTER 9

References

"The devil can cite Scripture for his purpose."

William Shakespeare (1564–1616)

Bibliography

[1] M. Zorkot and R. Golestanian. Current fluctuations across a nanopore. *Journal of Physics: Condensed Matter* 30(13):134001, 2018.

[2] M. Zorkot, R. Golestanian, and D. J. Bonthuis. The power spectrum of ionic nanopore currents: the role of ion correlations. *Nano Letters* 16(4):2205–2212, 2016.

[3] M. Zorkot, R. Golestanian, and D. J. Bonthuis. Current fluctuations in nanopores: The effects of electrostatic and hydrodynamic interactions. *The European Physical Journal Special Topics* 225(8-9):1583–1594, 2016.

[4] A. B. Downey. *Think complexity: complexity science and computational modeling.* "O'Reilly Media, Inc.", 2012.

[5] S. W. Smith et al. *The scientist and engineer's guide to digital signal processing.* California Technical Pub. San Diego, 1997.

[6] N. Leibovich, A. Dechant, E. Lutz, and E. Barkai. Aging Wiener-Khinchin theorem and critical exponents of $1/f^{\beta}$ noise. *Physical Review E* 94(5):052130, 2016.

[7] B. B. Mandelbrot and J. W. Van Ness. Fractional brownian motions, fractional noises and applications. *SIAM Review* 10(4):422–437, 1968.

[8] N. A. Clark, J. H. Lunacek, and G. B. Benedek. A study of brownian motion using light scattering. *American Journal of Physics* 38(5):575–585, 1970.

[9] F. Gittes and C. F. Schmidt. Signals and noise in micromechanical measurements. *Methods in Cell Biology* 55:129–156, 1997.

[10] R. F. Voss and J. Clarke. "1/f noise" in music and speech. *Nature* 258:317–318, 1975.

[11] J. B. Johnson. The Schottky effect in low frequency circuits. *Physical Review Letters* 26(1):71, 1925.

[12] W. Schottky. Small-shot effect and flicker effect. *Physical Review Letters* 28(1):74, 1926.

[13] B. Mandelbrot, C. Fractals-Form, and W. Dimension. *Fractals: Form, Chance And Dimension.* W. H. Freeman and Co., 1977.

[14] B. Taft, B. Hickey, C. Wunsch, and D. Baker. Equatorial undercurrent and deeper flows in the central pacific. *Deep Sea Research and Oceanographic Abstracts* 21:403–430, 1974.

[15] R. F. Voss and J. Clarke. "1/f noise" in music: Music from 1/f noise. *The Journal of the Acoustical Society of America* 63(1):258–263, 1978.

[16] F. Hooge. 1/f noise sources. *IEEE Transactions on Electron Devices* 41(11):1926–1935, 1994.

[17] C. Wunsch. Bermuda sea level in relation to tides, weather, and baroclinic fluctuations. *Reviews of Geophysics* 10(1):1–49, 1972.

[18] D. Bell. A survey of 1/f noise in electrical conductors. *Journal of Physics C: Solid State Physics* 13(24):4425, 1980.

[19] J. B. Johnson. Thermal agitation of electricity in conductors. *Physical Review Letters* 32(1):97, 1928.

[20] H. Nyquist. Thermal agitation of electric charge in conductors. *Physical Review Letters* 32(1): 110, 1928.

[21] P. Hänggi and H. Thomas. Stochastic processes: Time evolution, symmetries and linear response. *Physics Reports* 88(4):207–319, 1982.

[22] C. W. Gardiner. *Stochastic Methods*. Springer-Verlag, Berlin–Heidelberg–New York–Tokyo, 1985.

[23] M. Büttiker. Scattering theory of thermal and excess noise in open conductors. *Physical Review Letters* 65(23):2901, 1990.

[24] A. d'Amico and P. Mazzetti. *Noise in physical systems and 1/f noise-1985*. Elsevier, 2012.

[25] D. V. Perepelitsa. Johnson noise and shot noise. *Dept. of Physics, MIT* 2006.

[26] R. Shaw. Strange attractors, chaotic behavior, and information flow. *Zeitschrift für Naturforschung A* 36(1):80–112, 1981.

[27] T. Kleinpenning and A. de Kuijper. Relation between variance and sample duration of 1/f noise signals. *Journal of Applied Physics* 63(1):43–45, 1988.

[28] R. Agrawal, C. Faloutsos, and A. Swami. Efficient similarity search in sequence databases. In D. B. Lomet, editor, *Foundations of Data Organization and Algorithms*, pages 69–84, Berlin, Heidelberg, 1993. Springer Berlin Heidelberg.

[29] J. M. Halley. Ecology, evolution and 1/f-noise. *Trends in Ecology & Evolution* 11(1):33–37, 1996.

[30] D. L. Gilden. Cognitive emissions of 1/f noise.. *Psychological Review* 108(1):33, 2001.

[31] D. Kaplan and L. Glass. *Understanding Nonlinear Dynamics*. Springer-Verlag New York, 2012.

[32] F. N. Hooge. 1/ noise is no surface effect. *Physics Letters A* 29(3):139–140, 1969.

[33] F. Hooge. Discussion of recent experiments on 1/ noise. *Physica* 60(1):130–144, 1972.

[34] P. Dutta and P. Horn. Low-frequency fluctuations in solids: 1/f noise. *Reviews of Modern Physics* 53(3):497, 1981.

[35] F. Hooge, T. Kleinpenning, and L. Vandamme. Experimental studies on 1/f noise. *Reports on Progress in Physics* 44(5):479, 1981.

[36] A. Van der Ziel. Unified presentation of 1/f noise in electron devices: fundamental 1/f noise sources. *Proceedings of the IEEE* 76(3):233–258, 1988.

[37] P. G. Collins, M. Fuhrer, and A. Zettl. 1/f noise in carbon nanotubes. *Applied Physics Letters* 76(7):894–896, 2000.

[38] A. Van der Ziel. Flicker noise in electronic devices. *Advances in Electronics and Electron Physics* 49:225–297, 1979.

[39] M. Nelkin and A.-M. Tremblay. Deviation of 1/f voltage fluctuations from scale-similar gaussian behavior. *Journal of Statistical Physics* 25(2):253–268, 1981.

[40] M. Caloyannides. Microcycle spectral estimates of 1/f noise in semiconductors. *Journal of Applied Physics* 45(1):307–316, 1974.

[41] F. Hooge. 1/f noise. *Physica B+ C* 83(1):14–23, 1976.

[42] A. McWhorter. 1/f noise and germanium surface properties. *Semiconductor Surface Physics* pages 207–228, 1957.

[43] K. K. Hung, P. K. Ko, C. Hu, and Y. C. Cheng. A unified model for the flicker noise in metal-oxide-semiconductor field-effect transistors. *IEEE Transactions on Electron Devices* 37 (3):654–665, 1990.

[44] K. K. Hung, P. K. Ko, C. Hu, and Y. C. Cheng. A physics-based mosfet noise model for circuit simulators. *IEEE Transactions on Electron Devices* 37(5):1323–1333, 1990.

[45] T. Musha, S. Sato, and M. Yamamoto. *Noise in physical systems and 1/f fluctuations*. IOS

Press, 1992.

[46] J. Richardson. The linear theory of fluctuations arising from diffusional mechanisms—an attempt at a theory of contact noise. *Bell System Technical Journal* 29(1):117–141, 1950.

[47] I. Lundström, D. McQueen, and C. Klason. On low frequency and 1/f noise from diffusion like processes. *Solid State Communications* 13(12):1941–1944, 1973.

[48] R. Rammal, C. Tannous, and A.-M. Tremblay. 1/f noise in random resistor networks: fractals and percolating systems. *Physical Review A* 31(4):2662, 1985.

[49] R. F. Voss and J. Clarke. Flicker (1/f) noise: Equilibrium temperature and resistance fluctuations. *Physical Review B* 13(2):556, 1976.

[50] M. Weissman. 1 f noise and other slow, nonexponential kinetics in condensed matter. *Reviews of Modern Physics* 60(2):537, 1988.

[51] P. Bak, C. Tang, and K. Wiesenfeld. Self-organized criticality: An explanation of the 1/f noise. *Physical Review Letters* 59(4):381, 1987.

[52] P. Bak and C. Tang. Earthquakes as a self-organized critical phenomenon. *J. Geophys. Res* 94 (15):635–15, 1989.

[53] J. Hesse and T. Gross. Self-organized criticality as a fundamental property of neural systems. *Criticality as a signature of healthy neural systems: multi-scale experimental and computational studies* 2015.

[54] D. Dhar and R. Ramaswamy. Exactly solved model of self-organized critical phenomena. *Physical Review Letters* 63(16):1659, 1989.

[55] D. Dhar. Self-organized critical state of sandpile automaton models. *Physical Review Letters* 64 (14):1613, 1990.

[56] T. Hwa and M. Kardar. Dissipative transport in open systems: An investigation of self-organized criticality. *Physical Review Letters* 62(16):1813, 1989.

[57] T. Hwa and M. Kardar. Avalanches, hydrodynamics, and discharge events in models of sandpiles. *Physical Review A* 45(10):7002, 1992.

[58] N. W. Watkins, G. Pruessner, S. C. Chapman, N. B. Crosby, and H. J. Jensen. 25 years of self-organized criticality: concepts and controversies. *Space Science Reviews* 198(1-4):3–44, 2016.

[59] R. F. Voss. Evolution of long-range fractal correlations and 1/f noise in DNA base sequences. *Physical Review Letters* 68(25):3805, 1992.

[60] G. F. Schneider, S. W. Kowalczyk, V. E. Calado, G. Pandraud, H. W. Zandbergen, L. M. Vandersypen, and C. Dekker. DNA translocation through graphene nanopores. *Nano Letters* 10 (8):3163–3167, 2010.

[61] F. Bezanilla. The voltage sensor in voltage-dependent ion channels. *Physiological Reviews* 80(2): 555–592, 2000.

[62] B. Hille. Ionic selectivity, saturation, and block in sodium channels. a four-barrier model.. *The Journal of General Physiology* 66(5):535–560, 1975.

[63] D. W. Deamer and M. Akeson. Nanopores and nucleic acids: prospects for ultrarapid sequencing. *Trends Biotechnol.* 18:131–180, 2000.

[64] A. Meller, L. Nivon, E. Brandin, J. Golovchenko, and D. Branton. Rapid nanopore discrimination between single polynucleotide molecules. *Proc. Nat. Acad. Sci. USA* 97:1079–1084, 2000.

[65] A. H. Laszlo, I. M. Derrington, and Ross. Decoding long nanopore sequencing reads of natural DNA. *Nature Biotechnology* 32(8):829–833, 2014.

[66] H. Reuter and C. Stevens. Ion conductance and ion selectivity of potassium channels in snail neurones. *Journal of Membrane Biology* 57(2):103–118, 1980.

[67] R. Latorre and C. Miller. Conduction and selectivity in potassium channels. *Journal of Membrane Biology* 71(1):11–30, 1983.

[68] W. A. Catterall. Structure and function of voltage-sensitive ion channels. *Science* 242(4875): 50–61, 1988.

[69] R. A. Kumpf and D. A. Dougherty. A mechanism for ion selectivity in potassium channels: computational studies of cation-pi interactions. *Science* 261(5129):1708–1710, 1993.

[70] W. A. Catterall. Cellular and molecular biology of voltage-gated sodium channels. *Physiological Reviews* 72(suppl 4):S15–S48, 1992.

[71] W. A. Catterall. Structure and function of voltage-gated ion channels. *Annual review of biochemistry* 64(1):493–531, 1995.

[72] J. J. Kasianowicz, E. Brandin, D. Branton, and D. W. Deamer. Characterization of individual

polynucleotide molecules using a membrane channel. *Proceedings of the National Academy of Sciences* 93(24):13770–13773, 1996.

[73] D. A. Doyle, J. M. Cabral, R. A. Pfuetzner, A. Kuo, J. M. Gulbis, S. L. Cohen, B. T. Chait, and R. MacKinnon. The structure of the potassium channel: molecular basis of k+ conduction and selectivity. *Science* 280(5360):69–77, 1998.

[74] D. J. Aidley and P. R. Stanfield. *Ion channels: molecules in action.* Cambridge University Press, 1996.

[75] B. Hille et al. *Ion channels of excitable membranes*, volume 507. Sinauer Sunderland, MA, 2001.

[76] G. Yellen. The voltage-gated potassium channels and their relatives. *Nature* 419(6902):35, 2002.

[77] T. J. Jentsch, C. A. Hübner, and J. C. Fuhrmann. Ion channels: function unravelled by dysfunction. *Nature Cell Biology* 6(11):1039–1047, 2004.

[78] S. Y. Noskov, S. Berneche, and B. Roux. Control of ion selectivity in potassium channels by electrostatic and dynamic properties of carbonyl ligands. *Nature* 431(7010):830, 2004.

[79] F. Bezanilla and C. M. Armstrong. Negative conductance caused by entry of sodium and cesium ions into the potassium channels of squid axons. *The Journal of General Physiology* 60(5): 588–608, 1972.

[80] E. Gouaux and R. MacKinnon. Principles of selective ion transport in channels and pumps. *Science* 310(5753):1461–1465, 2005.

[81] S. Y. Noskov and B. Roux. Ion selectivity in potassium channels. *Biophysical Chemistry* 124(3): 279–291, 2006.

[82] D. Branton, D. W. Deamer, A. Marziali, H. Bayley, S. A. Benner, T. Butler, M. Di Ventra, S. Garaj, A. Hibbs, X. Huang, et al. The potential and challenges of nanopore sequencing. *Nature Biotechnology* 26(10):1146–1153, 2008.

[83] D. C. Gadsby. Ion channels versus ion pumps: the principal difference, in principle. *Nature reviews. Molecular cell biology* 10(5):344, 2009.

[84] C. Vergara, R. Latorre, N. V. Marrion, and J. P. Adelman. Calcium-activated potassium channels. *Current Opinion in Neurobiology* 8(3):321–329, 1998.

[85] J. Aqvist and V. Luzhkov. Ion permeation mechanism of the potassium channel. *Nature* 404 (6780):881, 2000.

[86] B. Hille. Gating in sodium channels of nerve. *Annual review of physiology* 38(1):139–152, 1976.

[87] W. A. Catterall. Voltage-dependent gating of sodium channels: correlating structure and function. *Trends in Neurosciences* 9:7–10, 1986.

[88] J. R. Moorman, G. E. Kirsch, A. M. VanDongen, R. H. Joho, and A. M. Brown. Fast and slow gating of sodium channels encoded by a single mrna. *Neuron* 4(2):243–252, 1990.

[89] N. Yang, A. L. George, and R. Horn. Molecular basis of charge movement in voltage-gated sodium channels. *Neuron* 16(1):113–122, 1996.

[90] A. L. Goldin, R. L. Barchi, J. H. Caldwell, F. Hofmann, J. R. Howe, J. C. Hunter, R. G. Kallen, G. Mandel, M. H. Meisler, Y. B. Netter, et al. Nomenclature of voltage-gated sodium channels. *Neuron* 28(2):365–368, 2000.

[91] J. M. Berg, J. L. Tymoczko, and L. Stryer. *Biochemistry, Fifth Edition.* W.H. Freeman, 2002.

[92] B. Hille, A. M. Woodhull, and B. Shapiro. Negative surface charge near sodium channels of nerve: divalent ions, monovalent ions, and ph. *Philosophical Transactions of the Royal Society of London B: Biological Sciences* 270(908):301–318, 1975.

[93] W. A. Catterall. From ionic currents to molecular mechanisms: the structure and function of voltage-gated sodium channels. *Neuron* 26(1):13–25, 2000.

[94] D. A. Köpfer. *Ion Conductance Through Potassium Channels.* PhD thesis, Göttingen Graduate School for Neurosciences, 2015.

[95] A. L. Hodgkin and A. F. Huxley. A quantitative description of membrane current and its application to conduction and excitation in nerve. *The Journal of Physiology* 117(4):500, 1952.

[96] P. S. Singh, H.-S. M. Chan, S. Kang, and S. G. Lemay. Stochastic amperometric fluctuations as a probe for dynamic adsorption in nanofluidic electrochemical systems. *Journal of the American Chemical Society* 133(45):18289–18295, 2011.

[97] S. Heerema, G. Schneider, M. Rozemuller, L. Vicarelli, H. Zandbergen, and C. Dekker. 1/f noise in graphene nanopores. *Nanotechnology* 26(7):074001, 2015.

[98] R. M. Smeets, U. F. Keyser, N. H. Dekker, and C. Dekker. Noise in solid-state nanopores. *Proceedings of the National Academy of Sciences* 105(2):417–421, 2008.

[99] V. Tabard-Cossa, D. Trivedi, M. Wiggin, N. N. Jetha, and A. Marziali. Noise analysis and reduction in solid-state nanopores. *Nanotechnology* 18(30):305505, 2007.

[100] A. Verveen and H. Derksen. Fluctuations in membrane potential of axons and the problem of coding. *Biological Cybernetics* 2(4):152–160, 1965.

[101] F. Conti, L. De Felice, and E. Wanke. Potassium and sodium ion current noise in the membrane of the squid giant axon.. *The Journal of Physiology* 248(1):45, 1975.

[102] H. M. Fishman. Relaxation spectra of potassium channel noise from squid axon membranes. *Proceedings of the National Academy of Sciences* 70(3):876–879, 1973.

[103] D. J. Poussart. Membrane current noise in lobster axon under voltage clamp. *Biophysical Journal* 11(2):211–234, 1971.

[104] H. M. Fishman. Noise measurements in axon membranes. In *Membranes, Ions, and Impulses*, pages 29–45. Springer, 1975.

[105] D. L. Dorset and H. M. Fishman. Excess electrical noise during current flow through porous membranes separating ionic solutions. *Journal of Membrane Biology* 21(1):291–309, 1975.

[106] R. Sauvé and E. Bamberg. 1/f noise in black lipid membranes induced by ionic channels formed by chemically dimerized gramicidin a. *Journal of Membrane Biology* 43(4):317–333, 1978.

[107] S. Nekolla, C. Andersen, and R. Benz. Noise analysis of ion current through the open and the sugar-induced closed state of the lamb channel of escherichia coli outer membrane: evaluation of the sugar binding kinetics to the channel interior. *Biophysical Journal* 66(5):1388–1397, 1994.

[108] O. P. Hamill, A. Marty, E. Neher, B. Sakmann, and F. Sigworth. Improved patch-clamp techniques for high-resolution current recording from cells and cell-free membrane patches. *Pflügers Archiv European journal of physiology* 391(2):85–100, 1981.

[109] S. M. Bezrukov and J. J. Kasianowicz. Current noise reveals protonation kinetics and number of ionizable sites in an open protein ion channel. *Physical Review Letters* 70(15):2352, 1993.

[110] S. M. Bezrukov and I. Vodyanoy. Noise-induced enhancement of signal transduction across voltage-dependent ion channels. *Nature* 378(6555):362, 1995.

[111] J. A. White, J. T. Rubinstein, and A. R. Kay. Channel noise in neurons. *Trends in Neurosciences* 23(3):131–137, 2000.

[112] A. A. Faisal, L. P. Selen, and D. M. Wolpert. Noise in the nervous system. *Nature Reviews Neuroscience* 9(4):292–303, 2008.

[113] S. M. Bezrukov and M. Winterhalter. Examining noise sources at the single-molecule level: 1/f noise of an open maltoporin channel. *Physical Review Letters* 85(1):202, 2000.

[114] Z. Siwy and A. Fuliński. Origin of $1/f^{\alpha}$ noise in membrane channel currents. *Physical Review Letters* 89(15):158101, 2002.

[115] I. Goychuk and P. Hänggi. Stochastic resonance in ion channels characterized by information theory. *Physical Review E* 61(4):4272, 2000.

[116] I. Goychuk and P. Hänggi. Ion channel gating: a first-passage time analysis of the kramers type. *Proceedings of the National Academy of Sciences* 99(6):3552–3556, 2002.

[117] I. Goychuk and P. Hänggi. Fractional diffusion modeling of ion channel gating. *Physical Review E* 70(5):051915, 2004.

[118] I. Goychuk and P. Hänggi. Anomalous escape governed by thermal 1/f noise. *Physical Review Letters* 99(20):200601, 2007.

[119] J. Banerjee, M. K. Verma, S. Manna, and S. Ghosh. Self-organised criticality and 1/f noise in single-channel current of voltage-dependent anion channel. *EPL (Europhysics Letters)* 73(3): 457, 2006.

[120] C. Dekker. Solid-state nanopores. *Nature Nanotechnology* 2(4):209–215, 2007.

[121] J. Li, D. Stein, C. McMullan, D. Branton, M. J. Aziz, and J. A. Golovchenko. Ion-beam sculpting at nanometre length scales. *Nature* 412(6843):166–169, 2001.

[122] P. Chen, T. Mitsui, D. B. Farmer, J. Golovchenko, R. G. Gordon, and D. Branton. Atomic layer deposition to fine-tune the surface properties and diameters of fabricated nanopores. *Nano Letters* 4(7):1333–1337, 2004.

[123] R. M. Smeets, U. F. Keyser, D. Krapf, M.-Y. Wu, N. H. Dekker, and C. Dekker. Salt dependence of ion transport and DNA translocation through solid-state nanopores. *Nano letters* 6(1):89–95, 2006.

[124] U. F. Keyser, B. N. Koeleman, S. Van Dorp, D. Krapf, R. M. Smeets, S. G. Lemay, N. H. Dekker, and C. Dekker. Direct force measurements on DNA in a solid-state nanopore. *Nature*

Physics 2(7):473–477, 2006.

[125] D. Fologea, M. Gershow, B. Ledden, D. S. McNabb, J. A. Golovchenko, and J. Li. Detecting single stranded DNA with a solid state nanopore. *Nano Letters* 5(10):1905–1909, 2005.

[126] J. Kong, N. A. Bell, and U. F. Keyser. Quantifying nanomolar protein concentrations using designed DNA carriers and solid-state nanopores. *Nano letters* 16(6):3557–3562, 2016.

[127] S. Van Dorp, U. F. Keyser, N. H. Dekker, C. Dekker, and S. G. Lemay. Origin of the electrophoretic force on DNA in solid-state nanopores. *Nature Physics* 5(5):347–351, 2009.

[128] R. Smeets, U. Keyser, M. Wu, N. Dekker, and C. Dekker. Nanobubbles in solid-state nanopores. *Physical review letters* 97(8):088101, 2006.

[129] R. Smeets, U. Keyser, M. Wu, N. Dekker, and C. Dekker. Nanobubbles in solid-state nanopores. *Physical Review Letters* 97(8):088101, 2006.

[130] K. Venta, G. Shemer, M. Puster, J. A. Rodriguez-Manzo, A. Balan, J. K. Rosenstein, K. Shepard, and M. Drndic. Differentiation of short, single-stranded DNA homopolymers in solid-state nanopores. *ACS Nano* 7(5):4629–4636, 2013.

[131] J. Shi, J. Hou, and Y. Fang. Recent advances in nanopore-based nucleic acid analysis and sequencing. *Microchimica Acta* 183(3):925–939, 2016.

[132] J.-H. Jeon and R. Metzler. Fractional brownian motion and motion governed by the fractional langevin equation in confined geometries. *Physical Review E* 81(2):021103, 2010.

[133] C. Tasserit, A. Koutsioubas, D. Lairez, G. Zalczer, and M.-C. Clochard. Pink noise of ionic conductance through single artificial nanopores revisited. *Physical Review Letters* 105(26): 260602, 2010.

[134] I. Kosińska and A. Fuliński. Brownian dynamics simulations of flicker noise in nanochannels currents. *EPL (Europhysics Letters)* 81(5):50006, 2008.

[135] V. Marx. Nanopores: a sequencer in your backpack. *Nature Methods* 12(11):1015, 2015.

[136] G. Liu, S. Rumyantsev, M. S. Shur, and A. A. Balandin. Origin of 1/f noise in graphene multilayers: Surface vs. volume. *Applied Physics Letters* 102(9):093111, 2013.

[137] N. V. Prabhu, M. Panda, Q. Yang, and K. A. Sharp. Explicit ion, implicit water solvation for molecular dynamics of nucleic acids and highly charged molecules. *Journal of Computational Chemistry* 29(7):1113–1130, 2008.

[138] J. Kleinjung and F. Fraternali. Design and application of implicit solvent models in biomolecular simulations. *Current Opinion in Structural Biology* 25:126–134, 2014.

[139] R. C. Weast, M. J. Astle, and W. H. Beyer. *CRC handbook of chemistry and physics*, volume 69. CRC press Boca Raton, FL, 1988.

[140] N. W. Ashcroft and N. D. Mermin. *Solid State Physics (Holt, Rinehart and Winston, New York, 1976)*, volume 403. Oldenbourg, 2005.

[141] F. Seitz and D. Turnbull. *Solid State Physics*, volume 7. Academic Press, 1958.

[142] C. Kittel. *Introduction to Solid State Physics*. Wiley, 2005.

[143] H.-J. Limbach, A. Arnold, B. A. Mann, and C. Holm. Espresso—an extensible simulation package for research on soft matter systems. *Computer Physics Communications* 174(9):704–727, 2006.

[144] P. Gibbon and G. Sutmann. Long-range interactions in many-particle simulation. *Quantum simulations of many-body systems: from theory to algorithm. Eds. J. Grotendorst, D. Marx and A. Muramatsu. NIC-series* 10:467–506, 2002.

[145] H. Lee and W. Cai. Ewald summation for Coulomb interactions in a periodic supercell. *Lecture Notes, Stanford University* 3(1):1–12, 2009.

[146] R. W. Hockney and J. W. Eastwood. *Computer simulation using particles*. CRC Press, 1988.

[147] J. Eastwood and R. Hockney. Computer simulation using particles. *New York: Mc GrawHill* 1981.

[148] M. Deserno and C. Holm. How to mesh up ewald sums. i. a theoretical and numerical comparison of various particle mesh routines. *The Journal of Chemical Physics* 109(18):7678–7693, 1998.

[149] J. J. Cerda, V. Ballenegger, O. Lenz, and C. Holm. P^3M algorithm for dipolar interactions. *The Journal of chemical physics* 129(23):234104, 2008.

[150] C. Holm. Efficient methods for long range interactions in periodic geometries plus one application. *Computational Soft Matter: From Synthetic Polymers to Proteins* 23:195–236, 2004.

[151] J. J. Cerdà, V. Ballenegger, and C. Holm. Particle-particle particle-mesh method for dipolar interactions: On error estimates and efficiency of schemes with analytical differentiation and

mesh interlacing. *The Journal of chemical physics* 135(18):184110, 2011.

[152] R. Elber. *Recent developments in theoretical studies of proteins*, volume 7. World Scientific, 1996.

[153] A. Y. Kuksin, I. Morozov, G. Norman, V. Stegailov, and I. Valuev. Standards for molecular dynamics modelling and simulation of relaxation. *Molecular Simulation* 31(14-15):1005–1017, 2005.

[154] J. Glosli, F. Graziani, R. More, M. Murillo, F. Streitz, M. Surh, L. Benedict, S. Hau-Riege, A. Langdon, and R. London. Molecular dynamics simulations of temperature equilibration in dense hydrogen. *Physical Review E* 78(2):025401, 2008.

[155] L. X. Benedict, M. P. Surh, L. G. Stanton, C. R. Scullard, A. A. Correa, J. I. Castor, F. R. Graziani, L. A. Collins, O. Čertík, J. D. Kress, et al. Molecular dynamics studies of electron-ion temperature equilibration in hydrogen plasmas within the coupled-mode regime. *Physical Review E* 95(4):043202, 2017.

[156] P. H. Hünenberger. Thermostat algorithms for molecular dynamics simulations. *Advanced computer simulation* pages 130–130, 2005.

[157] R. L. Davidchack, R. Handel, and M. Tretyakov. Langevin thermostat for rigid body dynamics. *The Journal of Chemical Physics* 130(23):234101, 2009.

[158] N. Grønbech-Jensen and O. Farago. Constant pressure and temperature discrete-time langevin molecular dynamics. *The Journal of chemical physics* 141(19):194108, 2014.

[159] G. Bussi, D. Donadio, and M. Parrinello. Canonical sampling through velocity rescaling. *The Journal of chemical physics* 126(1):014101, 2007.

[160] M. Ferrario, G. Ciccotti, and K. Binder. *Computer simulations in condensed matter: from materials to chemical biology*, volume 1. Springer, 2007.

[161] C. Junghans. *Between the scales: water from different perspectives*. PhD thesis, Max-Planck-Institut für Polymerforschung, 2010.

[162] G. S. Grest and K. Kremer. Molecular dynamics simulation for polymers in the presence of a heat bath. *Physical Review A* 33(5):3628, 1986.

[163] R. D. Groot and P. B. Warren. Dissipative particle dynamics: Bridging the gap between atomistic and mesoscopic simulation. *The Journal of Chemical Physics* 107(11):4423–4435, 1997.

[164] P. B. Warren. Dissipative particle dynamics. *Current Opinion in Colloid & Interface Science* 3 (6):620–624, 1998.

[165] U. D. Schiller. *Dissipative particle dynamics. A study of the methodological background*. PhD thesis, University of Bielefeld, Germany, 2005.

[166] D. Villamaina and E. Trizac. Thinking outside the box: fluctuations and finite size effects. *European Journal of Physics* 35(3):035011, 2014.

[167] P. Welch. The use of fast fourier transform for the estimation of power spectra: a method based on time averaging over short, modified periodograms. *IEEE Transactions on Audio and Electroacoustics* 15(2):70–73, 1967.

[168] J. Feng, K. Liu, M. Graf, D. Dumcenco, A. Kis, M. Di Ventra, and A. Radenovic. Observation of ionic Coulomb blockade in nanopores. *Nature Materials* 15(8):850–855, 2016.

[169] M. Krems and M. Di Ventra. Ionic Coulomb blockade in nanopores. *Journal of Physics: Condensed Matter* 25(6):065101, 2013.

[170] B. Luan and A. Aksimentiev. Electro-osmotic screening of the DNA charge in a nanopore. *Physical Review E* 78(2):021912, 2008.

[171] K. Leung and S. B. Rempe. Ion rejection by nanoporous membranes in pressure-driven molecular dynamics simulations. *Journal of Computational and Theoretical Nanoscience* 6(8):1948–1955, 2009.

[172] D. P. Hoogerheide, S. Garaj, and J. A. Golovchenko. Probing surface charge fluctuations with solid-state nanopores. *Physical Review Letters* 102(25):256804, 2009.

[173] F. Wohnsland and R. Benz. 1/f-noise of open bacterial porin channels. *Journal of Membrane Biology* 158(1):77–85, 1997.

[174] M. R. Powell, I. Vlassiouk, C. Martens, and Z. S. Siwy. Nonequilibrium 1/f noise in rectifying nanopores. *Physical Review Letters* 103(24):248104, 2009.

[175] R. Phillips, T. Ursell, P. Wiggins, and P. Sens. Emerging roles for lipids in shaping membrane-protein function. *Nature* 459(7245):379–385, 2009.

[176] L. Picas, F. Rico, and S. Scheuring. Direct measurement of the mechanical properties of lipid

phases in supported bilayers. *Biophysical Journal* 102(1):L01–L03, 2012.

[177] J. Kotar, M. Leoni, B. Bassetti, M. C. Lagomarsino, and P. Cicuta. Hydrodynamic synchronization of colloidal oscillators. *Proceedings of the National Academy of Sciences* 107(17):7669–7673, 2010.

[178] W. Lee, H. Amini, H. A. Stone, and D. Di Carlo. Dynamic self-assembly and control of microfluidic particle crystals. *Proceedings of the National Academy of Sciences* 107(52):22413–22418, 2010.

[179] R. Golestanian, J. M. Yeomans, and N. Uchida. Hydrodynamic synchronization at low Reynolds number. *Soft Matter* 7(7):3074–3082, 2011.

[180] J. L. McWhirter, H. Noguchi, and G. Gompper. Flow-induced clustering and alignment of vesicles and red blood cells in microcapillaries. *Proceedings of the National Academy of Sciences* 106(15):6039–6043, 2009.

[181] M. Hagen, I. Pagonabarraga, C. Lowe, and D. Frenkel. Algebraic decay of velocity fluctuations in a confined fluid. *Physical Review Letters* 78(19):3785, 1997.

[182] K. Misiunas, S. Pagliara, E. Lauga, J. R. Lister, and U. F. Keyser. Nondecaying hydrodynamic interactions along narrow channels. *Physical Review Letters* 115(3):038301, 2015.

[183] M. Fyta, S. Melchionna, S. Succi, and E. Kaxiras. Hydrodynamic correlations in the translocation of a biopolymer through a nanopore: Theory and multiscale simulations. *Physical Review E* 78 (3):036704, 2008.

[184] N. Laohakunakorn, S. Ghosal, O. Otto, K. Misiunas, and U. F. Keyser. DNA interactions in crowded nanopores. *Nano Letters* 13(6):2798–2802, 2013.

[185] S. J. Marrink, H. J. Risselada, S. Yefimov, D. P. Tieleman, and A. H. De Vries. The MARTINI force field: coarse grained model for biomolecular simulations. *The journal of physical chemistry B* 111(27):7812–7824, 2007.

[186] S. O. Yesylevskyy, L. V. Schäfer, D. Sengupta, and S. J. Marrink. Polarizable water model for the coarse-grained MARTINI force field. *PLoS computational biology* 6(6):e1000810, 2010.

[187] K. R. Hadley and C. McCabe. Coarse-grained molecular models of water: a review. *Molecular Simulation* 38(8-9):671–681, 2012.

[188] J. Padding and A. Louis. Hydrodynamic interactions and brownian forces in colloidal suspensions: Coarse-graining over time and length scales. *Physical Review E* 74(3):031402, 2006.

[189] A. Gelimson and R. Golestanian. Collective dynamics of dividing chemotactic cells. *Physical Review Letters* 114(2):028101, 2015.

2